

**A Corticostriatal Mechanism for Integrating Subjective Value into Processes  
of Risky Decision-Making**

Kevin Jarbo

August 2018

A Dissertation Presented in Partial Fulfillment  
of Requirements for the Degree of  
Doctor of Philosophy

Graduate Supervisory Committee

Dr. Timothy Verstynen, Chair

Dr. Bobby Klatzky

Dr. Marlene Behrmann

Department of Psychology &  
Center for the Neural Basis of Cognition  
Carnegie Mellon University

*For my parents, Thelma and George*

*You gifted me the dream of becoming a doctor. I hope that seeing my dream become our reality is only the beginning of how I will pay you back for all you have ever given me and sacrificed to ensure my personal growth and success.*

*For my siblings, Nicole and Ted*

*You have always held me accountable to the charge of being the best example of an older brother that I could possibly be. I will always strive for excellence because of the two of you.*

*For Caroline, my partner for life*

*You believed something good about me that I refused to acknowledge, especially when I was losing myself during the darkest points in the process of composing this dissertation. I never had to doubt the constancy of your unconditional love, support, and encouragement.*

*You are my mirror and my light.*

*For Tim*

*You saw something in me that I never believed I had. You have always been in my corner, pushing me to the limits of my potential, working side-by-side with me when I needed you, and letting me explore all of my intellectual and personal passions on my own when I needed to. Without question, graduate training with you has been the most fulfilling experience of my life.*

*I will never be able to thank you all enough for always believing in me.*

# Acknowledgements

My deepest thanks go to my chair, Tim. “You’d be a great grad student one day.” I will never forget when you said those words to me. We have come a long way since sharing an office, and I look forward to how far we can both go, individually and together.

I also thank my committee, Dr. Bobby Klatzky and Dr. Marlene Behrmann. Some of my toughest critics and staunchest supporters. You both have given me invaluable tools and indispensable wisdom that I will take with me wherever my intellectual pursuits lead. I cannot say how much I appreciate the way you have held me to the highest standards. Because of that, I will never back down from a challenge to exceed anyone’s expectations.

CoAx Lab is family. Much of the work in this dissertation was made possible by two extremely dedicated undergraduate researchers, Rory Flemming and Cristina Bañuelos, who collected so much of the data and came to the lab with such a strong willingness to learn that it inspired me to work harder. I only hope that any of the mentorship and tutelage I have provided you proves useful in your own personal and professional endeavors. Thanks to some of the earliest CoAx Lab members, Tara Molesworth and Brighid Lynch, who helped launch the Danger Zone study that became a cornerstone of all this work. My more recent CoAx compatriots, Alexis Porter and Krista Bond, thank you continually being sources of social support and for taking the time to disengage from work for deeper conversations about our experiences in academia. I hope those moments of reflection for me will serve you well as you move to the next levels of your own academic careers. Kyle Dunovan and Patrick Beukema, you two jokers have been the most

crucial part of my graduate student experience since Day 1. You both have seen the best and worst of me, and you have always been there to support me in more ways than I knew I needed. You will always be able to count on me to reciprocate that love.

David Colaço, thank you for letting me know that you appreciated the way I did science. I am not sure I ever would have believed it was any good on my own. You gifted me with a new perspective on how to think and how to seek out the answers to some of my biggest, personal, philosophical questions. Thanks for convincing me to apply to SSNAP, because I never would have pursued that avenue on my own. My progression as a scholarly critic of my own work is due in large part to conversing and collaborating with you over the last two years, and I look forward to reaping the fruits of our fortuitous pairing.

Psych Grads, you all have been my collective rock over the last five years, and it is pretty astonishing to me that I have known some folks even longer. I could not put together a better group of people to support me and create the kind of communal environment that has been built here in the CMU Psychology Department. I feel like something special was forged and that everyone played a role in pushing the entire department forward. If anything, never forget your individual and collective capacity to inspire and uplift others. Those are among the greatest gifts you all have given me, and I offer you my sincerest gratitude for how you have rallied around me, and each other, to see everyone to the finish line of this graduate student experience.

Thank you to the entire Psychology Department staff, postdocs, faculty, and administrators. As soon as I set foot in the department, I felt like I was bathing in brilliance. At the same time, I felt like I have always belonged here. So many of you have helped cultivate an atmosphere of learning and compassion. There was never a time when I thought no one was looking out for me. I could always air my grievances, get lost in deep conversations, or just work together on a jigsaw puzzle. CMU Psych will forever feel like home to me.

Big big thanks to the Center for Student Diversity & Inclusion, the Black Graduate Student Organization, and Call to Action! In the last two years, I found myself really struggling to find my place and my purpose at this university. The Center and BGSO opened their doors and their arms to me, almost like you were waiting for me to come knock. I knew what it meant to feel welcome, I learned from you what it meant to be empowered, and I started to become my whole self at CMU because of you. Certain individuals have my deepest gratitude here: Ms. M. Shernell Smith, “The Heart of Carnegie Mellon University”; Dr. Travis Carless, my sands and fellow President’s Fellow; soon-to-be Dr. Chelsea Jones, who told me I “might as well be BGSO’s Activism Chair” and woke a brother all the way up! Without the three of you here at CMU, I would never have known my place. Having had you, I will never be lost.

My family, I thank you all for taking the time to attend my defense and share the greatest moment in my life together. We all worked for this achievement and I could not have done this without your inspiration.

I thank Thomas Powell, my dear friend and Good Brother. I never would have thought we would both be in Pittsburgh together after becoming friends the first week of undergrad at Pitt. Sitting here sixteen years later, I am honored and lucky to have had you as a friend for all these years. We have shared a lot of our finest moments together, and I know we will have a lot more on the way! Yo, yo!!!

Lastly, I thank my graduate training support and funding sources, including: the Center for the Neural Basis of Cognition, NIH B<sup>2</sup> Training Grant, Multimodal Neuroimaging Training Program Fellowship, Kavli Institute Summer Institute in Cognitive Neuroscience (i.e., “Brain Camp”), and the Summer Seminars in Neuroscience and Philosophy (SSNAP) and the John Templeton Foundation.

K. Jarbo

# Table of Contents

|   |    |
|---|----|
| Dedication  | 1  |
| Acknowledgements  | 2  |
| Table of Contents   | 6  |
| Abstract  | 11 |
| Glossary of Terms   | 12 |
| Chapter 1: Introduction   | 14 |
| 1.1    Psychological components of risky spatial decisions  | 15 |
| 1.2    Algorithms of spatial decisions  | 20 |
| 1.2.1    Statistically rational sensorimotor integration  | 20 |
| 1.2.2    Spatial decisions in risky contexts  | 22 |
| 1.3    Subjective estimates of multiple kinds of variability affect spatial decisions             | 25 |
| 1.3.1    Sensory input estimates  | 26 |
| 1.3.2    Motor output estimates   | 27 |
| 1.3.3    Probability distortions  | 29 |
| 1.3.4    Explicit cognitive strategies impact implicit sensorimotor decisions                     | 31 |
| 1.4    Neural mechanisms of spatial decisions   | 32 |
| 1.4.1    Multiple brain regions represent different components of spatial decisions               | 33 |
| 1.4.2    Brain areas involved in spatial decisions are highly interconnected locally and globally | 39 |

|  |   |    |
|--|---|----|
| 1.4.3  | Structural and functional connectivity converge in the striatum | 41 |
| 1.5  | Open questions and specific aims                                | 43 |
| 1.5.1  | Specific aims   | 44 |
| Chapter 2: Sensory uncertainty impacts avoidance during spatial decisions                |   | 48 |
| 2.1  | Introduction  | 49 |
| 2.2  | Methods   | 54 |
| 2.2.1  | Participants  | 54 |
| 2.2.2  | Experimental setup  | 55 |
| 2.2.3  | Experimental task   | 55 |
| 2.2.4  | Data analysis   | 60 |
| 2.3  | Results   | 61 |
| 2.4  | Discussion  | 64 |
| 2.5  | Conclusion  | 68 |
| Chapter 3: Contextual framing of a risky spatial decision outcome impacts loss avoidance |   | 69 |
| 3.1  | Introduction  | 69 |
| 3.1.1  | Contextual framing effects on risky decision                    | 71 |
| 3.1.2  | Framing impacts moral judgments of decision outcomes            | 71 |
| 3.1.3  | Contextual framing and the maximum expected gain model          | 72 |
| 3.2  | Methods   | 74 |
| 3.2.1  | Participants  | 74 |
| 3.2.2  | Experimental setup and design                                   | 75 |
| 3.2.3  | Data analysis   | 79 |

|  |   |     |
|--|---|-----|
| 3.3  | Results   | 82  |
| 3.3.1  | Selection bias  | 84  |
| 3.3.2  | Harm versus help differences                            | 87  |
| 3.3.3  | Selection variability                                   | 90  |
| 3.3.4  | Reaction and movement time                              | 90  |
| 3.3.5  | Maximum and average movement velocity                   | 91  |
| 3.4  | Discussion  | 92  |
| 3.5  | Conclusion  | 99  |
| Chapter 4: Converging structural and functional connectivity of orbitofrontal,<br>dorsolateral prefrontal, and posterior parietal cortex in the human striatum |   | 100 |
| 4.1  | Introduction  | 101 |
| 4.2  | Methods   | 103 |
| 4.2.1  | Participants  | 103 |
| 4.2.2  | MRI acquisition   | 103 |
| 4.2.3  | Fiber tractography and analysis                         | 105 |
| 4.2.4  | Striatal and cortical endpoint distribution analysis    | 107 |
| 4.2.5  | Resting state fMRI preprocessing and analysis           | 109 |
| 4.2.6  | Structural and functional connectivity overlap analysis | 111 |
| 4.3  | Results   | 112 |
| 4.3.1  | Topography of corticostriatal projections               | 112 |
| 4.3.2  | Convergence of corticostriatal projections              | 116 |
| 4.3.3  | Functional connectivity of convergence zones            | 123 |

|   |  |     |
|---|--|-----|
| 4.3.4   | Structure-function overlap                                       | 127 |
| 4.4   | Discussion   | 134 |
| 4.5   | Conclusion   | 139 |
| Chapter 5: Left putamen encodes task context during risky spatial decisions |  | 140 |
| 5.1   | Introduction   | 140 |
| 5.2   | Methods  | 143 |
| 5.2.1   | Participants   | 143 |
| 5.2.2   | Behavioral experimental design                                   | 144 |
| 5.2.3   | Behavioral data analysis   | 150 |
| 5.2.4   | MRI acquisition  | 151 |
| 5.2.5   | MRI preprocessing  | 152 |
| 5.2.6   | Modeling BOLD responses in general linear (GLM) analysis         | 154 |
| 5.2.7   | Defining regions-of-interest (ROIs)                              | 155 |
| 5.2.8   | Transforming ROIs from MNI to native space                       | 156 |
| 5.2.9   | ROI-based GLM contrast analysis                                  | 158 |
| 5.2.10  | Modeling BOLD responses for representational similarity analysis | 159 |
| 5.2.11  | Representational similarity analysis                             | 159 |
| 5.3   | Behavioral results   | 161 |
| 5.3.1   | Selection bias and variability                                   | 165 |
| 5.3.2   | Reaction and movement time                                       | 166 |
| 5.3.3   | Maximum and average velocity                                     | 167 |
| 5.4   | fMRI results   | 168 |

|  |  |     |
|--|--|-----|
| 5.4.1  | Whole-brain GLM results  | 168 |
| 5.4.2  | ROI-based GLM contrast results                                 | 170 |
| 5.4.3  | RSA results  | 172 |
| 5.5  | Discussion   | 177 |
| 5.6  | Conclusion   | 183 |
| Chapter 6: Conclusions and future directions |  | 184 |
| 6.1  | Contributions of individual studies                            | 185 |
| 6.1.1  | Extended predictions of the maximum expected gain model        | 185 |
| 6.1.2  | Elucidated contextual effects on risky spatial decision-making | 186 |
| 6.1.3  | Linked moral choice to risky spatial decision-making           | 187 |
| 6.1.4  | Identification of action-value connectivity in the human brain | 189 |
| 6.2  | Limitations of the current work                                | 192 |
| 6.3  | Toward a causal mechanism of risky spatial decision-making     | 194 |
| 6.4  | Concluding remarks   | 199 |
| References (in alphabetical order)           |  | 201 |

# Abstract

Making risky spatial decisions requires the efficient integration of spatial signals, value, and context (Trommershäuser et al., 2003; Neyedli & LeBlanc, 2017). Functional magnetic resonance imaging has provided evidence for an ideal network of posterior parietal regions that process spatial signals for motor control (Lindner et al., 2010), orbitofrontal areas that encode value estimates (Hsu et al, 2005), and dorsolateral prefrontal areas that represent contextual constraints on behavior (Badre & Frank, 2012). Nonhuman primate research has shown convergent white matter projections from those cortical regions into the anterior striatum (Haber & Knutson, 2010; Selemon & Goldman-Rakic, 1988), indicating an ideal point for integrating information from multiple cortical processes. Recently, the anterior striatum has been proposed as an “action-value” zone that is involved in evaluating action decisions (Pauli et al., 2016), which suggests it is critical in optimizing sensorimotor behavior on risky spatial decision tasks. However, the integrative structure of this corticostriatal action-value network in humans and its role in risky spatial decision-making is not fully determined. In addressing these open questions, I present 1) a series of experiments designed to establish the effects of spatial signals, value, and context during risky spatial decision-making, 2) confirmation of a convergent corticostriatal network of DLPFC, OFC, and PPC inputs in the human brain, and 3) a final project that examines action-value representations in the striatum. These projects combine multimodal neuroimaging studies and novel behavioral experiments to delineate a neural mechanism of cognitive penetration, wherein the contextual framing of a risky outcome impacts perceptual estimation and action selection processes involved in value-based spatial sensorimotor decisions.

# Glossary of Terms

**Value** A scalar amount assigned to one choice option that represents either the expected numerical gain (positive) or loss (negative) associated with a decision

**Subjective value** An idiosyncratic measure of utility that indicates an individual's preference for one choice option with greater utility than any other option with lower utility

**Context** A narrative instruction or cue that provides explicit information about the objective of a behavioral task and/or the stimuli involved in task performance

**Risk** The known or estimable probability of an expected loss associated with a decision outcome

**Risk seeking** Preference for a relatively large potential loss rather than sure loss with the same expected value

**Risk averse** Preference for a sure loss rather a relatively large potential loss with the same expected value

**Risky spatial decision** The mental process of choosing a targeted location within a visually-presented stimulus that is comprised of adjacent and/or overlapping reward (gain) and penalty (loss) regions. The term “selection” is used throughout the document to refer to the endpoint of the movement toward the targeted location. Risk is the probability of expected loss incurred on a selection that is within, or proximal to, the penalizing region of the stimulus.

**Spatial priority** The location within a visually-presented stimulus that is targeted for selection based on its position within a reward region of the stimulus and its association with either maximum expected gain or the greatest relative subjective value compared to other locations.

# Chapter 1

## Introduction

Despite complex spatial constraints and multiple sources of noise, humans are able to smoothly execute visually guided movements with relatively little apparent effort. A large body of empirical research is framed by prominent theories of sensorimotor control that assume implicit computations on spatial stimuli incorporate the structure of both sensory and motor variability in statistically rational processes that maximize the accuracy and precision of spatial sensorimotor decisions. However, more recent findings suggest that human sensorimotor behavior may be at least partially inconsistent with these statistically rational models. For example, in order to meet the explicit contextual demands of perceptually-based spatial judgments, people exhibit behavior that more closely reflects action selection strategies that either attempt to minimize the risk of potential loss or flexibly alter constraints on performance--but neither strategy is necessarily a statistically optimal approach to maximizing expected gain on a risky spatial decision based purely on external feedback signals. This suggests that a subjective value signal driven by contextual factors can also influence action selection in a way that deviates from the predictions of statistically rational sensorimotor integration models. Psychologically, action selection during spatial decision-making appears to be minimally comprised of component processes that must represent estimates of sensory variability, executive action selection signals, and the subjective value of spatial targets. Neurally, these component processes are reflected in the activity of several distributed cortical areas that are both structurally interconnected within and between

each region and have convergent projections within the striatum. Here, I open this dissertation with a review of literature on statistically rational models of implicit sensorimotor integration processes and evidence suggesting that explicit contextual demands also influence subjective estimates of value during cognitive processes that underlie biases in sensorimotor behavior. I also describe a network of corticocortical and corticostriatal circuitry that can support the necessary representations and computations for the component processes of spatial sensorimotor decisions.

### 1.1 Psychological components of risky spatial decisions

Imagine an operator operating a weaponized drone in an active warzone. The drone is capable of fast, high precision missile strikes on targeted locations. It relays the positions of enemies and allies to a screen at a command station to control each strike. With visual information about the real time spatial positions of enemies and allies, the operator must rapidly estimate and then select targeted strike locations. Now consider a situation where enemies and allies are positioned in close proximity, creating the risk of ally casualties. Toward the overall objective of winning the war, the operator should target locations that maximize enemy casualties, while avoiding ally losses. How does the operator quickly select a single location from the spatial distributions of enemies and allies to execute a strike?

The example above describes a risky spatial decision that combines sensory input and motor output component processes, that humans appear to perform this sort of spatial decision making effortlessly. First, the spatial distribution of operator positions is estimated from visual input. If enemy positions are distributed about a single location (e.g., the centroid of a 2D

Gaussian distribution), then the mean and variance, or sensory uncertainty, of the distribution can be estimated statistically. In this case, the mean represents the optimal spatial location to aim for and select that guarantees the greatest number of enemy casualties on a strike. However, an element of risk also exists such that selecting too close to a location with a high cost (i.e., near allies) increases the probability of a loss (i.e., ally casualties). This risk, or probability associated with a possible decision outcome, must also be considered in the spatial decision process. Then, to execute the selection, an internal motor plan must first represent the targeted location based on estimates of both visual input and risk, and then be gated to perform the corresponding movement output. Given that noise in sensory input is propagated to motor output (Faisal, Selen, & Wolpert, 2008; Osborne, Lisberger, & Bialek, 2005), both external (i.e., spatial variance and risk) and internal (i.e., motor execution) sources of variability must be accounted for during spatial decision processes that determine action selections.

Based on statistical decision theory (Berger, 1985; Maloney & Zhang, 2010), the maximum expected gain model of sensorimotor control provides a framework for incorporating sensory and motor noise during risky spatial decisions (Trommershäuser, Maloney, & Landy, 2003a, 2008). Risk is accounted for by weighting the estimates of each distribution in a spatial stimulus. For instance, when enemies are positioned near a distribution of objects that will not incur a loss, say trees, only enemy locations will contribute to the selection decision, while trees may be ignored. However, when allies are nearby instead, then the spatial distribution of ally locations must also be weighed relative to the distribution of enemy positions. Here, the maximum expected gain model predicts a shift, or bias, of selections away from ally positions to mitigate potential losses while ensuring some enemy casualties. It follows that if allies are

positioned close to the center of enemy positions, then a selection will be biased away from the optimal strike location, i.e., the center or mean of the enemy distribution, that maximizes enemy casualties. Thus, rather than selecting the optimal spatial location, individuals adopt a more risk seeking action selection strategy that is less certain to maximize expected gain.

Framing a risky decision in terms of a high loss probability (i.e., possible ally casualties) rather than gain (i.e., only enemy casualties), can lead people to prefer a risky prospect to a more certain outcome with equal or greater expected value (Tversky & Fox, 1995). Though framing effects have been shown to apply more directly to learning and memory (Pichert & Anderson, 1977), reasoning (Griggs & Cox, 1982; Wason & Shapiro, 1971), and economic choice (Kahneman & Tversky, 1979) that are cognitive in nature, contextual framing seems to also influence perceptual sensorimotor processes in spatial decision behavior.

In economic choice, cognitive framing effects on risk evaluation that increase loss aversion described in prospect theory (Kahneman & Tversky, 1979) parallel context effects on action selection behavior during spatial decisions. Assume that the distributions of ally operator positions or trees near enemies on separate strikes have the same mean and variance. The spatial estimation process for localizing the enemy distribution mean is the same in both cases, as is the motor process of selecting the distribution mean in order to maximize enemy casualties. Instead of ignoring the tree distribution on a given drone strike selection, the statistically and spatially equivalent distribution of allies must be considered as a potential loss to avoid. Critically, the only difference between the ally and tree distributions in the decision process that drives avoidance is the contextual framing of risk as a potential loss of allies in the spatial estimates that must be made.

Loss averse behavior arising from the contextual framing of a spatial decision suggests that the cognitive process of risk evaluation can penetrate implicit processes that integrate estimates of sensory input and motor output variability. Psychologically, the maximum expected gain model gives a computational account for how risk is incorporated into sensorimotor processes that result in observable avoidance bias. This raises the question of how this cognitive penetration can occur mechanistically to link sensory input to motor output. Namely, what is the neural circuitry that integrates estimates of both sensory variance and motor variability with risks to influence spatial decision-making behavior? Additionally, how might the activity of a putative network of brain regions involved in risky spatial decisions represent distinct contexts that frame gains and losses that lead to biased action selection behavior?

Here, I discuss theoretical and empirical research that attempt to explain how humans incorporate estimates of perceptual uncertainty into risky spatial decisions. I will highlight a model of the component processes that are necessary to make these decisions. Then, I will identify a neurologically plausible substrate for these component processes to argue for integrative psychological and neural mechanisms that allow for the penetration of contextual information about risks into implicit sensorimotor estimation processes that bias behavior during spatial decision-making.

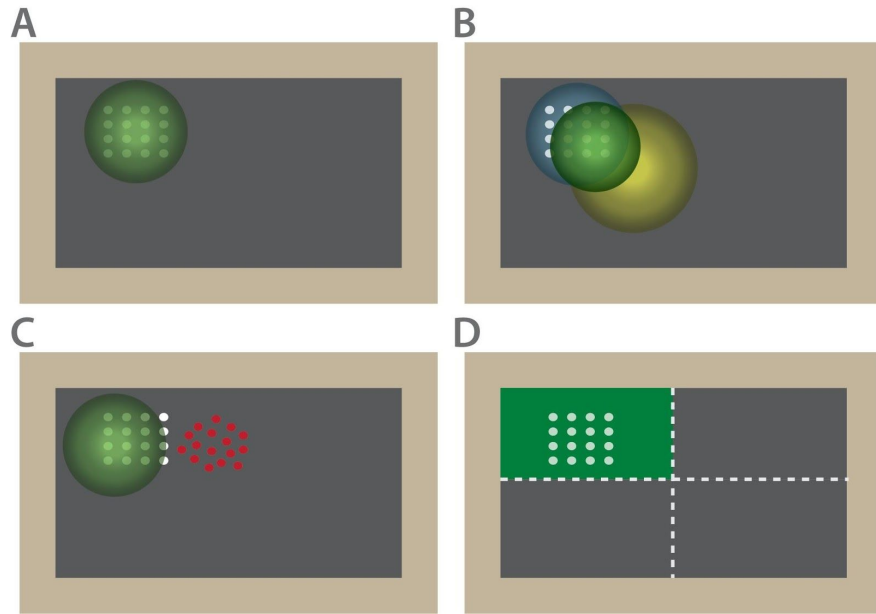


**Figure 1.1** Drone strike example comparing models of sensorimotor decisions about where to target missiles. This example is similar to a ballistic reach in that minimizing the error between the landing and the reach endpoint (e.g., missile strike point) is the goal of the spatial decision, not optimizing the movement trajectory (e.g., missile flight). Each panel shows an airfield surrounded by desert (dark gray rectangle in light brown rectangle) with the position of jets represented by white dots as viewed by an operator operating a drone. A) Optimal control theory posits that when the spatial distribution of a sensory target is known (e.g., jet locations), motor (aiming) variance should be constrained in the costliest dimensions of movement to maximize outcome. Since motor variance is Gaussian (graded green circle), the best location to aim for is the center of the cluster of jets. B) A normative Bayesian approach combines a prior history of missile strike success (graded yellow circle) with the likelihood of strike success (graded blue circle) to generate a posterior distribution (graded green circle) centered over the best aiming location on the airfield. C) Based on the statistical decision theory framework, an expected gain function can be estimated by associating relatively high value to spatial locations likely to result in success (i.e., cluster of jets) and low value locations that would result in a costly miss (e.g., allied operators positioned near jets). The operator should then aim for a location inside the airfield that corresponds to the maximum of the expected gain function while avoiding areas outside of the airfield near allied operators (red dots). D) Without necessarily computing sensory and motor variance statistics, the operator may simply decide to aim for some general location. For example, the operator may mentally divide the airfield (light gray dotted lines) and the upper left quadrant (green rectangle).

## 1.2 Algorithms of spatial decisions

### 1.2.1 Statistically rational sensorimotor integration

The first piece of information needed to make a sensorimotor decision on a visual target is a representation of the spatial distribution of sensory input. Consider a very simple case of a spatial decision where there is no prior information about where to select or any other competing sensory distribution. For instance, in Figure 1.1a, an individual executing a drone strike only needs the spatial positions of enemies in order to determine the optimal target location of the strike. This kind of spatial decision-making follows one principle of optimal control theory, which is one approach that describes human sensorimotor planning and execution (Todorov, 2004; Todorov & Jordan, 2002). Specifically, an individual can use a maximum likelihood estimation process to estimate the mean and variance of the input distribution so that the spatial decision is optimized by centering a selected action on the distribution's mean.

In a scenario where multiple drone strikes are to be made, the complexity of input into the spatial decision may increase as an operator considers their experience on prior strikes. So, how might the operator select the best location for a drone strike when they have to consider their success on previous strikes along with their estimates of sensory input variance? One strategy is to decide where to aim by estimating a likelihood function of success given the incoming sensory signals, and incorporating this likelihood with prior information based on previous successes and failures (Berniker & Kording, 2011; Knill & Pouget, 2004; Kording & Wolpert, 2006). In the drone strike example (Figure 1.1B), combining the likelihood with prior information allows the operator to use past experience to optimize his current aiming decision when sensory signals become noisy, e.g., sudden dust storm blurs video feed. Assuming that its

variance is stable, the prior becomes increasingly relied upon to optimize the sensorimotor decision as uncertainty in estimates of the likelihood grows.

Over the last decade, many studies have provided evidence that people rely on these sort of Bayesian dynamics when making spatially guided sensorimotor decisions (Bejjanki, Knill, & Aslin, 2016; Berniker & Kording, 2011; Fernandes, Stevenson, Vilares, & Kording, 2014; Grau-Moya, Ortega, & Braun, 2012, 2016; Hudson, Wolfe, & Maloney, 2012; Kording & Wolpert, 2006; Kwon & Knill, 2013; Orbán & Wolpert, 2011; Wei & Kording, 2010). For example, Bejjanki, Knill, and Aslin (2016) had participants perform a reaching task where the location of a hidden target on a touchscreen was indicated by a cloud of dots that could be used to estimate the target location. The target location was sampled randomly from a mixture of two Gaussian distributions (i.e., the prior). The dot cloud was comprised of eight dots sampled from a Gaussian distribution (i.e., the likelihood) and took on one of three different standard deviations across experimental conditions. Participants received numerical scores based on the accuracy of each reach endpoint. Modeling of participant behavior showed that they combined feedback with estimates of the target prior and likelihood in a Bayesian manner. This finding indicated that participants learned to optimize their estimates (i.e., maximize the posterior estimation) of the hidden target under multiple degrees of visual uncertainty. Indeed, as the variability of the likelihood increased, participants more heavily weighted their prior to maximize their posterior estimates of the target location, which is consistent with the predictions of Bayes theory in sensorimotor contexts (Franklin & Wolpert, 2011; Kording & Wolpert, 2006; Verstynen & Sabes, 2011; Wolpert, 2007). While maximum likelihood and Bayesian estimation processes provide optimal solutions to spatial decisions by respectively using estimates of sensory input or

a combination of sensory input and prior distribution variance, neither can fully account for how humans can make spatial decisions under risk.

### 1.2.2 Spatial decisions in risky contexts

Consider a situation where the operator must execute a strike on enemy targets when allies are nearby, adding an element of risk to the spatial decision. Within the statistical decision theory framework (Berger, 1985; Maloney & Zhang, 2010), the maximum expected gain model (Trommershäuser et al., 2003a; Trommershäuser, Maloney, & Landy, 2003b; Trommershäuser et al., 2008) provides one explanation for how spatial estimates can be performed under risk, i.e., gains and losses. For instance, in accord with the overall goal of striking enemy targets, the operator may associate a high positive value with the spatial locations of enemies. In contrast, a very low negative value may be assigned to the locations of allies in close proximity to enemy targets. Taking these costs into account, the operator can decide where to aim by attempting to avoid spatial locations with low value and focusing on high value locations to maximize his expected gain.

Many studies have provided confirmatory evidence for the idea that people estimate a spatial value function in ballistic reaching contexts. One such popular task involves having participants point to a briefly presented stimulus comprised of a small target circle that is visually overlapped by one or more non-target circles (Meyer, Abrams, Kornblum, Wright, & Smith, 1988; Neyedli & Welsh, 2013, 2014, 2015; Trommershäuser, Gepshtain, Maloney, Landy, & Banks, 2005; Trommershäuser, Landy, & Maloney, 2006; Trommershäuser et al., 2003a, 2003b; Wu, Trommershäuser, Maloney, & Landy, 2006). Participants must reach to the

target circle, typically within 700-800ms of stimulus onset, to gain a specified number of points on each trial. On some conditions, a point loss is incurred for reach endpoints that fall within the boundary of the non-target, or penalty, circle. The distance between the center of the target and penalty circles is also manipulated across trials or blocks to change the spatial boundaries of the target region. This distance manipulation thus changes the available space in the stimulus for gain, or reward. These risky ballistic reaching experiments consistently show that introducing penalty conditions causes participants to shift, or bias, their selections of the target circle away from the penalty circle to minimize the probability of losses (Meyer et al., 1988; Neyedli & Welsh, 2013, 2014, 2015; Trommershäuser et al., 2003a, 2003b; Wu et al., 2006).

Trommershäuser and colleagues (2003a, 2003b) developed a maximum expected gain model that incorporated estimates of motor variability for each participant to predict observed spatial selection bias (Trommershäuser et al., 2003a, 2003b). Two primary assumptions of the maximum expected gain model are that motor variance is approximately Gaussian, and the final decision relies on a weighting function that evaluates the spatial distributions of the target and penalty circles, respectively (Trommershäuser et al., 2003a, 2003b). The weighted probability distribution functions over the mean (i.e., center) of the target and penalty circles can be combined linearly to estimate a cost function, or landscape. Thus, the peak of this cost function corresponds to the spatial location in the stimulus that a participant should aim for to maximize expected gain. Across a variety of ballistic reaching experiments, human participants performed indistinguishably from an “ideal observer” model that accounts for both motor and sensory variability in a statistically principled manner based on the maximum expected gain model (Gepshtain, Seydell, & Trommershäuser, 2007; Trommershäuser et al., 2005, 2006, 2003a,

2003b; Wu et al., 2006). However, even under the same spatial constraints (i.e., target and penalty circle overlap), rather than minimize their motor variance in a statistically optimal way, people bias their reach targets further away from the penalty circle as penalty values increase (Neyedli & Welsh, 2013, 2014; Trommershäuser et al., 2006, 2003a, 2003b). These findings confirm that humans can spatially estimate risk and incorporate these risk estimates with internal estimates of motor variability to bias spatial decisions so as to minimize potential losses.

By associating values with different spatial locations, people can develop weights that correspond to the target and non-target, or penalty, regions of the stimulus input distributions used in the previously described maximum expected gain function. In particular, in situations wherein value-based feedback is provided following an action selection, reinforcement learning theory provides the computational framework for describing how the feedback on an action decision outcome can be used to adaptively adjust future selection behavior (Sutton & Barto, 1998). A hallmark of reinforcement learning in observable behavior is a trend toward the selection of an optimal choice over several trials of a given task.

In the ballistic reaching tasks discussed here, a gradual increase in the proximity of reach endpoints to an optimal location within the spatial target would signify the occurrence of reinforcement learning. Indeed, Neyedli and Welsh (2013) showed that participants performing the ballistic reaching task described above (Trommershäuser et al., 2003a), decreased their bias away from the penalizing region over several blocks of reaching trials. This resulted in a higher probability of selecting the optimal location within the target region and a greater overall number of points accumulated across experimental blocks (Neyedli & Welsh, 2013). Though many earlier ballistic reaching experiments using similar stimuli showed no evidence of such learning

effects (Trommershäuser et al., 2008), Neyedli and Welsh (2013) argued that those results were likely due to overtraining individuals before they performed the experimental task (Neyedli & Welsh, 2013). Thus, these findings suggest that reinforcement learning processes may indeed occur at the earliest stages (i.e., before extensive training) of spatially-guided movement decisions despite impoverished prediction error signals. Continuing to explore the impact of the robust sensory and reward prediction errors on sensorimotor control and learning can provide insight into how that information is used during spatial decisions.

### 1.3 Subjective estimates of multiple kinds of variability affect spatial decisions

One consistency among all of these theoretical framings of spatially based sensorimotor decisions presented thus far is an assumption that implicit sensory signals and motor plans are integrated in processes to optimize decision outcomes. However, several lines of evidence conflict with an assumption of strictly implicit information is processed during spatial estimations. For example, recent studies suggest that humans make suboptimal, or often irrational, sensorimotor decisions, particularly in explicit contexts of risk (Nagengast, Braun, & Wolpert, 2010; O'Brien & Ahmed, 2016). In a 2016 study by O'Brien and Ahmed, participants executed whole body leaning or arm reaching movements to earn points by controlling the proximity of a cursor to the edge of a virtual cliff presented on a computer screen (O'Brien & Ahmed, 2016). On some task conditions, penalties were incurred for cursor movements that traversed the cliff edge. When human performance was compared with a model based on optimal control theory (Nagengast et al., 2010; Todorov & Jordan, 2002) and another model based on cumulative prospect theory (Jarvstad, Hahn, Rushton, & Warren, 2013; Tversky & Kahneman,

1992; Wu, Delgado, & Maloney, 2009), participants exhibited risk-seeking movement behavior--sometimes letting the cursor fall over the cliff edge. This “irrational” risk-seeking behavior was significantly greater than either model predicted as the optimal, or rational, behavior based on both implicit estimates of sensorimotor noise and the weighting of explicit expected reward and penalty associated with movement decision outcomes. Importantly, O’Brien and Ahmed (2016) showed that individuals make inaccurate subjective judgments of their own motor variability during risky spatial decisions, resulting in a deviation from the optimal action selection that should emerge from a statistically rational process.

### 1.3.1 Sensory input estimates

A critical assumption of statistically rational models of sensorimotor control is that the brain reliably and accurately estimates the structure of both sensory and motor noise (Berniker & Kording, 2011; Kording & Wolpert, 2004, 2006; Maloney & Zhang, 2010; Todorov, 2004; Todorov & Jordan, 2002; Trommershäuser et al., 2008). However, recent work has shown that people tend to make inaccurate subjective estimations of input noise related to the statistics of sensory stimuli (Beck, Ma, Pitkow, Latham, & Pouget, 2012; Juni, Gureckis, & Maloney, 2016). Juni and colleagues (2016) had participants reach to a hidden target whose location on a touchscreen could be estimated from a sequentially presented cloud of dots taken one by one from a Gaussian distribution at each participant’s discretion (Juni et al., 2016). Participants oversampled sensory information about the stimulus before executing their reaches, deviating from the optimal sampling behavior estimated for an ideal observer (Juni et al., 2016). Though more dots yielded more reliable estimates of the target location, oversampling resulted in a

failure to maximize expected gain--due to points lost for each dot requested before executing the reach on a trial. Along with requesting a supra-optimal number of dots, participants appeared to stop requesting dots only once the variance of the dot cluster density was significantly lower than the density predicted by an ideal observer model (Juni et al., 2016). Here, oversampling to reduce uncertainty is quite consistent with a heuristic bias commonly observed during risky economic choice decisions (Tversky & Kahneman, 1992; Wu et al., 2009), where participants prefer a more certain choice with low value over a higher value choice with greater uncertainty, and thus fail to maximize expected gain across multiple decisions.

### 1.3.2 Motor output estimates

Imprecise subjective estimates are not restricted to perceptual characteristics of sensory input, but also to estimates motor output variability. To test whether individuals could accurately estimate the variance of their own motor output, Zhang and colleagues (2013) had participants train on ballistic reaches to circular targets, and then indicate their preference for hitting either a vertical or horizontal rectangle based on each participant's subjective estimate of their motor variance (Zhang, Daw, & Maloney, 2013). The experimental stimuli were designed so that the true distribution of reach endpoints for all participants would be anisotropic--elongated on the vertical axis; however, participants did not indicate a preference for vertically oriented rectangles over horizontal rectangles as expected. Rather, the authors found that participants ascribed an isotropic (i.e., bivariate Gaussian) distribution to their reach endpoints and thus performed non-optimally on non-motor decisions that required accurate estimates of their motor variance.

In a follow-up study (Zhang, Daw, & Maloney, 2015), participants first performed multiple ballistic reaching tasks. On a subsequent non-motor task, participants were then asked to choose which of two arrangements of rectangular targets they thought was easier to hit. By modeling reaching and choice behavior, Zhang and colleagues confirmed that actual motor output variability was best fit by a unimodal Gaussian probability distribution function. However, participant performance on the choice task, where no actual movements were made, indicated that their internal estimates of variability were multimodal and better captured by mixtures of uniform distributions (Zhang et al., 2015). More importantly, the expected position based on the uniform distributions of estimated motor output variance did not track the expected position if the decision is assumed to be based on the Gaussian distribution of actual reach endpoint variability, indicating that participants misrepresented probabilistic information about their own motor output, as is consistent with previous (Wu et al., 2009) and more recent findings (O'Brien & Ahmed, 2016). Based on this evidence Zhang and colleagues (2015) argued that participants may have used a computational shortcut (i.e., heuristic) to approximate the maximum of actual motor variability rather than statistically optimize their decisions (Zhang et al., 2015). In other words, if humans do not accurately represent the statistical distributions of task-relevant noise, then this complicates the assumption of statistically rational models that the actual structure of sensory input is used to optimize motor output.

Returning to the drone strike example, since the blast radius of the missile explosion is necessarily larger than the missile itself, the operator has some room for error during his aiming decision. As such, the operator does not necessarily have to maximize his precision (i.e., minimize aiming variability) to damage some number of jets. To determine whether people

minimized and maintained motor variance across many ballistic reaches, Jarvstad and colleagues (2014) presented participants with two simultaneously presented circular targets that differed in size and location on a touchscreen (Jarvstad, Hahn, Warren, & Rushton, 2014). They found that participants did not opt to constrain their motor variability for reaches to the larger target to the same degree that they were capable of on reaches to the smaller target. Furthermore, participants were able to minimize reach endpoint variability equally for small and large target circles when explicitly instructed to aim for the center of either size target in a control experiment. These findings directly conflict with the assumption of both optimal control theory and statistical decision theory that humans maximize motor output variance over task-relevant sensory input (Todorov, 2004; Todorov & Jordan, 2002; Trommershäuser et al., 2003a, 2003b). The results of Jarvstad and colleagues (2014) clearly show that if a high degree of control is not required, people can relax constraints on motor variance to execute an action that may not be optimal, but good enough for a task (i.e., satisfice). If people satisfice on sensorimotor tasks based on explicit task contexts, then controlling motor output variability may be driven by explicit strategic necessity, rather than implicit statistically rational optimization processes.

### 1.3.3 Probability distortions

In addition to inaccurate subjective estimates of sensory and motor variability, people distort outcome probabilities on risky economic choices (Kahneman & Tversky, 1979; Tversky & Kahneman, 1992), which also appears to occur during sensorimotor decisions with risky prospects (O'Brien & Ahmed, 2016; Wu et al., 2009). To illustrate probability distortion behaviorally, Wu and colleagues (2009) showed that a visuomotor decision making task can be

mathematically equivalent to an economic choice task, or lottery (Wu et al., 2009). Participants attempted to maximize point gain across a series of trials by executing ballistic reaches to a narrow target bar presented vertically between two wider bars worth fewer points. Using the variance of reach endpoints for each participant, the authors constructed a set of motor lottery decisions based on the probabilities of hitting the narrow target bar, either of the wider bars, or missing the stimulus completely. Wu and colleagues found that participants centered their reach endpoints on the narrow target bar to maximize gain across trials, demonstrating risk seeking behavior since there is a lower probability of hitting the narrow target. However, participants chose lotteries with lower overall payouts but greater chances of winning, which corresponded with the probability of hitting the wider bars on the motor task. This showed that people were risk averse on the lottery task even though both types of decisions were mathematically equivalent. The findings of Wu and colleagues were consistent with cumulative prospect theory (Tversky & Kahneman, 1992) and showed that people distort probabilities on both non-spatial (e.g., economic) and spatial decisions, although not necessarily in the same way. Critically, the results provide evidence that people do not make accurate subjective estimates of sensory input or their own motor output, violating assumptions of statistical decision theory (Trommershäuser et al., 2008). Despite evidence that heuristic-like strategies are used during sensorimotor decisions, it is still unclear whether these explicit strategies are a part of implicit computations on perceptual noise, or if they constitute independent decision processes.

### 1.3.4 Explicit cognitive strategies impact implicit sensorimotor decisions

People adapt sensorimotor motor decisions both implicitly and explicitly. Implicit adaptations rely on the use of sensory signals to minimize error. Alternatively, a person can make an explicit cognitive decision to aim for a specific spatial target based on task instructions, which can lead to the same outcome as implicit, sensory-based adjustments. Taylor and Ivry (2011) showed that when the visual feedback on a reach endpoint to a circular target was rotated by 45 degrees in a counterclockwise direction, participants shifted their endpoints in a clockwise direction to minimize spatial error on the target (Taylor & Ivry, 2011). In one task condition, participants only used visual error-based feedback that led to an implicit adaptation process that reduced error very slowly over many trials. On a second condition, the experimenter gave participants task instructions to adjust reaches 45 degrees clockwise, which resulted in an immediate reduction in error on the first trial after visual feedback was rotated counterclockwise. More recently, Bond and Taylor (2015) used a variety of ballistic reaching tasks to further investigate the role of explicit strategy in sensorimotor adaptation (Bond & Taylor, 2015). On this task, participants were asked to verbalize their intended aiming decision, i.e., explicit strategy, to hit a spatial target within a circular array. The participants adapted rapidly to abrupt rotations in target location, visual feedback on cursor position, and the presence of landmarks in the array to execute successful reaches (Bond & Taylor, 2015). These findings show that sensorimotor control and learning have two dissociable components (Taylor & Ivry, 2011, 2012; Taylor, Krakauer, & Ivry, 2014), which are either slow, rigid, and driven by sensory error (i.e., implicit) or fast, flexible, and cognitively-based (i.e., explicit) (Bond & Taylor, 2015; McDougle, Bond, & Taylor, 2015).

#### 1.4 Neural mechanisms of spatial decisions

In the preceding sections of this chapter, I have discussed several experiments framed from the perspective of both normative models of sensorimotor control and more descriptive evaluations of value-based spatial decision-making behavior. The theories underlying these paradigms and models assume that the brain must represent several key components to execute spatially guided movement decisions. First, the brain must represent the spatial distribution of visual input to identify target stimuli and/or the locations in which they appeared. The second and third components are a set of possible actions directed to spatial stimuli and the signals that indicate a selected action from that set. In nearly all of the experiments described, some form of feedback that corresponded to target hits or misses was given to participants. Thus, the values of spatial targets and locations relative to non-target stimuli and locations must also be represented. Lastly, it follows that the decision outcome (e.g., reach endpoint error to the target or number of points received on a reach trial) will also be reflected by neural responses. Evidence from nonhuman primate neurophysiology and histology as well as human neuroimaging shows that activity in a variety of highly distributed and interconnected brain regions is tuned to different aspects of spatially guided movement decisions. This kind of functional brain network, or circuit of regions, provides a neurologically plausible mechanism for exploring a potential interaction between implicit computational and explicit cognitive processes that underlie observable spatially guided decision behavior.

#### 1.4.1 Multiple brain regions represent different components of spatial decisions

Neural activity in distributed cortical and subcortical regions contribute to unique aspects of spatially guided movements. Typically, the studies that report these findings record neuronal spike rate within single units or populations of neurons of monkeys performing a spatial delayed-response task where they must saccade (Chafee & Goldman-Rakic, 2000; Colby & Goldberg, 1999; Curtis, 2006; Funahashi, Bruce, & Goldman-Rakic, 1989; Gottlieb, 2002; Hoshi & Tanji, 2006; Kakei, Hoffman, & Strick, 2001; McGinty, Rangel, & Newsome, 2016; Ptak, 2012) or reach to a briefly presented visual stimulus (Buneo & Andersen, 2006; Cisek & Kalaska, 2005; Colby, 1998; Crammond & Kalaska, 1994; Gottlieb, 2007; Romo, Hernández, & Zainos, 2004; Schultz & Romo, 1992; W. Schultz, Tremblay, & Hollerman, 2000; Wise, di Pellegrino, & Boussaoud, 1996; Yamagata, Nakayama, Tanji, & Hoshi, 2009). Colby and Duhamel (1996) recorded from neurons in lateral and medial regions of the intraparietal sulcus (LIP and MIP) that are respectively associated with saccades and arm reaching while monkeys viewed brief presentations a single visual target stimulus that appeared in different spatial locations on a screen (Colby & Duhamel, 1996). Both LIP and MIP neurons increased phasic spiking activity when a visual target was presented within the receptive fields of each neuron type, as well as when a saccade (LIP neurons) or a reach (MIP neurons) was made to the target for a fluid reward. Furthermore, both neuron types showed sustained tonic activity between stimulus presentation and movement execution, even when the stimulus was not visible. These findings show that spiking activity in parietal neurons can represent and maintain the distribution of behaviorally relevant visuospatial input that appears within the receptive fields of those neurons (Colby & Duhamel, 1996; Colby & Goldberg, 1999; Curtis, 2006; Gottlieb, 2002; Ptak,

2012). This activity can also contribute to the execution of movements toward the location of a visually presented spatial stimulus (Buneo & Andersen, 2006; Colby, 1998; Gottlieb, 2007).

While parietal activity can represent the spatial location of visual target stimuli, frontal and prefrontal cortical regions represent a set of actions toward spatial locations and the selection of a particular action toward target stimuli and locations. For instance, a tonic burst of spiking activity in dorsal premotor cortex (PMd) neurons is observed when a visual stimulus is presented in the spatial location of their preferred movement direction (Crammond & Kalaska, 1994; Yamagata et al., 2009). Crammond and Kalaska (1994) observed this increase in tonic spiking activity in PMd using a paradigm where monkeys executed reaches to a target stimulus or a cued target location where no visual stimulus appeared, which indicates that PMd activity corresponds to movements toward target spatial locations that do not necessarily have to be visible at any point during or after a movement (Crammond & Kalaska, 1994). Separate populations of PMd neurons can also represent multiple reaching actions before one is selected for execution. In cases where more than one visual stimulus is presented, PMd neurons that are directionally tuned for movements to each potential target location all increase their spiking activity (Bastian, Riehle, Erlhagen, & Schöner, 1998; Cisek & Kalaska, 2005; Dekleva, Ramkumar, Wanda, Kording, & Miller, 2016). Cisek and Kalaska (2005) found that the presentation of a non-spatial cue that signaled the target location resulted in a suppression of spike activity in PMd neurons that encoded movements toward non-target locations so that only the movement to the target location was performed (Cisek & Kalaska, 2005). Other research exploring the function of ventral premotor cortex (PMv), show populations of neurons also encode the spatial location of a visible target (Hoshi & Tanji, 2006; Kakei et al., 2001), and increase phasic spiking activity

during the initiation (Yamagata et al., 2009) and successful execution (Rizzolatti et al., 1987) of a reach to a visible spatial target. Together, these separate lines of work examining the functions of PMd and PMv provide strong evidence that neural activity in premotor cortex can map a set of actions to visible spatial stimuli and target locations (Cisek & Kalaska, 2010; Steven P. Wise, Boussaoud, Johnson, & Caminiti, 1997).

Whether a movement must be made toward a visual stimulus with particular target features (e.g., shape or color) or spatial location, a single action must be selected from a set of actions to achieve the particular goal of a spatial task. Dorsolateral prefrontal cortex (DLPFC) is implicated in the selection of task-relevant spatial decision behaviors (Funahashi et al., 1989; Hoshi, Shima, & Tanji, 1998; Kubota & Funahashi, 1982; Quintana, Yajeya, & Fuster, 1988; Rainer, Asaad, & Miller, 1998; Yamagata, Nakayama, Tanji, & Hoshi, 2012) and is theorized to maintain task-relevant (e.g., rule-based) information as a general mechanism of controlling goal-directed behavior (Dixon & Christoff, 2014; Hoshi, 2006; Miller & Cohen, 2001; Ridderinkhof, van den Wildenberg, Segalowitz, & Carter, 2004). Hoshi and colleagues (1998) monitored multiple populations of neurons in DLPFC for their responses to the shape, location, or both shape and location of a spatial target visually presented to monkeys on a delayed-response task (Hoshi et al., 1998). There were two trial types, or experimental contexts, wherein the monkey had to execute a reach to either a target that had the same shape as a previously presented cue stimulus, or to a stimulus that appeared in a cued location. Separate populations of neurons tuned to either target shape or spatial location selectively increased phasic spiking activity immediately before a reach was executed to the preferred stimulus or location based on the cue (Hoshi et al., 1998), which is consistent with earlier work showing that

DLPFC activity gradually increases before the phasic spiking that precedes a goal-directed movement (Kubota & Funahashi, 1982). By representing the relevant aspects (i.e., visual features or location) of a spatial target needed to execute a successful context-specific movement, DLPFC neurons facilitate the selection of a goal-directed action from a set of possible action choices (Hoshi, 2006; Miller & Cohen, 2001; Ridderinkhof et al., 2004).

One potential feature implicit to a spatial target or location is its value relative to other visible non-target stimuli or locations. Value information used to identify and guide selection decisions on visually presented target stimulus is represented by neurons in the orbitofrontal cortex (OFC) (Kringelbach & Rolls, 2004; Noonan, Kolling, Walton, & Rushworth, 2012; Rudebeck & Murray, 2011; Wallis, 2007). Recently, neural activity in OFC regions have also been shown to respond in a spatially-tuned fashion, indicating the distance of gaze positions away from the cued spatial location of a target (McGinty et al., 2016). McGinty, Rangel, and Newsome (2016) identified separate populations of neurons in monkey OFC that selectively responded to a set of one of three visually distinct stimuli that were associated with unique amounts of juice as a reward. Similar to the previously discussed paradigms, McGinty and colleagues observed neural responses in the cortical region of interest leading up to the execution of spatially guided movement. However, they used a novel free viewing paradigm to also measure eye gaze during a four second viewing period between the presentation of a cue that remained on screen and the delivery of a reward for fixating on the cue at the end of the viewing period. A tonic burst of activity was observed in selectively active OFC neurons when a monkey initially fixated its gaze on a cue and, quite interestingly, the spike rate of responsive neurons was negatively correlated with gaze proximity to the spatial location of the cue. More

specifically, OFC neurons decreased spatially-tuned spiking activity proportionally as the monkey fixated on locations that were further away from the cue, which provides some of the first evidence that neurons in OFC can encode the spatial location of a visual stimulus. It is also important to note that discrete subsets of OFC neurons that responded to unique stimuli associated with different relative values exhibited similar patterns of spiking behavior (McGinty et al., 2016; Strait et al., 2016), which highlights a potential mechanism for how the brain represents multiple visual stimuli with distinct values simultaneously.

Along with the cortical regions discussed thus far, a subcortical region, namely the striatum, has also been shown to exhibit spatially-tuned neural activity on visually guided motor decisions. In a spatial sequencing study by Kermadi and Joseph (1995), neural activity in the caudate nucleus of monkeys that sat facing a panel that had three buttons with fixed spatial positions programmed to light in different sequences of one, two, or three buttons (Kermadi & Joseph, 1995). After viewing a sequence, monkeys had to press the buttons in the same order to receive a juice reward. Amidst findings that some neural activity in the caudate was selective for entire sequences of saccades and reaches to target buttons, the authors also observed neurons with non-selective spiking activity, that is, some caudate neurons show phasic firing only for a button in a specific spatial location regardless of its temporal position in the sequence (Kermadi & Joseph, 1995). The spatially-tuned activation in the caudate reported by Kermadi and Joseph (1995) is consistent with observations of sustained phasic activity in the caudate in response to a nonspatial stimulus that cued the spatial target location of a future eye movement (Hikosaka, Sakamoto, & Usui, 1989). While these studies focused on the caudate nucleus, the putamen is also involved in generating goal-directed movements in response to visuospatial cues (Schultz &

Romo, 1992), particularly once movement plans become habitual actions (Balleine & O'Doherty, 2010; Graybiel, 2008). Another critical, and widely accepted, role of the striatum is reinforcement learning (Doya, 2008; Houk & Adams, 1995; Lee, Seo, & Jung, 2012; Schultz, 2016), which uses feedback on decision outcomes to adaptively adjust future behaviors (Sutton & Barto, 1998). Through the association of rewards to spatial locations, the striatum is implicated generally in spatial cognition (Burgess, 2008) and more specifically in locating and executing a movement toward a rewarding spatial target (Gottlieb, Hayhoe, Hikosaka, & Rangel, 2014; Retailleau, Etienne, Guthrie, & Boraud, 2012).

Several cortical and subcortical regions of the brain play unique and complementary roles in representing the major components of spatial decisions. Recordings from parietal (Buneo & Andersen, 2006; Colby & Goldberg, 1999; Gottlieb, 2002), premotor (Cisek & Kalaska, 2010; Wise et al., 1997), dorsolateral prefrontal (Hoshi, 2006; Miller & Cohen, 2001; Ridderinkhof et al., 2004), orbitofrontal (Kringelbach & Rolls, 2004; Noonan et al., 2012; Rudebeck & Murray, 2011; Wallis, 2007), and striatal (Burgess, 2008; Gottlieb et al., 2014; Retailleau et al., 2012) neurons show patterns of spiking activity that encode the location of spatial targets and contribute to goal-directed movements toward targeted locations. Overall, these neurophysiological data provide strong evidence that disparate regions of the neocortex and striatum show spatially-tuned activity that contribute to visually guided movement decisions to spatial targets.

1.4.2 Brain areas involved in spatial decisions are highly interconnected locally and globally

Cortical regions involved in spatial decisions have strong, reciprocal intracortical and corticocortical connectivity. Locally, short range white matter pathways within parietal, premotor (Schmahmann & Pandya, 2006), prefrontal, and orbitofrontal (Yeterian, Pandya, Tomaiuolo, & Petrides, 2012) cortices connect neurons within and across architectonic boundaries (Schmahmann & Pandya, 2006). Lateral premotor, and prefrontal regions exhibit a common functional divide between dorsal and ventral aspects of each region, wherein dorsal neurons encode spatial and directional information, while ventral regions encode information about the identity or features (e.g., color or shape) of visual stimuli (Hoshi, 2013; Yamagata et al., 2012). This local topographic organization of visual input to premotor and dorsolateral prefrontal cortices is consistent with the more global, dual routes of the visual stream through occipitoparietal pathways dorsally and occipitotemporal pathways ventrally (Goodale & Milner, 1992; Mishkin, Ungerleider, & Macko, 1983). The architectonic parcellations of orbitofrontal cortex fall along either an anterior to posterior axis where neurons represent abstract (e.g., points and money) and concrete (e.g., food, odors, sounds) reward information, respectively, or a medial to lateral axis where medial OFC neurons track the value of reinforcement signals and lateral OFC neurons track punishment signals that may result in goal-directed adjustments to behavior (Kringelbach & Rolls, 2004; Noonan et al., 2012). Neurons in anterior, posterior, medial, and lateral regions of OFC are highly interconnected to neurons in all other regions (Yeterian et al., 2012). Functionally, the high degree of intracortical connectivity within parietal, premotor, lateral prefrontal, and orbitofrontal regions comprise local circuitry seem to allow for a unified (i.e., spatial- and feature-based) representation of visual stimuli.

Histological tracer (Schmahmann & Pandya, 2006; Yeterian et al., 2012) and human neuroimaging (Catani & de Schotten, 2012; Fernandez-Miranda et al., 2012; Wakana, Jiang, Nagae-Poetscher, van Zijl, & Mori, 2004) studies have also shown that long range white matter fasciculi connect disparate pairs of cortical regions. The previously cited reviews are strongly recommended for in-depth descriptions of these pathways in human and nonhuman primates. Reciprocal connectivity is present between parietal cortex and both premotor and lateral prefrontal regions via the superior longitudinal fasciculus (SLF), which has three subcomponents: SLF I, SLF II, and SLF III (Martino et al., 2013). SLF I connects caudal regions of the superior parietal lobule and dorsal premotor cortex, while SLF II consists of fibers connecting the caudal inferior parietal lobule with dorsal premotor cortex and DLPFC, and SLF III connecting rostral areas of inferior parietal lobule with DLPFC (Cavada & Goldman-Rakic, 1989; Schmahmann & Pandya, 2006). Both ventral premotor cortex and DLPFC are connected with lateral OFC via SLF I (Barbas, 2000; Cavada, Company, Tejedor, Cruz-Rizzolo, & Reinoso-Suarez, 2000; Schmahmann & Pandya, 2006). Premotor cortex and DLPFC are also strongly interconnected (Barbas, 2000; Hoshi, 2006; Lu, Preston, & Strick, 1994). Though the distribution of connectivity in parietal cortex is somewhat sparse, rostral and caudal regions of the inferior parietal lobule are connected with OFC (Cavada et al., 2000; Selemon & Goldman-Rakic, 1988). Along with robust local connectivity within cytoarchitectonic boundaries, long range white matter fasciculi relates all pairings of presently reviewed cortical regions, i.e., parietal, premotor, DLPFC, and OFC (Catani & de Schotten, 2012; Fernandez-Miranda et al., 2012; Schmahmann & Pandya, 2006; Wakana et al., 2004; Yeterian et al., 2012). Another important feature of this connectivity is that projections from each cortical

region share common targets with other cortical regions in the circuit (Hoshi, 2006; Schmahmann & Pandya, 2006; Selemon & Goldman-Rakic, 1988; Yeterian et al., 2012). The global level of corticocortical interconnectedness of this network further supports its role in integrating the representations of visual input, action selection, and stimulus values that are needed for spatially-guided movement decisions.

#### 1.4.3 Structural and functional connectivity converge in the striatum

Though the corticocortical connectivity described thus far provide one way of combining information about spatial targets and locations as well as specifying goal-directed movements (Ridderinkhof et al., 2004), the striatum plays a critical part in spatial decisions by releasing desired actions toward target stimuli or locations (Kermadi & Joseph, 1995; Schultz & Romo, 1992) and using feedback to adjust upcoming decisions via reinforcement learning (Doya, 2008; Houk & Adams, 1995; Lau & Glimcher, 2007; Lee et al., 2012; Wolfram Schultz, 2016; Sutton & Barto, 1998). Given that the striatum only receives direct projections from the neocortex (Alexander, DeLong, & Strick, 1986; Haber, 2016; Kemp & Powell, 1970), it is ideally situated in the brain to integrate information about spatial decisions to execute goal-directed actions and use outcome feedback to update selected movements. While the organization of basal ganglia circuitry was largely thought to be parallel and segregated (Alexander et al., 1986; Kemp & Powell, 1970), there is a substantial degree of overlapping and integrated corticostriatal projection terminations (Averbeck, Lehman, Jacobson, & Haber, 2014; Haber, 2003; Selemon & Goldman-Rakic, 1985). For example, premotor cortex, DLPFC, and OFC all project to similar anterior regions of the caudate nucleus and putamen (Averbeck et al., 2014; Haber & Knutson,

2010), and parietostriatal pathways have separately been found to project to those same striatal regions (Cavada & Goldman-Rakic, 1989; Selemon & Goldman-Rakic, 1988). This convergent corticostriatal connectivity identified by histological work in nonhuman primates has also been observed in a recent human neuroimaging study (Jarbo & Verstynen, 2015). Furthermore, patterns of resting state functional connectivity confirm the presence of correlated activity across these structurally connected cortical and striatal regions (Choi, Yeo, & Buckner, 2012; Jarbo & Verstynen, 2015). Given that resting state functional connectivity analysis prohibits any inferences task-based functional activation, Pauli and colleagues (2016) conducted a meta-analysis on 5,809 fMRI studies to identify striatal regions involved in specific categories of psychological processes (Pauli et al., 2016). The authors parcellated the striatum into five functionally distinct subregions with one so-called “action value zone” that encompassed anterior aspects of the caudate and putamen, bilaterally (Pauli et al., 2016). Critically, the action value zone is situated in regions of the striatum that are the site of convergent cortical inputs from frontal and parietal regions involved in spatial decision making (Averbeck et al., 2014; Haber & Knutson, 2010; Jarbo & Verstynen, 2015; Selemon & Goldman-Rakic, 1985, 1988). Taking together these observations of structural and functional connectivity, tasks that require value-based, spatially-guided movements should engage anterior regions of the striatum along with parietal, premotor, DLPFC, and OFC areas that represent each of the key components of a spatial decision (see Figure 1.2).

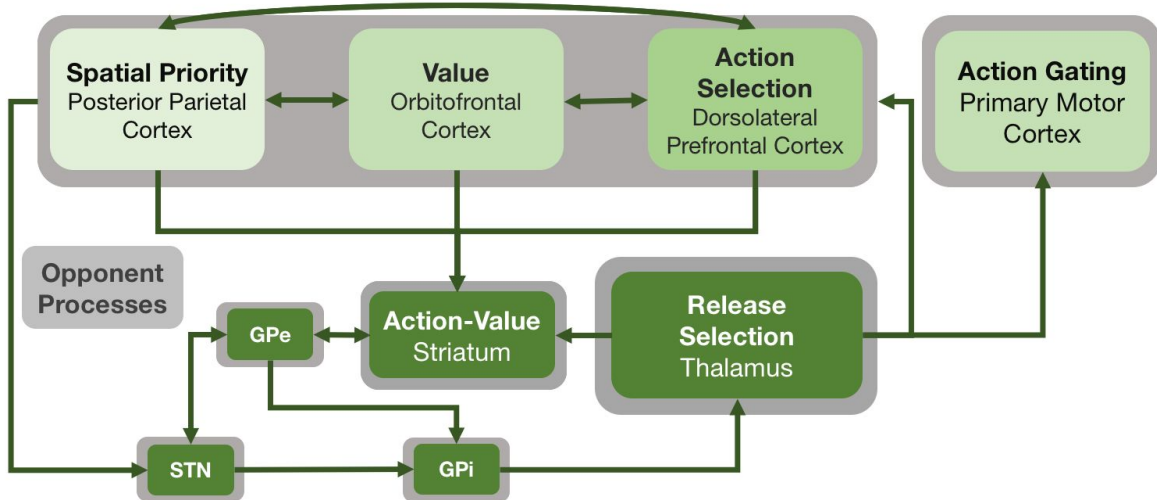


**Figure 1.2** Neural circuit model of a spatially guided movement decision. Arrows indicate the direction of neural signaling through the cortico-basal ganglia-cortical network. Bidirectional arrows indicate reciprocal connectivity between cortical and subcortical regions and nuclei. Top: Larger gray boxes indicate cortical areas with reciprocal connectivity within and between each region (light green boxes) and their respective functional roles in spatial decisions. For the purposes of this diagram, action gating in primary motor cortex is depicted separately from PPC, OFC, and DLPFC as its particular function in this circuit is carried out after the hypothesized integration of information from the other cortical areas. Bottom: Dark green boxes outline by gray boxes represent nuclei that comprise the basal ganglia. The striatum is the primary input to the basal ganglia that facilitates the control of downstream opponent processes (left small gray box) that mediate the release of a selected action from the thalamus to where the action itself is gated via primary motor cortex for execution.

## 1.5 Open questions and specific aims

Behaviorally, it remains unclear how estimates of sensory reliability and subjective value drive spatial decisions under risk. Additionally, the rostral striatum is ideally situated to integrate perceptual information, value, and executive action signals during risky spatial decision-making, however its role in driving value based spatial decisions remains poorly understood. As of yet,

the structure of this integrative corticostriatal action-value network in humans and its role in risky spatial decision-making is not fully determined.

To address these open questions this dissertation presents a series of studies wherein I 1) developed a set of novel behavioral experiments to establish the effects of spatial signals, value, and context during risky spatial decision-making processes, 2) confirmed the existence of an integrative corticostriatal network of convergent DLPFC, OFC, and PPC inputs in the human brain, and 3) examined activity modulation and action-value representations in the striatum. My dissertation projects combined diffusion weighted imaging (DWI), resting state fMRI (rsfMRI), task-related fMRI, and psychophysics experiments to delineate a neural mechanism of cognitive penetration, wherein the contextual framing of a risky outcome impacts perceptual estimation and action selection processes involved in value-based spatial sensorimotor decisions.

### 1.8.1 Specific Aims

This dissertation will address three specific aims.

Aim 1: Explore the interplay between sensory uncertainty, value signals, and subjective context on spatial sensorimotor decisions (Chapters 2 and 3). If the sensory uncertainty of a spatial target is increased, then selection bias away from a penalizing non-target cue will also increase. Also, if the subjective evaluation of feedback signals impacts selection behavior, then changes in the contextual framing of risk should modulate avoidance bias.

Aim 1.1: A previous value-based spatial decision task (Trommershäuser et al., 2003) will be adapted to focus on the impact of increased sensory uncertainty on target selection behavior under risk of point-based scoring penalties (Chapter 2).

Aim 1.2: A follow-up study will establish how changes in the contextual framing of risks, which impacts the subjective value of feedback signals, modulates avoidance bias during spatial judgments (Chapter 3).

Aim 2: Identify convergent corticostriatal connectivity that integrates multiple sources of information necessary for value-based action decisions. If the striatum integrates action-value information from functionally associated areas of OFC, DLPFC, and PPC, then white matter pathways from those cortical areas should converge in anterior striatal regions (Chapter 4).

Aim 2.1: Tractography on DWI data will be used to confirm convergent projections from OFC, DLPFC, and PPC into the “action-value” regions of the human striatum.

Aim 2.2: Analysis of rsfMRI data will then be used to verify the network’s (Aim 2.1) functional connectivity.

Aim 3: Confirm that a risky spatial decision-making task (Aim 1.2) engages all regions of the corticostriatal action-value network (Aim 2) (Chapter 5). If the network evaluates action-value, then changes in BOLD activation should track the level of cost associated with each task condition. Additionally, if the contextual framing of risks modulates action-value, then patterns

of BOLD activation representing different task contexts should be reflected in activity patterns in striatal action-value regions.

These specific aims will be explored over the course of four experimental chapters. In Chapter 2, I explore the interplay between sensory uncertainty, value signals, and subjective context on spatial sensorimotor decisions. Specifically, if the sensory uncertainty of a spatial target is increased, then selection bias away from a penalizing non-target cue will also increase. Also, if the subjective evaluation of feedback signals impacts selection behavior, then changes in the contextual framing of risk should modulate avoidance bias. A previous value-based spatial decision task (Trommershäuser et al., 2003) was adapted to focus on the impact of increased sensory uncertainty on target selection behavior under risk of point-based scoring penalties. A two-session follow-up study confirmed the reliability of the effects observed in the first study both within-subjects and between groups. A third study, discussed in Chapter 3, established how changes in the contextual framing of risks, which impacts the subjective value of feedback signals, modulates avoidance bias during spatial judgments.

Chapter 4 discusses the findings of a multimodal neuroimaging study that identified convergent corticostriatal connectivity that integrates multiple sources of information necessary for value-based action decisions. In that study, I tested the hypothesis that if the striatum integrates action-value information from functionally associated areas of OFC, DLPFC, and PPC, then white matter pathways from those cortical areas should converge in anterior striatal regions. Tractography on DWI data confirmed that convergent projections from OFC, DLPFC,

and PPC overlapped within "action-value" regions of the human striatum. A subsequent analysis of rsfMRI data was used to verify the network's functional connectivity.

Finally, Chapter 5 explores whether contextual signals during risky spatial decision-making modulate corticostriatal action-value network activation. In particular, I hypothesized that if the network evaluates action-value, then changes in BOLD activation should track the levels of condition-specific (i.e., no-penalty vs penalty) costs on spatial selections. Additionally, if the contextual framing of risks modulates action-value, then patterns of BOLD activation representing different task contexts (i.e., harm vs help) should be reflected by differences in activity patterns within striatal action-value regions. To address these hypotheses, I conducted an fMRI study using an adapted version of the behavioral task described in Chapter 3 to examine how the contextual framing of risk influences representational patterns of activity in the action-value striatum. More generally, I identify a network of cortical regions that encode differences between context and penalty conditions during risky spatial decision-making.

In the final chapter of this dissertation, I conclude with a critical review of the work presented and situate the findings within the broader literature in cognitive psychology, decision neuroscience, and moral psychology that explore contextual framing effects on risky decision-making behavior. I will discuss the limitations of each experiment as well as plans to address those limitations with future work examining the neural underpinnings of value-based action selection behavior during risky decision-making.

# Chapter 2

## Sensory uncertainty impacts avoidance during spatial decisions

*The following text has been adapted from Jarbo, Flemming, & Verstynen, 2017*

When making risky spatial decisions humans incorporate estimates of sensorimotor variability and costs on outcomes to bias their spatial selections away from regions that incur feedback penalties. Since selection variability depends on the reliability of sensory signals, increasing the spatial variance of targets during visually-guided actions should increase the degree of this avoidance. Healthy adult participants ( $N = 20$ ) used a computer mouse to indicate their selection of the mean of a target, represented as a 2D Gaussian distribution of dots presented on a computer display. Reward feedback on each trial corresponded to the estimation error of the selection. Either increasing or decreasing the spatial variance of the dots modulated the spatial uncertainty of the target. A non-target distractor cue was presented as an adjacent distribution of dots. On a subset of trials, feedback scores were penalized with increased proximity to the distractor mean. As expected, increasing the spatial variance of the target distribution increased selection variability. More importantly, on trials where proximity to the distractor cue incurred a penalty, increasing variance of the target increased selection bias away from the distractor cue and prolonged reaction times. These results confirm predictions that increased sensory uncertainty increases avoidance during risky spatial decisions.

## 2.1 Introduction

It is fabled that William Tell was forced to use an arrow to precariously shoot an apple placed atop his son's head. Successful completion of his task required Tell to optimally aim his crossbow for the high reward target, i.e., the apple, while avoiding an area with a very high penalty, i.e., his son's head (see also Trommershäuser, Maloney, & Landy, 2003). Situations like this can be complicated by environmental conditions. For instance, a thick fog settling into the square would increase the difficulty of Tell's aiming decision. The increased noise in the target estimation process would, in turn, reduce his accuracy and impact the likelihood of striking the apple.

In scenarios like these, where people must execute a visually guided movement with a potentially high cost on feedback outcomes, humans avoid aiming at locations that increase the likelihood of a penalty (Meyer, Abrams, Kornblum, Wright, & Smith, 1988). This spatial avoidance relies on the statistics of both sensory (Whiteley & Sahani, 2008) and motor (Trommershauser et al., 2005) signals in the goal of probabilistically estimating the degree of risk associated with actions made to different areas of space (Nagengast, Braun, & Wolpert, 2011). Specifically, humans account for both penalty magnitude and response variability such that an increase in either will increase their penalty-avoidance bias (Gepshtain, Seydell, & Trommershäuser, 2007; Landy, Goutcher, Trommershäuser, & Mamassian, 2007; Landy, Trommershäuser, Daw, 2012; Trommershäuser et al., 2005; Trommershäuser, Landy, & Maloney, 2006; Trommershäuser et al., 2003a; Trommershäuser, Maloney, & Landy, 2003b; Wu, Trommershäuser, Maloney, & Landy, 2006). This process is largely consistent with statistical decision theory, which describes how probabilistic information is incorporated into

decision processes (Berger, 1985; Maloney & Zhang, 2010) in order to maximize expected gain by minimizing penalty on decisions with uncertain costs. Specifically, the expected gain model of sensorimotor decision-making posits that humans combine probabilistic estimates of spatial targets with estimates of relative reward and penalty associated with those targets to produce a gradient of action value (Trommershäuser et al., 2003a; Trommershäuser, Maloney, & Landy, 2008). Figure 2.1a depicts the expected gain model in an example trial where the peak of the expected gain function is shifted away from a penalty inducing stimulus. One cue represents the target of a spatial action, where selections closer to the mean lead to greater rewards (solid black distribution, Figure 2.1a), while the other represents the spatial location of a region where selections will incur a penalty (gray distribution, Figure 2.1a). The expected gain model predicts that the magnitude of selection bias away from the penalty region is estimated as a cost function across space ( $x$ ) (black dashed line, Figure 2.1a), reflecting the difference between these two distributions (Gepshtein et al., 2007; Landy et al., 2007, 2012; Neyedli & Welsh, 2013; Trommershäuser et al., 2006, 2003a, 2003b; Wu et al., 2006).

$$MEG_x = \arg \max_x (\alpha N(x; \mu_T, \sigma_T) - (1 - \alpha)(N(x; \mu_{NT}, \sigma_{NT})) \quad \text{Eq. 2.1}$$

In *Equation 2.1*, the optimal location to reach towards, i.e., the location with the maximum expected gain ( $MEG_x$ ), is the maximum of a linear function that represents the difference of the target (denoted with subscript  $T$ ) and non-target (denoted with subscript  $NT$ ) distributions, each with a mean (i.e., centroid) and standard deviation of  $\mu_T$  and  $\sigma_T$ , and  $\mu_{NT}$  and  $\sigma_{NT}$ , respectively. Thus, selection behavior is reflected as a distribution of endpoints over a series of

reaches with a mean centered over the target mean. The value of  $\alpha$  ranges from zero to one and determines the weight of the difference between target and non-target distributions in the resulting response ( $MEG_x$ ). When  $\alpha = 1$ , the penalty-inducing non-target is ignored, and the selections will focus at the mean of the target. As  $\alpha$  decreases, the location of the non-target induces a greater avoidance bias, pushing the selection away from the mean of the target. Figure 2.1b depicts selection bias away from the non-target (downward on the y-axis) in arbitrary units as a function of  $\alpha$  (x-axis) at different ratios of target to non-target variance based on *Equation 2.1*. If the target and non-target reflect the spatial location of reward and penalty, respectively, then at smaller values of  $\alpha$ , selection bias manifests as a shift in the selection distribution away from the penalizing non-target (and towards a location in the target that is still likely to result in reward).

By design, the expected gain model predicts that changes in stimulus variance should influence estimates of the  $MEG_x$  location. This is also illustrated in Figure 2.1b, where the topmost curve shows the predictions of the expected gain model (*Equation 2.1*) across all values of  $\alpha$  when the variances of the target and non-target are equal. Here bias is shown as more negative values that reflect stronger avoidance away from non-target mean. The other curves show cases where the variance of the target is 175%, 250%, 325%, and 400% larger than the variance of the non-target. Note that bias increases as the ratio of target to non-target variance increases, as well as with lower values of  $\alpha$ .

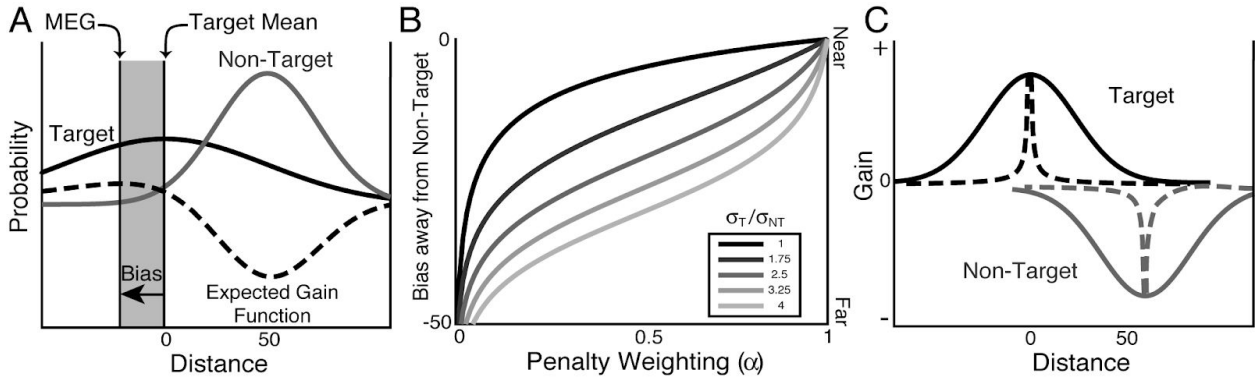


**Figure 2.1** Illustration of the expected gain function, predicted selection bias and scoring functions. (A) The target (solid black line) and penalty-inducing non-target (solid gray line) stimuli are represented as Gaussian distributions with means separated by a fixed distance of 50 arbitrary units. The expected gain function (dashed black line) is approximated as a linear combination of the stimulus distributions, weighted by their relative outcomes (i.e.  $\alpha$  and  $1-\alpha$ ). On estimation trials (see *Methods: Experimental task*), the mean of the target must be selected to receive the highest points possible. Selecting the peak of the non-target minimizes points during penalty blocks. The peak of the expected gain function (MEG) represents the optimal perceptual position to select based on the statistics of the stimulus distributions. The gray area between the MEG and target mean demarcates where selections are biased away from the non-target across trials. (B) Selection bias away from the non-target is plotted as a function of penalty weighting ( $\alpha$ ) across different ratios of target to non-target variance from 1:1 (black curve) to 4:1 (lightest gray curve). More negative y-axis values reflect larger selection bias. (C) Dashed black and gray lines represent hyperbolic scoring functions (see *Equation 2.4*) for the stimulus distributions. Point gain on a selection increases along the y-axis for the target but is negative for the non-target.

Previous studies on risky spatial decisions used filled-in circles with clear boundaries to represent the target and non-target regions of the space (Meyer et al., 1988; Trommershäuser et al., 2008). This design introduces two limitations that we address in the current study. First, these previous efforts did not systematically manipulate the effects of stimulus variance and, therefore, sensory uncertainty on spatial decisions, since the target and non-target areas were readily visible to the participants. Put another way, these previous studies were not designed to study the spatial

estimation and selection process. Here, we adapted a probabilistic stimulus design wherein the target and non-target positions must be estimated as the respective means of two sparse Gaussian distributions of dots (Acuna, Berniker, Fernandes, & Kording, 2015; Bejjanki, Knill, & Aslin, 2016; Juni, Gureckis, & Maloney, 2015; Tassinari, Hudson, & Landy, 2006). The second limitation involves the feedback payoff structures, in which the reward and penalty values were uniform throughout target and non-target regions of the stimulus. This structure necessarily results in an optimal selection location that is always biased away from the target center and the non-target in penalty conditions (Meyer et al., 1988; Neyedli & Welsh, 2013; Trommershäuser et al., 2003a, 2003b; Wu et al., 2006). Thus, there was not a true optimal location based on both the sensory and feedback signals as expected by the expected gain model (*Equation 2.1*), but instead a range of regions, which could be estimated purely from spatial signals, that produced the same reward. Here we disambiguated the spatial distribution of the feedback signal from the spatial distribution of the visual stimulus in order to increase attention at estimating the true mean of the target. Finally, previous studies have relied on ballistic reaches to represent their spatial selections, which can increase urgency in the action, thereby increasing selection noise. To mitigate the influence of motor noise, we allowed participants an unlimited amount of time to respond. Together, these experimental modifications allowed us to extend past research on risky spatial decisions by better controlling variability in motor behavior.

Using this paradigm, we sought to address previously untested predictions about the effects of stimulus variance on selection behavior during risky spatial decisions. First, based on the expected gain model (*Equation 2.1* and Figure 2.1b), we hypothesized that increasing the ratio of target ( $\sigma_T$ ) to non-target ( $\sigma_{NT}$ ) spatial variance should increase selection bias away

from the non-target. In other words, when the target mean is harder to estimate, relative to the location of the non-target, participants should be more cautious in their spatial estimations and be more biased away from the non-target stimulus. Second, this effect on spatial variance on avoidance bias should interact with explicit costs (i.e., target and non-target weights,  $\alpha$  and  $1-\alpha$ ) to more strongly bias selections than penalty conditions alone. Finally, as demands of integrating spatial signals increases (i.e., target variance increases) and estimating relative value increases (i.e.,  $\alpha$  gets smaller), then this should increase computational demands on the decision and slow reaction times to initiate the selection. With our paradigm, we were also able to observe the influence of sensory variance on reaction times that were largely unexplored in previous work.

## 2.2 Methods

### 2.2.1 Participants

Thirty undergraduate students enrolled in an introductory psychology course at Carnegie Mellon University were recruited through the university's Psychology Research Experiment System. Ten participants failed to perform at or above a criterion of 50% overall accuracy on the catch trials (see Section 2.2.3 Experimental task), leaving a final sample of 20 participants (9 females, 11 males). Participant ages ranged from 18 and 23 years of age (mean age = 20.4) and were screened for normal or corrected-to-normal vision and right-handedness. Each eligible participant reviewed and signed a consent form approved by the Carnegie Mellon University Institutional Review Board. All participants who completed the study received credit toward fulfillment of their semester course requirements.

### 2.2.2 Experimental setup

The experiment was conducted using Psychophysics Toolbox 3.0.10 (Brainard, 1997; Kleiner et al., 2007) through MATLAB (Release 2012a, The MathWorks, Inc., Natick, MA, United States) on a desktop computer running Ubuntu 14.04. Participants completed the task seated in a dimly lit room in front of a 23" computer monitor with a total screen resolution of 1920 x 1080 pixels.

### 2.2.3 Experimental task

Using a 2x2 (low vs. high target variance x no-penalty vs. penalty) within-subject design, each participant completed eight blocks of trials (two blocks per condition). The order of block conditions was randomized for each participant. A total of 102 trials (82 estimation trials and 20 catch trials) were presented in each block with a total of 816 trials (656 estimation trials and 160 catch trials) across the entire experiment. The experiment took approximately 45 minutes to complete.

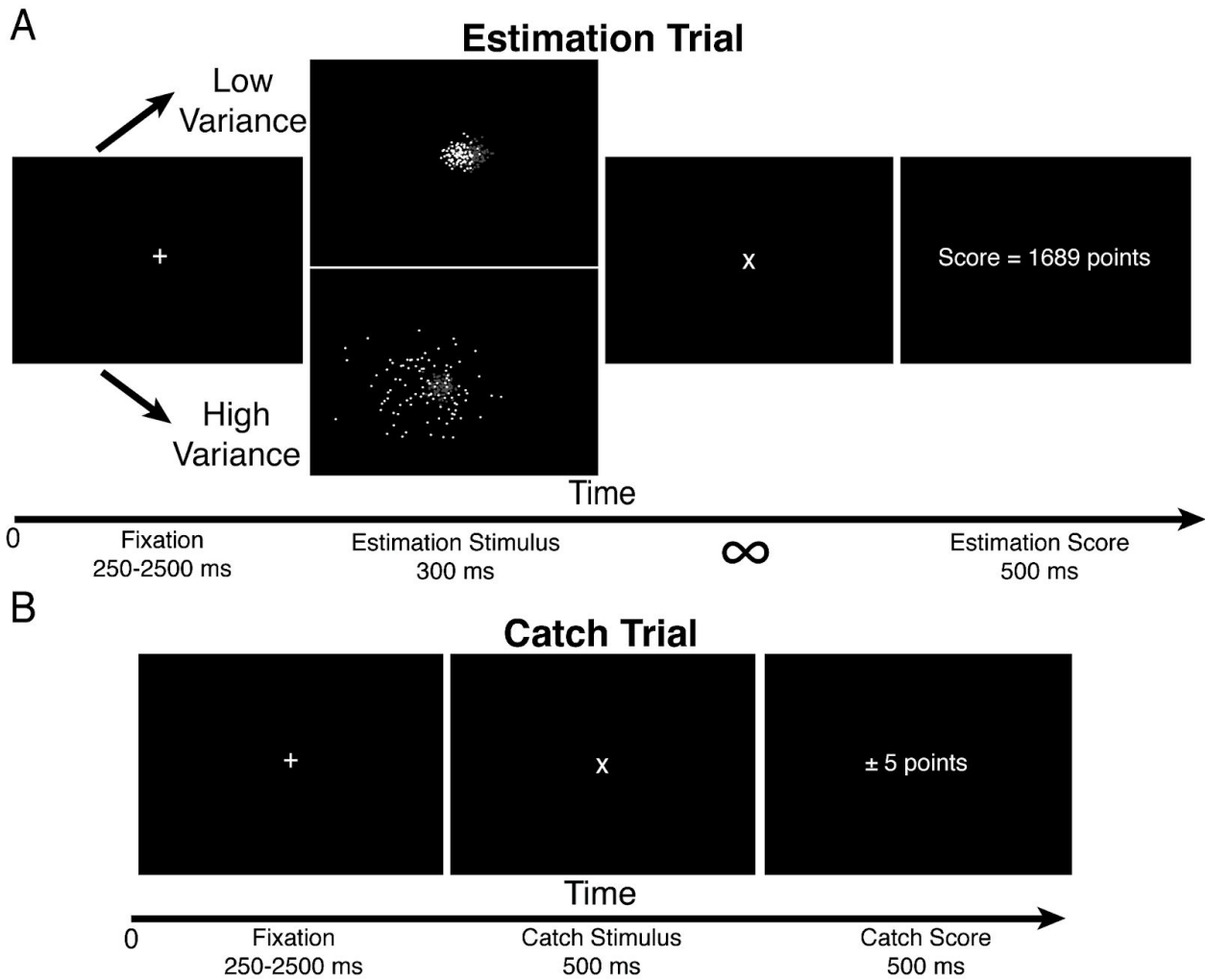


**Figure 2.2** Experimental trial timeline. Participants clicked and held the left mouse button to initiate all trials. (A) On estimation trials, a fixation (+) was presented (250-2500 ms jittered). The target (referred to as the Target in the task; white) and non-target (referred to as the Danger Zone in the task; gray here, presented in red in the task) stimuli flashed on screen for 300 ms then disappeared. Participants then had unlimited time to indicate their target selection by dragging the cursor (x) and releasing the mouse button. Score on a trial, based on selection distance from the target, was presented for 500 ms. (B) On catch trials, instead of visual cues, an “x” was presented after a random interval. Participants obtained a flat point total for releasing the mouse within 500 ms, or lost points for missed catch trials or responses slower than 500 ms.

All trials were self-paced, and participants initiated each trial by clicking and holding the

left mouse button while the screen was blank. A fixation stimulus (+) appeared at the center of the screen following the click and hold. On estimation trials (Figure 2.2a), after a uniformly sampled period of time between 250-2500 ms, the target and non-target stimuli were presented simultaneously on the screen for 300 ms before disappearing. Both the target and non-target distributions appeared completely in randomly sampled locations within the rectangular space of 1024 x 768 pixels centered on the screen, with the constraint that both stimuli were completely visible in the workspace. The target stimulus (Target) was presented as a Gaussian distribution of 100 white dots, each 3 pixels in diameter. The non-target stimulus, referred to as the “Danger Zone” on penalty trials (described below), was simultaneously presented as a Gaussian distribution of 100 red dots (gray in Figure 2.2a), also with 3-pixel diameters. This distribution could appear either to the right or left of the Target with equal probability on each estimation trial. The horizontal distance between the mean of the target and mean of the non-target was fixed at 50 pixels. The standard deviation of the Target was 25 pixels in the low variance blocks and 100 pixels in the high variance blocks. The non-target always had a standard deviation of 25 pixels.

Once the two stimuli were removed from the screen, the mouse cursor was presented as an “x” at the center of the screen. Participants had an unlimited amount of time to drag the cursor to a location and then release the left mouse button to indicate their selection of the mean of the target stimulus. Immediately following the selection, a point total for that trial was presented at the center of the screen for 500 ms. The screen then went blank until the participant initiated the next trial.

On half of the blocks, the reward feedback would be penalized based on the proximity of

the participant's selection to the non-target ("Danger Zone"), while this penalty was not applied on the remaining blocks. Participants were cued to the cost condition (i.e., no-penalty or penalty) of the upcoming block of trials by onscreen instructions. The block commenced after the participant indicated they were ready to begin by pressing the spacebar on the keyboard. Regardless of cost condition, selecting the mean of the target stimulus guaranteed the maximum number of points that could be scored on an estimation trial. Points scored on each estimation trial were computed based on the distance of a selection from the target and non-target means. On each trial, the Euclidean distance to the target stimulus (*Equation 2.2*) and non-target stimulus (*Equation 2.3*) were computed based off of the selection location  $(x_s, y_s)$  and the means of both the target stimulus  $(x_T, y_T)$  and non-target  $(x_{NT}, y_{NT})$  distributions, respectively.

$$d_T = \sqrt{\sum ((x_s, y_s) - (x_T, y_T))^2} \quad \text{Eq. 2.2}$$

$$d_{NT} = \sqrt{\sum ((x_s, y_s) - (x_{NT}, y_{NT}))^2} \quad \text{Eq. 2.3}$$

The reward feedback score on each trial was computed as the weighted difference between the target ( $d_T$ ) and non-target ( $d_{NT}$ ) selection errors, such that

$$\text{Score} = \omega (100/d_T) - (1 - \omega) (100/d_{NT}) \quad \text{Eq. 2.4}$$

In *Equation 2.4*, the feedback score based on selection position was computed to have a hyperbolic  $1/d$  falloff where  $d$  equaled the distance between a selection location and mean of the target. Here the scoring functions are weighted by  $\omega$ , corresponding to the weight of the spatial distributions specified by the value of  $\alpha$  in *Equation 2.1*. In no-penalty blocks, the value of  $\omega$  was set to 1, so that only selection distance from the target contributed to the score on those trials. In penalty blocks,  $\omega$  was set to 0.33 so that participants incurred a heftier loss for selections that were closer to the center of the non-target.

The dashed lines in Figure 2.1c provides a visual representation of the hyperbolic scoring functions overlaid with Gaussian target and non-target distributions. The highest possible score on any estimation trial was constrained to 200 if a perfect distance was estimated (i.e.,  $d_T = 0$ ). To more strongly engage participants in the task, scores were multiplied by 1000 when presented at the end of each trial. The use of the hyperbolic function meant that any spatial error between the selection and target resulted in a steep reduction in points, thereby forcing participants to aim as closely to the mean of the target stimulus as possible. The fixed distance between the target and non-target locations ensured that target selections yielded the greatest number of points on an estimation trial across all blocks, regardless of cost condition.

Twenty catch trials (Figure 2.2b) were randomly presented throughout each block as an experimental control to verify that participants were fixating on the center of the screen at the start of each trial. Just like the estimation trials, participants initiated catch trials from a blank screen by clicking and holding the left mouse button. A fixation appeared at the center of the screen for a jittered period of 250-2500 ms after trial initiation. Then, in lieu of the appearance of the estimation trial stimulus, the fixation changed from a “+” to an “x” at the center of the screen.

Participants then had to release the mouse button within 500 ms in order to gain five points, or otherwise lose five points for either failing to respond or responding too slowly.

Data from 10 participants were excluded from further analyses for failure to reach 50% accuracy on the catch trials across the entire experiment. One possible explanation is that the magnitude of points on estimation trials dwarfed that on catch trials, reducing the incentive to respond. Estimation trials were also far more frequent in the task (80% of all trials) and had no limit for responses, whereas catch trial responses had to be made within 500 ms. However, we note that the general pattern of results, including the statistical significance and effect sizes of our reported results, do not change with inclusion of those data. As such, we do not include any further discussion of catch trial performance.

#### 2.2.4 Data analysis

Selection variability, bias, and reaction time were the primary dependent measures. The spatial location of a selection as well as the time between offset of the stimuli and movement onset on estimation trials (i.e., reaction time) was recorded for every trial across all participants. For all analyses, only the position along the x-dimension, i.e., the selection, was used since this was the dimension along which the adjacent non-target location was manipulated. Selection variability, bias, and reaction time were computed for all 164 estimation trials within the same experimental condition. Selection variability was computed as the standard deviation of the x-coordinate of selections across trials within a condition.

Selection bias was computed as the difference between the selection and target on a trial relative to the position of the non-target stimulus, which could be presented either to the left or

right of the target stimulus. As illustrated in Figure 2.1b, the selection bias score has more negative values with a greater selection distance away from the non-target stimulus, relative to the mean of the target stimulus. Positive values would indicate selections closer to the non-target stimulus.

A two-way repeated measures ANOVA was conducted to observe the main effects of variance and penalty (i.e., cost) conditions, as well as the variance x penalty interaction separately on selection variability, bias, and reaction time (Figure 2.3). Paired sample t-tests were used as post-hoc measures to determine the directionality of main effects and interactions in significant omnibus tests. Effect sizes were estimated as partial eta squared,  $\eta_p^2$ .

### 2.3 Results

As predicted, variability of participants' estimates of the target stimulus mean were higher in the high variance blocks than the low variance blocks,  $F(1,19) = 7.29, p = 0.014, \eta_p^2 = 0.28$  (Figure 2.3a). We averaged the scaling effect of variance across the penalty and no penalty blocks and computed the ratio of selection variability in high variance blocks to low variance blocks to be 1.59. This scaling effect for variance There was no main effect of penalty condition on selection variability,  $F(1,19) = 0.83, p = 0.37$ , nor was there a variance x penalty interaction,  $F(1,19) = 1.41, p = 0.25$ . This indicates that increasing the spatial variance of the target stimulus reduces the reliability of the spatial estimations. Indeed, we did observe a significant main effect of target variance on reaction time,  $F(1,19) = 37.80, p < 0.001, \eta_p^2 = 0.67$  (Figure 2.3b), wherein reaction times slowed in the high variance conditions. Though penalty did not have a significant main effect on reaction times,  $F(1,19) = 2.55, p = 0.13$ , there was a significant variance x penalty

interaction,  $F(1,19) = 5.62, p = 0.029, \eta_p^2 = 0.23$ . The paired t-test confirmed that the high variance condition with penalty resulted in significantly slower reaction times than the high variance condition with no penalty, paired  $t(19) = -2.38, p = 0.014$ , Cohen's  $d = -0.53$ . Reaction times were not significantly different between low variance blocks, paired  $t(19) = 1.68, p = 0.1098$ , regardless of penalty condition. This effect on reaction times is interesting as past work motivating the current experiments implemented a time constraint with very short time durations (e.g., < 700 ms), which is often critical for detecting changes in reaction times due to influences on the decision process itself. However, reliable effects of spatial stimulus variance and penalty on reaction times were not observed (Neyedli & Welsh, 2013, 2014; Trommershäuser et al., 2003a, 2003b). We elaborate on this difference between studies further in the Discussion. Taken together, the selection variance and reaction time results confirm that the target spatial variance manipulation impacted the reliability of the spatial estimation process.

The expected gain model predicts that selection bias away from the non-target stimulus should increase in these conditions of low sensory certainty, and this effect should interact with the presence of feedback penalties. Consistent with previous observations (Neyedli & Welsh, 2013, 2014; Trommershäuser et al., 2005; Trommershäuser et al., 2003a, 2003b), the introduction of a penalizing cost on selections resulted in a bias away from the non-target (Figure 2.3c). The ratio of bias in penalty blocks compared to no penalty blocks was 2.47 when we averaged the scaling effect of penalty across low and high variance conditions. Both main effects of variance,  $F(1,19) = 7.72, p = 0.012, \eta_p^2 = 0.29$ , and penalty condition,  $F(1,19) = 18.66, p < 0.001, \eta_p^2 = 0.50$ , as well as the variance x penalty interaction,  $F(1,19) = 10.63, p = 0.004, \eta_p^2 = 0.36$ , were significant. Generally, selection bias was greater in high variance conditions;

one-sample t-tests, evaluating the bias effect with respect to a null hypothesis of zero, revealed this nonzero bias was present in penalty blocks across the low,  $mean = -2.84$ ,  $t(19) = -2.90$ ,  $p = 0.009$ , Cohen's  $d = -0.65$ , and high variance,  $mean = -15.64$ ,  $t(19) = -3.72$ ,  $p = 0.002$ , Cohen's  $d = -0.83$ , conditions. A paired t-test showed that the magnitude of this penalty-induced bias was significantly greater in high variance blocks, paired  $t(19) = -3.23$ ,  $p = 0.005$ , Cohen's  $d = -0.72$ . This confirms our prediction that when the sensory reliability of spatial target estimates is low (i.e., high spatial variance), selection bias away from the non-target increases.

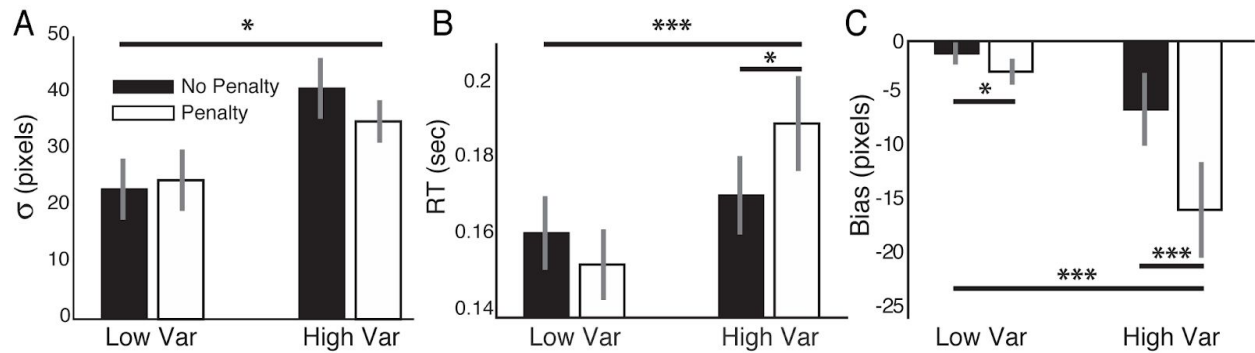


**Figure 2.3** Selection variability, reaction time, and bias across conditions. Bar color is same in all panels and error bars represent the standard error of the mean. (A) Average selection variability in pixels, measured as the standard deviation ( $\sigma$ ) of selections in low and high variance blocks, were compared across no-penalty (black) and penalty (white) blocks. There was a significant main effect of target variance that resulted in increased selection variability in high variance blocks. (B) Average reaction time (RT) in seconds, measured as the amount of time from stimulus offset and the initiation of movement on an estimation trial. There was a significant interaction between variance and penalty. RTs were slower in high variance conditions with the longest RTs in the high variance x penalty blocks. (C) Average selection bias in pixels, measured as the distance of selections from the target mean. A significant interaction between variance and penalty resulted in the greatest bias away from the non-target (Danger Zone) in the high variance x penalty blocks. Both main effects were significant and showed an increased bias in penalty blocks. Asterisks and hash lines denote significant main effects and interactions (\*  $p < 0.05$ , \*\*\*  $p < 0.05$ ).

## 2.4 Discussion

Consistent with the predictions of the expected gain model (Trommershäuser et al., 2003a, 2008), we show that sensory reliability of visual targets interacts with spatial cost estimates during goal directed action. We confirmed that increasing the spatial variance of a visual target reduces the reliability of spatial estimates of the target mean (Bejjanki et al., 2016; Kording & Wolpert, 2004; Tassinari et al., 2006). By allowing an unlimited amount of time to make selections, our task was less sensitive to the effects of motor noise on spatial estimates than previous studies that used a ballistic reaching paradigm (Neyedli & Welsh, 2013, 2014; Trommershäuser et al., 2003a, 2003b). Because our paradigm did not pressure response speed itself, other non-planning processes could contribute to variability in the reaction times (Wong, Goldsmith, Forrence, Haith, & Krakauer, 2017), tempering the interpretation of context influences on response speed. We also replicated the observation that participants biased their selections away from a non-target stimulus that could induce a penalty on feedback scores (Landy et al., 2007, 2012; Trommershauser et al., 2005; Trommershäuser et al., 2003a, 2003b; Wu et al., 2006). Critically, we showed for the first time, under conditions of high target variance and penalty, participants most strongly biased selections away from the non-target stimulus and also took significantly more time to initiate selection movements.

Though our findings are generally consistent with probabilistic models of human spatial estimation (Landy et al., 2007; Neyedli & Welsh, 2013; Tassinari et al., 2006; Trommershäuser et al., 2003a, 2003b), we built on past research by providing support for previously unexamined predictions of the expected gain model (Trommershäuser et al., 2003a, 2008) regarding the effect of stimulus variance on spatial decisions. First, we confirmed the prediction that increasing the

ratio of target to non-target stimulus variance increases avoidance bias away from the non-target stimulus (Figure 2.1a and b, and 2.3c). While this prediction comes out of the normative form of the expected gain model (see *Equation 2.1*), it was not evaluated in previous studies because the stimuli used did not allow for the manipulation of spatial certainty. Our novel implementation of 2D Gaussian distributions as target and non-target stimuli, rather than circles, allowed for systematically manipulating the spatial precision of sensory signals and, consequently, the variance of the estimation process itself. Second, we found an interaction between stimulus reliability and penalty-induced avoidance bias, the greatest selection bias was away from the penalizing non-target in high target variance conditions. Again, this follows from the prediction of the normative form of the expected gain model (see Figure 2.1b). Finally, by dissociating the feedback function from perceptual distributions of the target (Figure 2.1c), we were able to show that the avoidance bias reflects a purely perceptual estimation process, rather than a feedback learning process. Specifically, had participants been using just the trial-by-trial reward feedback signals to find the optimal selection location, the mean of their selections would center on the mean of the target stimulus (i.e., zero spatial bias). The fact that participants still showed a bias in non-penalty conditions and that this bias scaled with perceptual reliability of the spatial location of the target, confirms that trial-by-trial reinforcement learning has little impact on the estimation process itself (Trommershäuser et al., 2003a, 2003b). We should point out, however, that Neyedli & Welsh (2013) found evidence that reward feedback signals may moderate the shape of this bias over time. While we failed to see evidence of such learning in our participants (analysis not shown), this is likely due the fact that our experiment was not designed to explicitly test for learning effects.

It is worth noting that the avoidant selection behavior shown here likely reflects a top-down strategy rather than a simple computation on bottom-up sensory inputs. Past risky spatial decision-making studies manipulated the degree of target and non-target circle overlap (Meyer et al., 1988; Neyedli & Welsh, 2013; Trommershäuser et al., 2003a, 2003b), thereby constraining the spatial region that would produce a reward. From a statistical perspective, there are two ways to compensate behavior when the rewarded spatial region shrinks: improve spatial precision by reducing selection variability or improve accuracy by shifting the mean of the selection to being near the center of this constrained reward region. As in the current study, these previous experiments showed that rather than constraining motor output variability based on sensory estimates to ensure that selections fell within the available space of the target, participants shifted the mean of their selections away from the penalizing non-target to a degree that corresponded to target and non-target overlap in order to avoid losses. In some ways, this is consistent with the principle of loss aversion in Prospect Theory, which posits that “losses loom larger than gains” in that individuals are more sensitive to a potential loss than a sure gain of equal or greater expected value (Tversky & Kahneman, 1992). However, it is worth noting that our experimental design was able to dissociate the actual optimal feedback position with the expected optimal position given a weighted combination of the two stimuli (see Figure 2.1c). If participants were simply using a mixture of the incoming sensory signals and previous reward feedback to learn an optimal location to select, they would always select the mean of the target stimulus. The fact that we also observed a strong avoidance bias suggests that the maximum expected gain estimation is a purely perceptually driven spatial estimate and not an optimal decision given the reward feedback delivered.

Although selection bias was not significantly different from zero on low target variance blocks with no penalty, selections still trended away from the non-target, rather than varied symmetrically about the target (i.e., zero bias). While participants may have been primed to always avoid the non-target stimulus across the experiment, this nonzero bias on no-penalty blocks when  $\alpha$  was fixed at a value of 1 suggests that participants did not fully discount the non-target even though it should have had no influence on their spatial estimates. Our experimental design was limited in determining whether this observation was due to some carryover of  $\alpha$  values when no-penalty blocks followed penalty blocks, or whether there is some other source of noise in the spatial estimation process that should be considered in the expected gain model. Indeed, there is evidence that both learning of expected costs on spatial decision outcomes (Neyedli & Welsh, 2013, 2014) and noisy spatial estimates (Juni et al., 2015) can lead to biased selection behavior. Future paradigms can use a counterbalanced block structure and manipulate  $\alpha$  parametrically to quantitatively assess any potential effects of carryover (e.g., learned value of  $\alpha$ ) or noisy spatial estimates.

We also found that increased sensory stimulus variance interacts with penalty to further slow the time it took to initiate the selection decision. Under conditions of high target variance, participants took significantly longer to initiate their movements with the slowest reaction times occurring in high variance blocks with penalty. When penalty was added along with high demands on selection precision, i.e., high sensory variance, participants might have taken longer to respond as a precaution in order to mitigate larger than expected costs. This cautionary behavior may reflect some subjective difficulty or uncertainty either in a strategic plan to reduce known costs or in the implicit spatial estimation process itself. This presents another avenue of

research wherein expected cost, reflected by trial-by-trial fluctuations in the value of  $\alpha$ , and estimates of stimulus variance can be considered together during spatial decisions. As such, new models of sensorimotor integration can relate explicit (e.g., costs) and implicit (e.g., sensory variance) aspects of estimation processes that underlie spatial decision behavior (McDougle, Ivry, & Taylor, 2016; Summerfield & Tsetsos, 2012; Taylor, Krakauer, & Ivry, 2014).

## 2.5 Conclusion

Taken together, our findings clearly show that estimates of sensory variance contribute to the degree to which individuals attempt to avoid penalties during risky spatial decisions by biasing their action selections away from regions that induce feedback penalties. Based on our results, it largely appears that estimates of stimulus variance and cost conditions along with expected feedback are considered together while people make spatial judgments in an attempt to maximize gain. However, the proposition that “losses loom larger than gains” (Tversky & Kahneman, 1992) implies that there is a subjective component to avoiding penalty during spatial decisions. This further suggests that subjective differences in the kinds of penalty incurred can influence how much people bias their selection behavior. If an individual has to make a risky decision between two different kinds of losses, e.g., points versus real money, then they may show an increased selection bias to avoid a penalty that they perceive as more costly. In the following chapter, I present the findings from an experiment that uses a modified version of the Danger Zone paradigm to explore how the contextual framing of losses impacts risky spatial decision behavior.

# **Chapter 3**

## **Contextual framing of a risky spatial decision outcome impacts loss avoidance**

In Chapter 2, we showed that increased sensory uncertainty and expected penalty drives increased loss avoidance during risky spatial decisions. Here we present a second novel study, Drone Strike, that leverages the experimental control of risk and uncertainty in Danger Zone to examine how contextual framing (i.e., a harmful versus helpful action) influences the extent to which people avoid loss during risky spatial decisions. The primary difference between Drone Strike and Danger Zone is the addition of a wartime narrative to manipulate the contextual framing of loss between penalty and no-penalty conditions, thus inducing top-down engagement in the decision-making process that was not necessary for Danger Zone. Otherwise, the visuospatial features and score distributions constituting the target and non-target stimuli were identical between the studies.

### **3.1 Introduction**

Imagine that you are challenged to throw a dart and strike the center, or bullseye, of a dartboard. How would your aim and throwing behavior change if your challenger replaced the bullseye with a picture of a close friend, or worst enemy? Now, this task is imbued with a contextual meaning even though throwing the dart with the goal of striking the bullseye remains the same. Here, we

ask how contextual framing influences behavior during spatial decision-making. To begin exploring this question, we introduce an extension of the Danger Zone paradigm (Chapter 2) in which narrative frames are used to contextualize risky spatial decision-making scenarios to determine whether or not selection bias is impacted by differences in the kind of loss incurred when all other aspects of the task are identical.

Interestingly, in the Danger Zone study, despite participants being explicitly informed that selecting the center of the target distribution maximized expected gain, regardless of task condition, we still observed significantly greater loss avoidance during the penalty conditions. Even though participants showed that they were capable of selecting the center of the target in conditions without penalty, the findings suggest that participants incorporated both information about risk via point-based feedback on selections and estimates of sensory uncertainty when making selection decisions. Doing so resulted in a selection bias that mitigated penalty particularly when the spatial decision was framed in terms of a potential loss. This further suggests that instead of objectively selecting the center of the target on all trials, people may have been incorporating a *subjective* valuation of feedback and sensory uncertainty that was reflected in a selection bias away from the penalizing non-target. This subjective aversion to potential loss offers an explanation for why participants failed to select the location that was guaranteed to maximize expected gain under penalty conditions in spite of demonstrating a clear ability to do so in no-penalty conditions when all visuospatial aspects of the decision were equivalent.

### 3.1.1 Contextual framing effects on risky decisions

Framing an otherwise equivalent economic decision as two different kinds of losses has been shown to have distinct effects on choice behavior. For instance, people are more likely to accept a gamble with a high probability of losing some amount of money rather than spending the same amount of money to enter a lottery with the same high probability of losing (i.e., winning nothing) (Kahneman & Tversky, 1979, 1984) (Hershey & Paul J. H. Schoemaker, 1980; Tversky & Kahneman, 1981; Wang, 1996; Yang, Vosgerau, & Loewenstein, 2013). Given that the likelihood and monetary value of a losing outcome is the same in both cases, choosing a gamble over a lottery is based only on a person's subjective preference for how, but not how much, they might lose on their decision. In particular, the contextual framing of the decisions impacts whether or not an individual chooses an option that is more likely to maximize expected gain because of a subjective preference to avoid one kind of loss over another.

### 3.1.2 Framing impacts moral judgments of decision outcomes

Experimental philosophy research, motivated by moral psychology, has shown that the contextual framing of the moral valence (e.g., the *goodness* or *badness*) of a decision outcome impacts an individual's judgment of the decision. Consider the phenomenon known as the Knobe effect, or the 'side-effect' effect, wherein people show striking differences in judging how intentional another individual's decision was based on the framing of its outcome (Feltz, 2007; Knobe, 2003a, 2003b). Knobe (2003) showed that simply changing the word "harm" to "help" in vignettes that described the indirect outcome, i.e., side-effect, of an action decision was enough to change how people judged the intentionality of another individual's decision (Knobe, 2003a).

On two separate experiments, when participants read that the side-effect was harmful, or morally “bad”, 77% and 82% of the participants judged the decision as intentional. For vignettes in which the side-effect was helpful, or morally “good”, 77% and 70% judged the decision as unintentional. Importantly, the side-effect of the decisions presented in either set of vignettes were exactly the same regardless of context, so participants had no reason to judge the decisions differently other than the description of side-effects as “good” or “bad”. These experiments suggest that the contextual framing of decision outcome can be a powerful experimental manipulation that influences how people interpret and characterize information about action decisions. Furthermore, we can examine whether the perception of decision-related information as being either potentially harmful or helpful differentially influences a person’s decision-making processes as reflected by their own decision-making behavior.

### 3.1.3 Contextual framing and the maximum expected gain model

In the Drone Strike task presented in this chapter, we used a wartime scenario to develop two kinds of moral dilemmas that provided a contextual frame for the same type of risky spatial decisions in the Danger Zone experiment (Chapter 2). Namely, the target represented enemies to be neutralized on a drone strike or allies to whom ammunition needed to be delivered. In penalty conditions, the non-target represented either nearby allies to be avoided by a drone strike (harm context) or enemies to be avoided on ammunition deliveries (help context). Here the harm context contextualizes losses (i.e., ally casualties) as being subjectively more aversive than in the help context (i.e., ammunition intercepted by enemies). Importantly, the nature of the sensory

signals is identical between the help and harm conditions. The only thing that changes is the context in which the spatial decision is made.

Returning to the maximum expected gain model presented in Chapter 2, the term  $\alpha$  is used to weigh the target and non-target distributions, which partly determined the magnitude of selection bias away from the penalizing non-target (see *Equation 2.1*). The effect of contextual framing on risky spatial decisions can be examined within the framework of the maximum expected gain model by scaling  $\alpha$ . Figure 3.1 illustrates selection bias as a function of  $\alpha$  during a risky spatial decision under two contextual frames for loss. In particular, we assume that loss during the harm condition is subjectively more aversive than the help condition and should result in a greater selection bias away from the penalizing non-target (i.e.,  $\alpha_{Harm} < \alpha_{Help}$ ), when all other aspects of the decision (e.g., sensory signals, timing) are the same.

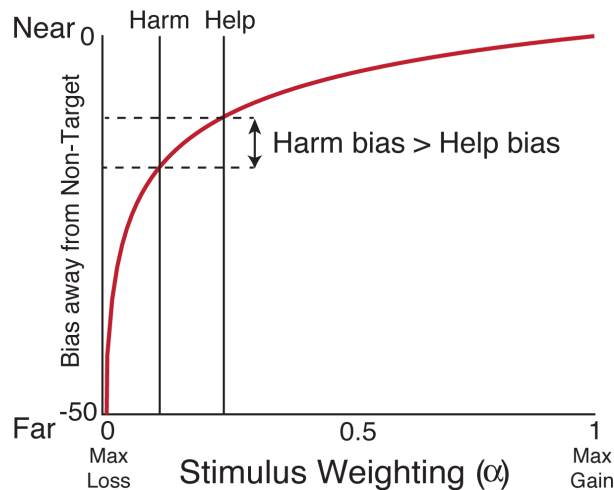


**Figure 3.1** Illustration of selection bias difference prediction based on the maximum expected gain model. Selection bias is plotted as a function (solid red line) of penalty weighting ( $\alpha$ ) and a 1:1 target to non-target variance ratio ( $\sigma_T/\sigma_{NT}$ ). More negative values on the y-axis represent selections farther away from the non-target region of the stimulus. Horizontal black dashed lines reflect the hypothesized difference in selection

bias in harm and help contexts (solid black lines), where bias is expected to be farther away from a penalizing non-target in subjectively more aversive harm conditions.

Here we specifically address the hypothesis that if risky spatial decision-making behavior is impacted by the subjective aversion to potential loss, then selection bias away from the penalizing non-target in the context of harm (i.e., ally casualties) will be significantly greater than in the help context (i.e., ammunition interception by enemies). Additionally, we present the findings from analyses on the effects of context (harm versus help), cost (no-penalty versus penalty), and target variance (low versus high) on other measures of performance, including selection precision, reaction time, movement time, maximum movement velocity, and average movement velocity. Together, these results more fully characterize avoidant selection behavior during risky spatial decisions.

## 3.2 Methods

### 3.2.1 Participants

Based on the Danger Zone study (Chapter 2), which had a 2x2 within-subjects design and a final sample size of 20 participants, here we recruited a total of 50 participants, which ensured that we had twice the sample size given that this present study has twice the number of experimental conditions. Since the added conditions required more time for extra instructions before task blocks, two sessions were needed in order for participants to a similar number of trials between studies: Drone Strike = 640 trials (320 trials/session), Danger Zone = 656 “estimation” trials, see Chapter 2. A total N = 44 healthy adults (mean age = 22.6 years, age range = 18 - 44; 33 female, 11 male) completed two, one-hour behavioral sessions that occurred on consecutive days. One

participant's data was excluded from analysis when an error in stimulus presentation was observed during their second session. Three participants did not return for a second session due to scheduling conflicts that did not allow them to complete the study on consecutive days. Data from two participants were excluded from analyses for failure to reach 90% trial completion on either or both behavioral sessions. Excluding these data did not change the general pattern of results or my interpretation, so we will not discuss them here.

All participants were screened for normal or corrected-to-normal vision and right-handedness. The participant pool consisted of undergraduate and graduate students from Carnegie Mellon University and the University of Pittsburgh. Carnegie Mellon students were notified of the study either via the university's Psychology Research Experiment System or flyers posted on campus. University of Pittsburgh students were recruited via flyers. Participants were recruited based on their completion of a separate survey study that was administered at least two weeks prior to being notified of the present behavioral study. All participants in the behavioral study reviewed with an experimenter and signed a paper consent form approved by the Institutional Review Boards of Carnegie Mellon University and the University of Pittsburgh. All behavioral participants were compensated \$10 per hour for a total of \$10 if only one session was completed, or \$20 upon completion of the both sessions.

### 3.2.2 Experimental Setup and Design

The behavioral experiment was conducted with Psychophysics Toolbox 3.0.12 (Brainard, 1997; Kleiner et al., 2007) through MATLAB (Release 2015a, The MathWorks, Inc., Natick, MA, United States) on a desktop computer running Ubuntu 16.04. Participants completed the task

seated in a dimly lit room in front of a 23" computer monitor with a total screen resolution of 1920 x 1080 pixels and a 60 Hz screen refresh rate.

Using a 2x2x2 (harm vs. help context x no-penalty vs. penalty x low vs. high target variance) within-subject design, each participant completed four runs ("tours") of eight blocks of trials of a single condition ("missions"). We describe the levels of each task condition below in more detail. Participants completed 32 total blocks of 10 trials each for a total of 320 trials in a single experimental session that lasted approximately 50 minutes. The order of blocks was counterbalanced within runs using a Latin square approach that minimized the correlation between block orders across runs for each participant, as well as across sessions for individuals who completed a second behavioral session.

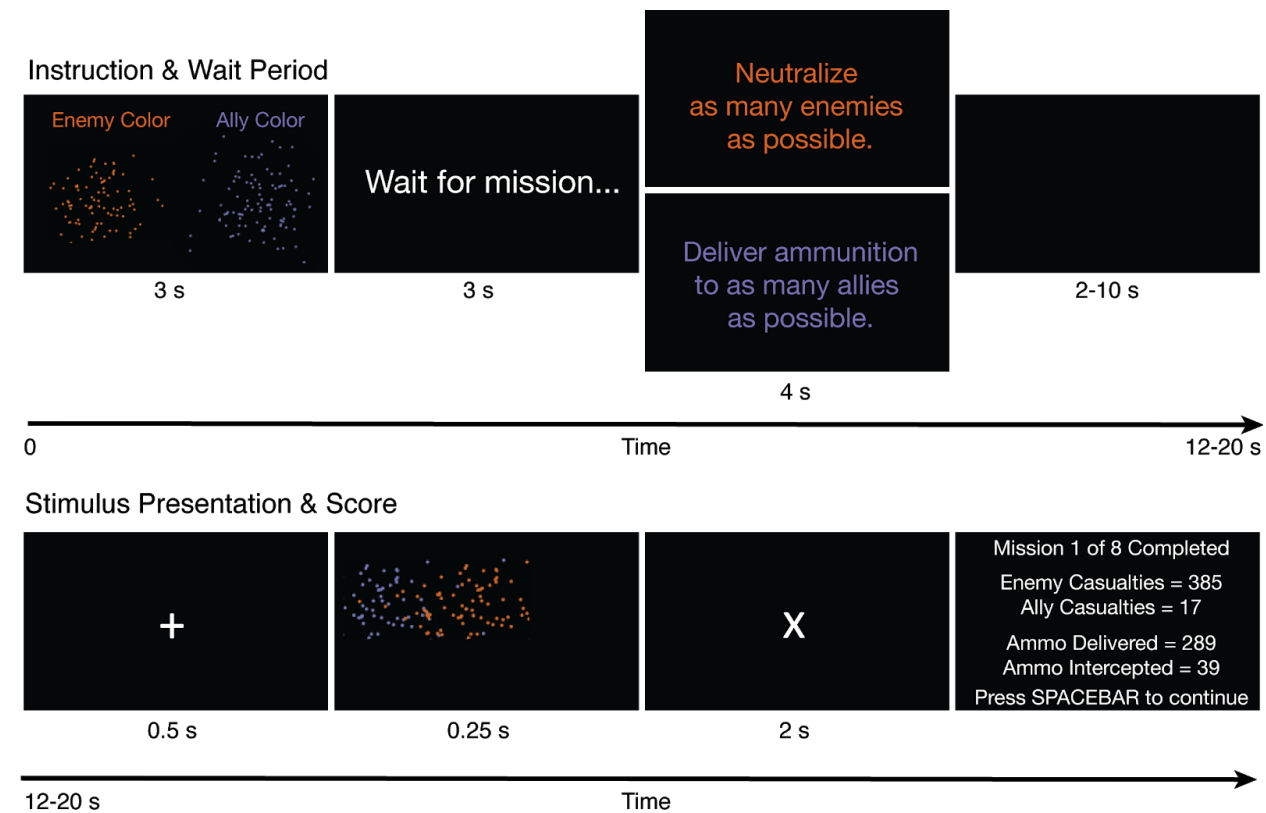


**Figure 3.2** Experimental block timeline. Each block, or “mission”, started with an instruction and wait period (top) where participants received a reminder of enemy and ally distribution colors for 3s followed by a 3 s wait period. A condition cue was then presented for 4 s in a font color the same as the target distribution for that block. A blank screen was then presented for 2-10 s (mean ITI = 4 s) prior to each trial. Stimulus presentation (bottom) began with a fixation (+) presented at the center of the screen. Participants had to click and hold the left button within 0.5 s of fixation onset to initiate the trial or else an “ABORT” message appeared indicating a failed trial. On a successfully initiated trial, the target and non-target stimulus distributions appeared onscreen for 0.25 s and then disappeared. Participants then had 2 s to indicate their target selection by dragging the cursor (x) and releasing the mouse button. Each block consisted of 10 trials, and a score report with a running total of enemy and ally casualties as well as ammunition delivered and intercepted was presented until the participant pressed the spacebar indicating that they were ready for the next block of trials. Note: Stimuli and fonts in figure are rescaled here for clarity.

On each block of trials, participants were tasked with using a computer mouse to select a location within a target stimulus distribution that was visually overlapped by a non-target stimulus distribution presented simultaneously onscreen (Figure 3.2). A wartime scenario was used to provide the contextual framing of each spatial selection, wherein participants selected the location of a missile strike on enemies or ammunition delivery to allies from a drone on a series of trials within a block. Before each block of trials, participants were presented for 3000 ms with a visual reminder of the colors that corresponded to the enemy and ally stimuli, which were either purple or orange. After a wait screen was presented for 3000 ms, the instruction for the upcoming set of trials was presented for 4000 ms. On “drone strike” missions, participants were instructed to “Neutralize as many enemies as possible” and to “Deliver ammunition to as many allies as possible” on “ammunition delivery” missions. In both cases, the color of the instruction text matched the target stimulus (i.e., enemies on drone strikes and allies on ammunition deliveries). Following the instruction period, a blank screen was presented before a fixation (+)

appeared at the center of the screen indicating the onset of a trial. The onset time for each trial within a block was uniformly sampled from a distribution of intertrial intervals ranging from 2000 ms to 10000 ms (mean ITI = 4000 ms).

To initiate the trial, the participant had to click and hold the left mouse button within 500 ms, otherwise they received an “ABORT!!!” message at the center of the screen indicating a failed trial. For successfully initiated trials, the target and non-target distributions were presented together for 250 ms before disappearing. Both the target and non-target distributions appeared completely on the screen. Each stimulus distribution was presented as a Gaussian distribution of 100 dots that were three pixels in diameter. The non-target distribution could appear either to the right or left of the target distribution with equal probability across trials. The means of the distributions were separated by fixed horizontal distance of 50 pixels and were randomly sampled from a distribution of 2D coordinates to appear a minimum of 350 pixels away from the center of the screen. On no-penalty blocks, the non-target stimulus distribution represented the position of trees, which were always green. On penalty blocks, the target and non-target distributions were the color of enemies and allies, respectively. In the low target variance conditions, the target standard deviation was set to 25 pixels and to 100 pixels in the high target variance condition. The standard deviation of the non-target distribution was fixed at 25 pixels across all trials.

After the stimulus distributions disappeared, the mouse cursor was immediately presented as an “x” at the center of the screen. Participants then had 2000 ms to drag the cursor to a location and then release the mouse button to indicate their selection for each drone strike or ammunition delivery. After a set of 10 trials in a block, a report screen was presented that

indicate the progress through the experiment along with a running total of enemies killed, allies killed, ammunition delivered, and ammunition intercepted. This report remained on the screen until any key on the keyboard was pressed by the participant to initiate the next run or block. A final score report screen was presented at the end of the session.

Regardless of context (i.e., drone strike or ammunition delivery), cost (i.e., no-penalty or penalty) or target variance (i.e., low or high) condition, selecting the mean of the target distribution guaranteed the maximum possible score on a trial. Equations 2-4 in Chapter 2 were used to calculate scores across trials. First, the Euclidean distance between a selection and the target distribution mean (*Equation 2.2*) and the non-target distribution mean (*Equation 2.3*) were computed. These distances were used in weighted hyperbolic functions with a  $1/d$  falloff to compute the score for each trial. *Equation 2.3* shows the target function weighted by  $\omega$  and the non-target by  $1-\omega$ . In no-penalty blocks,  $\omega = 1$ , so that only the selection distance from the target contributed to the score (i.e., no loss, only enemy kills or ammunition delivered), while  $\omega = 0.33$  to additionally reflect losses on penalty blocks as ally kills or ammunition intercepted. Here the computed scores were multiplied by 1000, rather than 100, and a rounded to yield an integer value between 0 and 100 for each trial. The total score for each block of 10 trials was added to a running total across all blocks within each experimental session.

### 3.2.3 Data Analysis

Selection bias away from the non-target, selection variability, reaction time (RT), movement time (MT), peak (i.e., maximum) mouse cursor velocity (maxV), and average mouse cursor velocity (avgV) served as dependent measures. The spatial location of a selection, the time

between stimulus offset and movement onset, as well as total movement time were recorded for every completed trial across all participants. Since the non-target position relative to the target was only manipulated on the horizontal dimension, only the horizontal selection distance was used in analyses of selection bias and variability. Selection bias was calculated as the difference between the target mean and the selection relative to position of the non-target. Specifically, selection bias takes more negative values at greater distances away from the non-target mean. Positive values thus indicate selections closer to the non-target mean (Figure 3.3). Selection variability was computed as the standard deviation of the x-coordinate of all selections within a condition. The position of the mouse was sampled at the screen refresh rate (60 Hz) and was used to compute the peak and average mouse velocity on each trial. All dependent measures were computed for all trials within a condition.

To further quantify any group-level main effects or interaction of cost (i.e., penalty) and target variance condition on selection bias between contexts (i.e., harm: drone strike vs. help: ammunition delivery), the mean selection bias in the help conditions was subtracted from the mean in the harm condition. We then subtracted those values in the no-penalty conditions from the values in the penalty conditions that matched on target variance to yield a difference score (i.e.,  $\Delta_{Harm-Help} = Bias_{Harm} - Bias_{Help}$ ). As such, negative  $\Delta_{Harm-Help}$  values reflect a larger bias away from the non-target in harm conditions than help conditions. Conversely, positive  $\Delta_{Harm-Help}$  values would indicate that selections were closer to the non-target in harm conditions. This also allowed us to compute a correlation between  $\Delta_{Harm-Help}$  values in low and high target variance conditions to examine whether or not there was a group-level relationship between how much more (or less) participants biased selections away from the non-target under each level of

target variance within each cost condition. Next, we more generally examined whether participants showed harm aversion selection bias in penalty conditions under each combination of low and high target variance by categorizing  $\Delta_{Harm-Help}$  values into four cells, or quadrants (Q-I through Q-IV) (see Table 3.4 and Figure 3.4). Moving counterclockwise beginning with the upper right quadrant, participants in Q-I would be categorized as less harm averse since  $\Delta_{Harm-Help}$  would be positive in both low and high target variance conditions. Participants in Q-II and Q-IV are then only harm averse in either the high or low target variance condition, respectively. If a participant falls in Q-III, then they would be harm averse in both variance conditions. Also, if more participants generally show less bias away from the non-target in no-penalty conditions but are harm averse in penalty conditions overall, then we should see a greatest proportion of  $\Delta_{Harm-Help}$  values shift from Q-I to Q-III. Based on these categorizations, we first calculated the ratios of  $\Delta_{Harm-Help}$  values in each quadrant as a preliminary estimate of the shift magnitude. Shift ratios greater than 1 thus indicate a larger number of participants with  $\Delta_{Harm-Help}$  values in a given quadrant in penalty conditions versus no-penalty conditions. We then performed a  $\chi^2$  goodness-of-fit test to determine whether or not the observed number of participants in each quadrant deviated significantly from the expected number. Lastly here, we computed the  $\Delta_{Harm-Help}$  value centroids (i.e., means) with 95% confidence intervals along the x and y axes within Q-I and Q-III (Figure 3.4, bottom panel).

All dependent variables were subjected to a three-way repeated measures ANOVA to observe whether there were any significant 3-way and 2-way interactions or main effects of context, cost, or target variance (Figure 3.3 and Tables 3.1-3.3). Since six dependent variables were subject to ANOVA, a Bonferroni correction of  $\alpha$  of  $0.05/6 = 0.008$  was used as a threshold

for statistical significance. For significant results on omnibus F tests, effect sizes were estimated as  $\eta_p^2$ . To account for the possibility of finding no significant differences between context conditions, a two-way repeated measures ANOVA was planned for data collapsed across (i.e., controlling for) context conditions to observe any expected significant main effects or interactions between cost and variance (Jarbo, Flemming, & Verstynen, 2017). In order to determine the directionality of significant main effects or interactions from the omnibus F tests, we report the group means and standard errors for each dependent variable across all conditions, and the results of 1-sample and paired sample t-tests with effect sizes computed as Cohen's d.

### 3.3 Results

Here we describe the interactions or main effects of target variance (Low vs High), cost (No Penalty vs Penalty), and context (Harm vs Help) on selection bias, with a focus on differences between harm and help conditions, as well as the five other dependent measures of interests: selection variability (SV), RT, MT, maxV, and avgV (Figure 3A-F). We refer the reader to Tables 1-3 for all statistics, including group means and standard errors for each dependent variable. Corresponding figures and panels for each dependent variable are referenced in the text.

**Table 3.1** ANOVA results of 2-way and 3-way interactions for dependent variables: selection bias, selection variability (SV), RT, MT, maxV, and avgV.

|   | DV   | F(1,43) | p       | Sig. | $\eta_p^2$ |  | DV   | F(1,43) | p     | Sig. | $\eta_p^2$ |
|---|------|---------|---------|------|------------|--|------|---------|-------|------|------------|
| Context<br>x<br>Cost                      | Bias | 20.286  | < 0.001 | ***  | 0.321      |  | MT   | 2.815   | 0.101 | ns   | -          |
|   | SV   | 2.410   | 0.128   | ns   | -          |  | maxV | 0.013   | 0.910 | ns   | -          |
|   | RT   | 0.184   | 0.670   | ns   | -          |  | avgV | 0.899   | 0.348 | ns   | -          |
| Context<br>x<br>Varianc<br>e              | Bias | 1.016   | 0.319   | ns   | -          |  | MT   | 2.427   | 0.127 | ns   | -          |
|   | SV   | 0.006   | 0.937   | ns   | -          |  | maxV | 0.187   | 0.667 | ns   | -          |
|   | RT   | 0.038   | 0.846   | ns   | -          |  | avgV | 0.191   | 0.665 | ns   | -          |
| Cost<br>x<br>Varianc<br>e                 | Bias | 8.32    | 0.006   | ***  | 0.162      |  | MT   | 0.459   | 0.502 | ns   | -          |
|   | SV   | 6.604   | 0.014   | *    | 0.133      |  | maxV | 0.928   | 0.341 | ns   | -          |
|   | RT   | 1.215   | 0.276   | ns   | -          |  | avgV | 0.007   | 0.932 | ns   | -          |
| Context<br>x<br>Cost<br>x<br>Varianc<br>e | Bias | 1.14    | 0.291   | ns   | -          |  | MT   | 0.734   | 0.396 | ns   | -          |
|   | SV   | 2.659   | 0.110   | ns   | -          |  | maxV | 0.457   | 0.503 | ns   | -          |
|   | RT   | 1.531   | 0.223   | ns   | -          |  | avgV | 0.637   | 0.429 | ns   | -          |

Bonferroni-corrected  $\alpha = 0.008$  denoted by (\*\*\*)� Significant uncorrected p-value  $\alpha = 0.05$  denoted by (\*). Same significance thresholds in Tables 3.2 and 3.3.

**Table 3.2** ANOVA and post hoc t-test results of main effects for dependent variables: selection bias, SV, RT, MT, maxV, and avgV.

|              | DV   | F(1,43) | p       | Sig. | $\eta_p^2$ |         | t(43)   | p   | Sig.    | Cohen's d |
|--------------|------|---------|---------|------|------------|---------|---------|-----|---------|-----------|
| Context      | Bias | 0.194   | 0.662   | ns   | -          |         | -       | -   | -       | -         |
|              | SV   | 2.494   | 0.122   | ns   | -          |         | -       | -   | -       | -         |
|              | RT   | 0.193   | 0.662   | ns   | -          |         | -       | -   | -       | -         |
|              | MT   | 1.299   | 0.261   | ns   | -          |         | -       | -   | -       | -         |
|              | maxV | 0.843   | 0.364   | ns   | -          |         | -       | -   | -       | -         |
|              | avgV | 1.793   | 0.188   | ns   | -          |         | -       | -   | -       | -         |
| Cost         | Bias | 41.878  | < 0.001 | ***  | 0.493      | 6.471   | < 0.001 | *** | 0.9755  |           |
|              | SV   | 25.405  | < 0.001 | ***  | 0.371      | -5.040  | < 0.001 | *** | -0.7598 |           |
|              | RT   | 16.585  | < 0.001 | ***  | 0.278      | -4.072  | < 0.001 | *** | -0.6139 |           |
|              | MT   | 30.367  | < 0.001 | ***  | 0.414      | -5.511  | < 0.001 | *** | -0.8308 |           |
|              | maxV | 26.207  | < 0.001 | ***  | 0.379      | 5.119   | < 0.001 | *** | 0.7717  |           |
|              | avgV | 29.803  | < 0.001 | ***  | 0.409      | 5.459   | < 0.001 | *** | 0.8230  |           |
| Varianc<br>e | Bias | 112.100 | < 0.001 | ***  | 0.723      | 10.590  | < 0.001 | *** | 1.5965  |           |
|              | SV   | 274.183 | < 0.001 | ***  | 0.864      | -16.560 | < 0.001 | *** | -2.4965 |           |
|              | RT   | 16.529  | < 0.001 | ***  | 0.278      | -4.066  | < 0.001 | *** | -0.6130 |           |
|              | MT   | 89.336  | < 0.001 | ***  | 0.675      | 9.452   | < 0.001 | *** | 1.4249  |           |
|              | maxV | 9.725   | 0.003   | ***  | 0.184      | 3.119   | 0.003   | *** | 0.4702  |           |

|             |        |         |     |       |        |         |     |         |
|-------------|--------|---------|-----|-------|--------|---------|-----|---------|
| <i>avgV</i> | 79.549 | < 0.001 | *** | 0.649 | -8.919 | < 0.001 | *** | -1.3446 |
|-------------|--------|---------|-----|-------|--------|---------|-----|---------|

Post hoc paired t-tests for Cost = no-penalty - penalty and Variance = low - high.

**Table 3.3** Condition-wise group (N = 44) means and standard errors (SE) for dependent variables: selection bias, SV, RT, MT, maxV, and avgV.

| Condition                                | Bias (pixels) |      | SV (pixels) |      | RT (ms) |     | MT (ms) |      | maxV<br>(pixels/s) |      | avgV<br>(pixels/s) |       |
|--|---------------|------|-------------|------|---------|-----|---------|------|--------------------|------|--------------------|-------|
|  | M             | SE   | M           | SE   | M       | SE  | M       | SE   | M                  | SE   | M                  | SE    |
| <i>Harm</i><br>No Penalty<br><i>Low</i>  | -3.49         | 1.83 | 25.82       | 2.55 | 33.0    | 2.1 | 601.7   | 28.5 | 81.78              | 2.08 | 14.99              | 0.500 |
| <i>Harm</i><br>No Penalty<br><i>High</i> | -24.27        | 3.43 | 55.00       | 3.50 | 38.1    | 2.9 | 507.7   | 24.9 | 79.71              | 2.41 | 16.83              | 0.578 |
| <i>Harm</i><br>Penalty<br><i>Low</i>     | -27.40        | 3.91 | 42.56       | 4.04 | 36.0    | 2.4 | 646.9   | 29.7 | 79.57              | 2.29 | 14.38              | 0.518 |
| <i>Harm</i><br>Penalty<br><i>High</i>    | -55.98        | 4.29 | 81.27       | 4.43 | 43.5    | 4.1 | 552.3   | 28.3 | 77.02              | 2.36 | 16.10              | 0.602 |
| <i>Help</i><br>No Penalty<br><i>Low</i>  | -4.97         | 1.69 | 27.80       | 2.74 | 32.6    | 1.9 | 593.8   | 26.4 | 82.05              | 2.08 | 15.10              | 0.504 |
| <i>Help</i><br>No Penalty<br><i>High</i> | -28.42        | 3.33 | 60.01       | 3.85 | 38.5    | 2.8 | 515.8   | 25.4 | 80.10              | 2.42 | 16.78              | 0.613 |
| <i>Help</i><br>Penalty<br><i>Low</i>     | -25.31        | 4.06 | 43.84       | 4.86 | 36.2    | 2.3 | 635.8   | 27.5 | 80.37              | 2.19 | 14.51              | 0.511 |
| <i>Help</i><br>Penalty<br><i>High</i>    | -53.69        | 3.79 | 79.83       | 5.94 | 42.4    | 3.6 | 546.6   | 27.1 | 77.03              | 2.29 | 16.27              | 0.603 |

### 3.3.1 Selection bias

Selection bias was measured as the distance, in pixels, between a selection and the target mean on a trial (Figure 3.3a). More negative values indicate selections further from the target mean in the direction away from the non-target. Positive values indicate selections closer to the

non-target distribution. Though the 3-way interaction between context, cost, and target variance was not significant, we observed significant cost x target variance,  $F(1,43) = 8.32$ ,  $p = 0.006$ ,  $\eta_p^2 = 0.162$  and context x cost interactions,  $F(1,43) = 20.286$ ,  $p < 0.001$ ,  $\eta_p^2 = 0.321$  (Table 3.1). The main effect of context was not significant,  $F(1,43) = 0.194$ ,  $p = 0.662$ , but both main effects of cost,  $F(1,43) = 41.878$ ,  $p < 0.001$ ,  $\eta_p^2 = 0.493$ , and target variance,  $F(1,43) = 112.100$ ,  $p < 0.001$ ,  $\eta_p^2 = 0.723$  were significant (Table 3.2). In general, selection bias was negative across all conditions, all  $t(43)s < -2.944$ , all  $ps < 0.006$ , all Cohen's  $ds < -0.444$ , except in the harm by no-penalty by low target variance condition (see Table 3.3 and Figure 3.3a). Following the omnibus F tests, a post hoc paired sample t-test showed that bias had significantly greater magnitude in penalty than no-penalty conditions,  $t(43) = 6.471$ ,  $p < 0.001$ , Cohen's  $d = 0.976$ , indicating that the context x cost interaction was driven by the penalty condition. Selection bias was also larger in high target variance than low target variance conditions,  $t(43) = 10.590$ ,  $p < 0.001$ , Cohen's  $d = 1.597$ . Lastly here, a paired t-test revealed that selection bias was significantly larger in penalty conditions in the harm context than in the help context,  $t(87) = -2.090$ , one-sided  $p = 0.020$ , Cohen's  $d = -0.223$ . We note that the significant two-way interaction between cost and variance replicates the findings presented in Chapter 2 (Table 3.1).

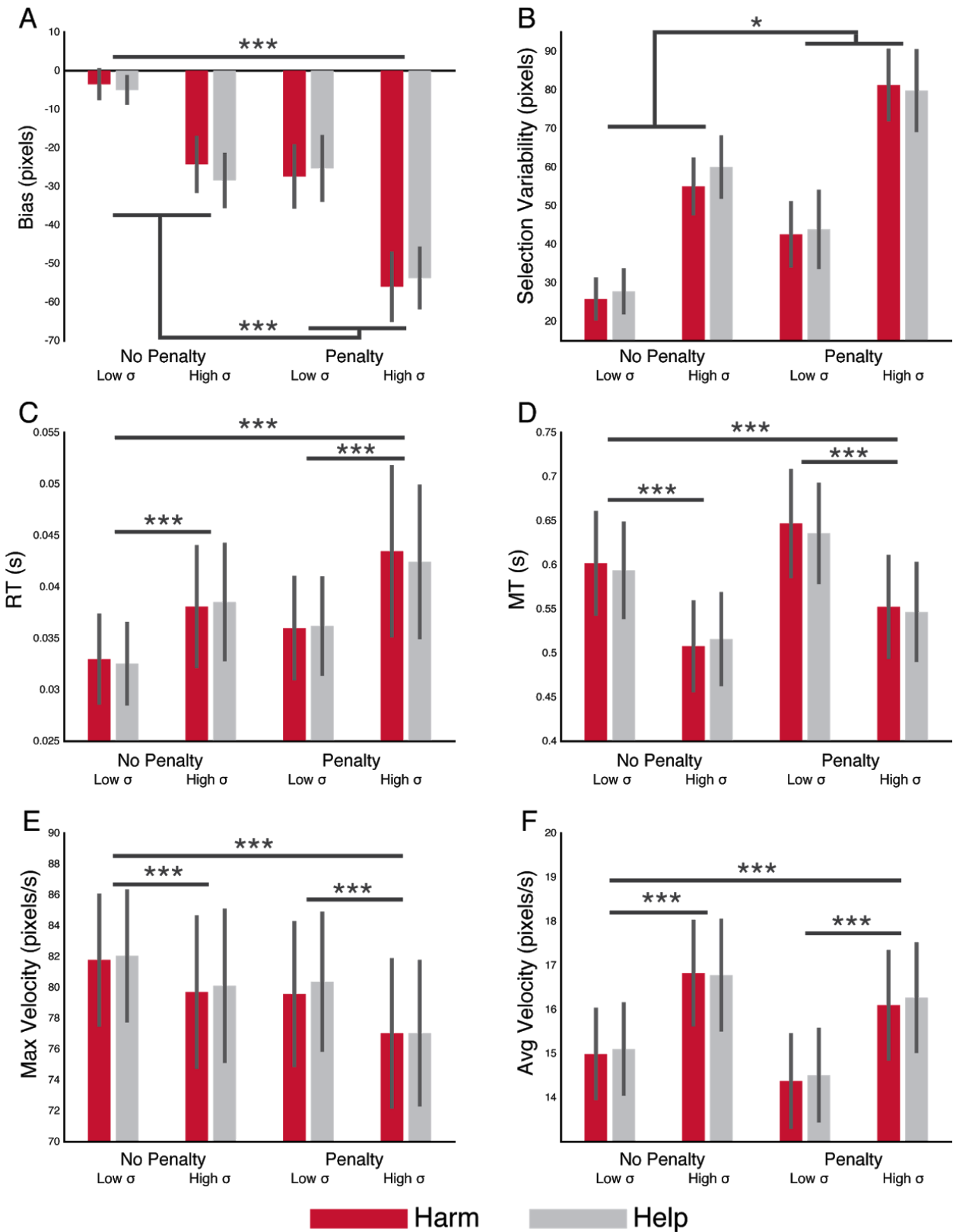


**Figure 3.3** Bar graphs with significant interactions and main effects. In each panel, bars (red/left= harm, gray/right = help) represent the group means of each dependent variable across all conditions with error bars reflecting the 95% confidence intervals of the means. Bonferroni-corrected  $\alpha = 0.008$  denoted by \*\*\* and uncorrected  $p < 0.05$  by \*. A) Selection bias measured in pixels and larger negative values indicate selections further away from the non-target distribution, while less negative and positive values reflect closer selections. Significant 2-way context x cost interaction is denoted by the long horizontal line at the top of the panel. A significant 2-way cost x variance interaction as well as significant main effects of cost and variance are denoted by medium-length and short horizontal lines in the bottom half of the panel. B) Selection variability is measured as the standard deviation of selections in pixels. Greater values correspond to greater selection variability. Horizontal lines represent a significant 2-way cost x variance interaction as well as significant main effects of cost and variance. There were no significant interactions for RT, MT, maximum and average velocity, represented in panels C-F. Though significant main effects of cost and variance were observed for each as denoted by the long and short horizontal lines. Greater values for RT and MT reflect slower times, while greater values for both velocity measures indicate faster mouse movements. All significant interactions, main effects, group means and standard errors are also reported in Tables 3.1-3.3.

### 3.3.2 Harm versus help differences

We computed a value,  $\Delta_{Harm-Help}$ , to quantify and evaluate differences in selection bias between the harm and help contexts. Then, we calculated the Pearson correlation between  $\Delta_{Harm-Help}$  values in the low and high variance conditions and found no significant linear relationship between selection bias in penalty conditions,  $r = -0.081$ ,  $p = 0.600$ , or no-penalty conditions,  $r = 0.164$ ,  $p = 0.288$ . Nor did we find a significant correlation in selection bias after collapsing across cost conditions,  $r = -0.190$ ,  $p = 0.216$ . Given the null correlation findings, we next categorized selection bias differences by plotting the  $\Delta_{Harm-Help}$  values in four distinct quadrants (see Table 3.4 and Figure 3.4). Specifically, we compared the counts of participants whose  $\Delta_{Harm-Help}$  values fell into each quadrant under no-penalty and penalty conditions as well as low

and high variance conditions. If participants generally found the harm context more aversive in penalty conditions, then we should observe the highest count of  $\Delta_{Harm-Help}$  values shift from Q-I in no-penalty conditions, where participants were selecting closer to the non-target, to Q-III in penalty conditions, where selections were biased away from the non-target regardless of variance. We report these values in Table 3.4. As expected, in no-penalty conditions, half ( $n = 22$ ) of the  $\Delta_{Harm-Help}$  values were in Q-I while only five were observed in Q-III (Figure 3.4a). In penalty conditions, Q-I had the fewest  $\Delta_{Harm-Help}$  values ( $n = 5$ ) while the remaining ( $n = 39$ ) were dispersed nearly evenly across the other three quadrants indicating that most participants were harm averse in penalty conditions in at least one level of target variance (Figure 3.4b). This provides additional confirmation of the significant context x cost interaction, such that the majority of participants select closer to the non-target in no-penalty conditions.

We further quantified the extent to which participants as a group were more likely to bias selections away from the non-target in the harm context by computing the ratio of counts in each quadrant between penalty and no-penalty conditions. The shift ratios for Q-II through Q-IV were all greater than 1 with the largest shift ratio of 2.400 for Q-II, indicating that participants showed a greater non-target avoidance driven by penalty in harm contexts, especially under high target variance conditions. In Q-III, the shift ratio of 1.875 shows that participants were nearly twice as likely to significantly bias selections in harm conditions with penalty. To more closely evaluate the shift from Q-I to Q-III (i.e., less selection bias versus more selection bias at both target variance levels), we computed a composite  $\Delta_{Harm-Help}$  score collapsed across no-penalty and penalty conditions with 95% confidence intervals. This showed that participants with less harm aversive selection bias behavior overall fell within Q-I ( $x\text{-mean}_{Q-I} = 6.798$ , 95% CI  $x_{Q-I}$ : [-1.100,

14.696]; y-mean<sub>Q-I</sub> = 4.076, 95% CI y<sub>Q-I</sub>: [-0.084, 8.235]), while more harm averse participants fell within Q-III (x-mean<sub>Q-III</sub> = -9.928, 95% CI x<sub>Q-III</sub>: [-14.547, -5.310]; y-mean<sub>Q-III</sub> = -7.998, 95% CI y<sub>Q-III</sub>: [-10.664, -5.333]) (Figure 3.4C). Lastly here, the  $\chi^2$  goodness-of-fit test confirmed that the observed number of participants in this sample were not equally distributed across quadrants,  $\chi^2(3, N = 44) = 11.455, p < 0.01$ . Together, the results of  $\Delta_{Harm-Help}$  values show that framing spatial decisions as potentially harmful can increase aversive selection bias regardless of uncertainty in the estimates of sensory variance.

**Table 3.4** Contingency table of observed  $\Delta_{Harm-Help}$  value frequencies in each quadrant and shift ratios between and collapsed across penalty and no-penalty conditions.

| Quadrant | Penalty | No-Penalty | Shift Ratio | Collapsed (Expected) |
|----------|---------|------------|-------------|----------------------|
| I        | 5       | 22         | 0.227       | 5 (11)               |
| II       | 12      | 5          | 2.400       | 11 (11)              |
| III      | 15      | 8          | 1.875       | 20 (11)              |
| IV       | 12      | 9          | 1.333       | 8 (11)               |

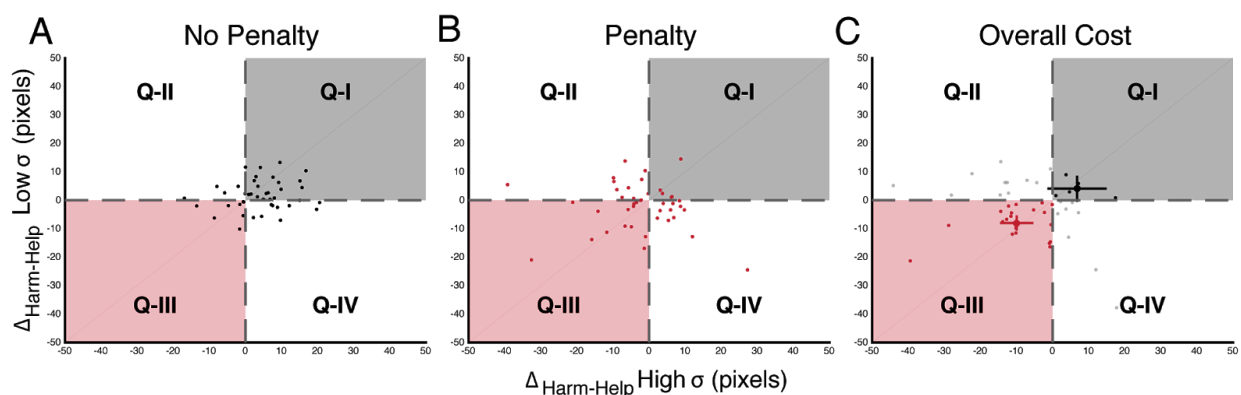


**Figure 3.4** Scatter plots and quadrant centroids for  $\Delta_{Harm-Help}$  shift analysis. All plotting conventions are the same across all panels. Each dot reflects the  $\Delta_{Harm-Help}$  value for each individual participant. The x- and y-axis respectively represent  $\Delta_{Harm-Help}$  values

measured in pixels within high and low variance conditions. Quadrant Q-I (gray) contains  $\Delta_{Harm-Help}$  values for participants with less harm aversive selection bias, while Q-III (light red) contains  $\Delta_{Harm-Help}$  values for participants with more harm aversive selection bias regardless of variance conditions. A)  $\Delta_{Harm-Help}$  values for no-penalty conditions primarily clustered in quadrant I (Q-I). B) In penalty conditions,  $\Delta_{Harm-Help}$  values are more broadly distributed throughout Q-II to Q-IV (see Table 3.4). C)  $\Delta_{Harm-Help}$  values were collapsed within variance conditions to generate a composite harm avoidance measure, reflecting overall selection behavior irrespective of target variance or cost condition. Centroids with 95% CIs on the x- and y-axis were computed for participants within Q-I (black) and Q-III (red).

### 3.3.3 Selection variability

To estimate selection variability, we computed the standard deviation of the error, in pixels, between a selection and the mean of the target distribution. The cost x variance interaction,  $F(1,43) = 6.604$ ,  $p = 0.014$ ,  $\eta_p^2 = 0.133$ , and both main effects of cost,  $F(1,43) = 25.405$ ,  $p < 0.001$ ,  $\eta_p^2 = 0.371$ , and variance,  $F(1,43) = 274.183$ ,  $p < 0.001$ ,  $\eta_p^2 = 0.864$ , were all significant (Figure 3.3b, Table 3.1, and Table 3.2). For context conditions, there were no significant interactions or main effects, all  $F(1,43)s < 2.66$ , all  $ps > 0.110$ , (Tables 3.1 and 3.2). Post hoc paired sample t-tests showed that selection variability was greater in penalty than no-penalty conditions,  $t(43) = -5.040$ ,  $p < 0.001$ , Cohen's  $d = -0.760$ , and in high versus low variance conditions,  $t(43) = -16.560$ ,  $p < 0.001$ , Cohen's  $d = -2.450$  (Table 3.2 and Table 3.3), also replicating the findings presented in Chapter 2.

### 3.3.4 Reaction and movement time

Reaction time was recorded at the first mouse movement detected after stimulus offset. There were no significant interactions nor main effect of context on RT or MT, all  $F(1,43)s < 2.815$ , all

$ps > 0.101$ . For RT, we found very similar significant main effects of both cost,  $F(1,43) = 16.585$ ,  $p < 0.001$ ,  $\eta_p^2 = 0.278$ , and target variance  $F(1,43) = 16.529$ ,  $p < 0.001$ ,  $\eta_p^2 = 0.278$  (Figure 3.3c and Table 3.2). RTs were slower in both penalty,  $t(43) = -4.072$ ,  $p < 0.001$ , Cohen's  $d = -0.6139$ , and high variance conditions,  $t(43) = -4.066$ ,  $p < 0.001$ , Cohen's  $d = -0.613$  (Tables 3.2 and 3.3). Movement time was computed as the difference between the time recorded when the selection was made (i.e., mouse button released at selection location) and the RT on a trial. While there was no significant interaction between the cost and target variance, there were significant main effects for both cost,  $F(1,43) = 30.367$ ,  $p < 0.001$ ,  $\eta_p^2 = 0.414$ , and variance,  $F(1,43) = 89.336$ ,  $p < 0.001$ ,  $\eta_p^2 = 0.675$  (Figure 3.3d and Table 3.2). In penalty conditions, MTs were significantly longer than in no-penalty conditions,  $t(43) = -5.511$ ,  $p < 0.001$ , Cohen's  $d = -0.831$ . MTs were also significantly longer in low, rather than high, target variance conditions,  $t(43) = 9.452$ ,  $p < 0.001$ , Cohen's  $d = 1.425$  (Tables 3.2 and 3.3). Overall, participants took longer to initiate movement and make a selection on trials in penalty conditions. Under high variance conditions, RTs were slower but MTs were shorter, indicating that participants spent more time completing their selections in low variance conditions, i.e., when there was low sensory uncertainty in target distribution estimates.

### 3.3.5 Maximum and average movement velocity

By recording mouse cursor positions and button presses along with RT and MT, we computed the maximum and average velocity of the mouse cursor movements during selections on each trial. There were no significant interactions or main effect of context on maxV or avgV, all  $F(1,43)s < 0.928$ , all  $ps > 0.341$ . There was a significant main effect of cost on both maxV,

$F(1,43) = 26.207$ ,  $p < 0.001$ ,  $\eta_p^2 = 0.379$ , and  $\text{avgV}$ ,  $F(1,43) = 29.803$ ,  $p < 0.001$ ,  $\eta_p^2 = 0.409$

(Figure 3.3e and f and Table 3.2). Post hoc t-tests showed greater (faster)  $\text{maxV}$ ,  $t(43) = 5.119$ ,  $p < 0.001$ , Cohen's  $d = 0.772$ , and  $\text{avgV}$ ,  $t(43) = 5.459$ ,  $p < 0.001$ , Cohen's  $d = 0.823$ , in no-penalty conditions compared with penalty conditions. Though the main effect of variance was significant for both velocity measures,  $\text{maxV}$  was significantly greater (faster) in low target variance conditions,  $t(43) = 3.119$ ,  $p = 0.003$ , Cohen's  $d = 0.470$ , while  $\text{avgV}$  was slower,  $t(43) = -8.919$ ,  $p < 0.001$ , Cohen's  $d = -1.345$  (Tables 3.2 and 3.3). As would be expected, the results for both velocity metrics parallel the MT findings in that participants moved more slowly in penalty conditions and low target variance conditions where MTs were also significantly longer.

### 3.4 Discussion

In this chapter, we present a second novel behavioral experiment to address Specific Aim 1.2 that establishes the effects of contextual framing on loss avoidance during risky spatial decisions, and additionally replicates and extends the findings presented in Chapter 2. First, this study shows that under equivalent conditions of value-based risk and sensory uncertainty, the contextual framing of loss outcomes as subjectively more aversive (i.e., ally casualties) increases selection bias away from a penalizing non-target to a greater degree than less aversive loss outcomes (i.e., ammunition interception). Second, the findings here replicate the observed effects of cost and variance on selection bias, selection variability, and reaction time presented in Chapter 2. In addition to these replications, analyses of movement time, maximum and average mouse cursor velocity allowed for a fuller characterization of selection behavior that suggests individuals made selection decisions more cautiously under the threat of potential loss by taking

significantly longer to initiate and complete selections, moving more slowly overall throughout the movement. Critically, the results of this study show that though different contextual frames did not change how selections were executed motorically, subjectively more aversive framing of potential loss outcomes uniquely drives avoidant action decision behavior.

By superimposing a wartime scenario on the original Danger Zone paradigm, this experiment allowed me to explore the effects of contextual framing on risky spatial decisions. Irrespective of task context, the visuospatial features of the stimuli as well as the scoring function used to compute gains and losses were equivalent across all experimental conditions. The overall goal of the task was to maximize expected gain by either neutralizing the most enemies or delivering the most ammunition to allies as possible. To those ends, the optimal selection on any trial is always the spatial mean of the target distribution. As such, any bias away from or toward the non-target distribution mean reflects a suboptimal selection strategy. Based on prior work, participants were expected to show greater selection bias away from regions of space that induce penalties in feedback so as to avoid losses i.e., ally casualties or ammunition interceptions (Jarbo et al., 2017; Neyedli & Welsh, 2013; Trommershäuser et al., 2003a, 2003b; Wu et al., 2006). However, if participants were only using spatial estimates of the target and non-target means, as well as the scoring feedback, then there should have been no difference in selection bias between conditions. Even though both kinds of loss were undesirable, participants biased selections to avoid the potential collateral losses incurred on a drone strike mission (harm context) to a small (see Section 3.3.1, Cohen's  $d = -0.223$ ) but significantly greater extent than on a delivery mission (help context). These findings are further supported by our group-level  $\Delta_{Harm-Help}$  analyses, which showed that participants shifted their behavior to bias selections away from the non-target

in harm contexts regardless of variance at nearly twice the rate (mean shift ratio Q-II to Q-IV = 1.869) of penalty conditions than in no-penalty conditions. Though the context effect is small, there is a marked shift in the degree to which participants are generally averse to losses that are perceived as harmful regardless of the level of sensory uncertainty during risky spatial decisions. Importantly, the harm and help contexts provided additional information that was incorporated into the selection decision in a way that made one kind of loss subjectively worse than the other despite all other features of the task being equal.

In addition to increased selection bias, the analysis of several other dependent variables indicates that loss averse selection behavior is also reflected in the timing and velocity of movement initiation and execution. First, selection variability and reaction times increased in high target variance and penalty conditions, replicating my previous findings (see Section 2.3). Our observation that selection variability increases with target variance is consistent with prior research and indicates that a greater spread of target distribution dots results in larger errors in estimating the target mean (Battaglia & Schrater, 2007; Jarbo et al., 2017; Tassinari, Hudson, & Landy, 2006). Data on total movement time, maximum and average mouse cursor velocity showed that participants took longer to complete their selections and moved more slowly overall in penalty conditions. Regarding target variance effects, even though participants had faster RTs in low variance conditions, MTs were also longer, when there was less sensory uncertainty. Together, the timing and velocity data suggest that participants took a more cautious approach to executing selections when penalty was a factor in the decision. This is in line with a body of established findings on speed-accuracy tradeoffs wherein people sacrifice speed in order to improve accuracy on sensorimotor tasks (Fitts, 1954; Harris & Wolpert, 1998; Meyer et al.,

1988; Trommershäuser et al., 2003b; Wu et al., 2006). Considering the timing and velocity findings together with lower observed selection bias in low variance conditions suggests that participants put more effort into executing selections in an attempt to maximize expected gain when they could be more confident in their sensory estimates. Future work can more closely examine how motor effort and sensory estimation confidence impact spatial selection behavior under risk.

Some degree of the selection bias effects we observed here could be based on noisy estimates of sensory uncertainty. In an experiment by Juni and colleagues (2016), participants had to select on a touchscreen a hidden target whose location could be estimated from a 2D Gaussian distribution of dots where each dot appeared one at a time in random order. A participant could request additional dots to increase their certainty in the sensory estimates of the target location but lost and increasing amount of points with the number of dots requested. This resulted in participants selecting locations from a cluster of dots to minimize point loss once they subjectively determined that there was a sufficiently dense cluster present. The authors found that participants requested more dots than required by an ideal (optimal) observer to accurately estimate the target location, suggesting that individuals failed to maximize expected gain by using a suboptimal decision-making strategy in situations with high sensory uncertainty (Juni et al., 2016). In the present study, our participants could have also been targeting areas in the stimulus that they perceived to have the densest cluster of dots in the high target variance conditions. However, since the stimuli were comprised of 2D Gaussian distributions, the densest cluster of target dots was still most likely to be centered on the target mean, in accord with the law of large numbers. Bear in mind that participants were explicitly instructed to select the target

center in order to maximize gain regardless of condition. Despite those instructions, some participants could have also adopted a “densest cluster” strategy based on their estimate of the scoring function if they thought that strategy would improve their score. One reason for this might be that participants assumed that, in reality, a drone strike would have a blast radius about the selection location, whereas an ammunition delivery would be received only at the selection location. To better assess strategic task performance, a future version of this study could directly manipulate the location of the densest cluster dots within the target distribution relative to the distribution’s mean to determine whether participants used a “densest cluster” or “spatial center” strategy, as well as ask participants for explanations of their selection decision strategies across different conditions.

Despite all other aspects of the task being equal, this study is somewhat limited in explaining why contextual framing differences resulted in participant behavior that was indicative of greater loss aversion in harm conditions than help conditions. For example, we did not explore whether any idiosyncrasies in moral or ethical dispositions mediated selection bias. Some people who are more consequentialist in their reasoning, i.e., who decide how morally good or bad an action is based solely the action’s consequences (Kagan, 1988), would likely be more impartial to both kinds of loss and would have maximized expected gain in an Utilitarian (Mill, 1863; Moore, 1903) way by neutralizing the most enemies and delivering ammunition to the most allies possible, regardless of ally casualties or intercepted ammunition, respectively. To explore this more deeply, we can obtain and analyze measures of Utilitarian ethical dispositions (Kahane et al., 2017) to determine whether a person characterized as “less Utilitarian” avoids potentially harmful losses to a greater extent than a person who is “more Utilitarian” and would

more readily accept losses in order to maximize gain. Additionally, we assumed that the harm and help contexts we developed ensured that the harm context simply posed a more aversive loss than the help context. However, this relationship between context and aversion may not be so straightforward, as judgments about harmful and helpful actions have also been linked to subjective beliefs about intentionality (Cushman, Knobe, & Sinnott-Armstrong, 2008; Knobe, 2003a) and the probabilities of action outcomes (Nakamura, 2018). As such, some questions that are beyond the scope of the work here remain about whether participants thought their choices were causing harm or helping, as well as how likely the harmful or helpful outcome would be if they attempted to maximize expected gain rather than avoid loss. So, while moral dilemmas provided a strong contextual framing manipulation for this experiment, carefully designed future work can begin to address complex open questions about the rationale participants used for making selection decisions.

Within the broader literature in psychology, contextual framing effects have been shown to impact mental processes by changing how information is subjectively perceived, which subsequently influences behavior on cognitive tasks that do not involve sensory or motor processes used in spatial decision-making tasks. For instance, contextual framing like shifts in perspective impact information encoding and retrieval (Anderson & Pichert, 1978). When individuals were primed with a particular perspective to frame their approach to a memory task, they were able to recall different details about a vignette they read, suggesting that contextual framing can influence what information is remembered and, thus available to be retrieved. Drone Strike does involve both visuospatial working memory, and working memory more generally, to encode and represent the briefly presented location of stimuli on each trial and maintain task

instructions across a set of trials. Depending on which task instructions frame the stimuli, participants may show differences in their perceptions of non-target salience and in how accurately they can recall its position, especially when losses must be avoided. Also, in classic work on decision-making and reasoning, reframing logic problems to be more socially relevant to an individual can also increase the likelihood that they arrive at valid conclusions suggesting that context can influence reasoning processes (Cosmides & Tooby, 1992; Griggs & Cox, 1982; Wason, 1968; Wason & Shapiro, 1971). Along with the Knobe effect (see Section 3.1.2), other work in experimental philosophy has used the *trolley* and *footbridge* problems to contextualize a moral dilemma in fictional vignettes where an individual must kill one person in order to save five others, and has shown that people reason differently about whether the individual intentionally killed the one person (Greene, Sommerville, Nystrom, Darley, & Cohen, 2001; Sinnott-Armstrong, Mallon, McCoy, & Hull, 2008; Thomson, 1986). From an economic standpoint, the outcome of the decision is the same, but people judge the act of killing--and, thus the decision to kill itself--differently across vignettes. This sort of moral reasoning may have played a role in Drone Strike where, as we hypothesized, participants judged ally casualties as a subjectively worse *kind* of loss than intercepted ammunition, even though the spatial distributions and scoring functions were equivalent across contexts. The present study provides evidence that the contextual framing of a risky spatial decision impacts sensorimotor processes and behavior, and suggests a potential mechanism of cognitive penetration, wherein the perceptual representation of sensory information biases value-based action decisions.

### 3.5 Conclusion

This novel experiment extends the findings and application of my prior work presented in Chapter 2 and shows that the contextual framing of loss impacts avoidance during risky spatial decision-making. By analyzing the effects of context, cost, and target variance on additional dependent variables, we also provide a more complete description of selection behavior. The adaptation of the Danger Zone experiment as Drone Strike here, illustrates how my novel paradigm can be used to build a more comprehensive understanding of risky decision-making behavior by bridging the fields of cognitive psychology, sensorimotor integration, economics, and moral philosophy.

# **Chapter 4**

## **Converging structural and functional connectivity of orbitofrontal, dorsolateral prefrontal, and posterior parietal cortex in the human striatum**

*The following text has been adapted from Jarbo & Verstynen, 2015*

Modification of spatial attention via reinforcement learning (Lee and Shomstein, 2013) requires the integration of reward, attention, and executive processes. Corticostriatal pathways are an ideal neural substrate for this integration because these projections exhibit a globally parallel (Alexander et al., 1986), but locally overlapping (Haber, 2003), topographical organization. Here we explore whether there are unique striatal regions that exhibit convergent anatomical connections from orbitofrontal cortex, dorsolateral prefrontal cortex, and posterior parietal cortex. Deterministic fiber tractography on diffusion spectrum imaging data from neurologically healthy adults ( $N = 60$ ) was used to map frontostriatal and parietostriatal projections. In general, projections from cortex were organized according to both a medial–lateral and a rostral– caudal gradient along the striatal nuclei. Within rostral aspects of the striatum, we identified two bilateral convergence zones (one in the caudate nucleus and another in the putamen) that consisted of voxels with unique projections from orbitofrontal cortex, dorsolateral prefrontal cortex, and parietal regions. The distributed cortical connectivity of these striatal convergence

zones was confirmed with follow-up functional connectivity analysis from resting state fMRI data, in which a high percentage of structurally connected voxels also showed significant functional connectivity. The specificity of this convergent architecture to these regions of the rostral striatum was validated against control analysis of connectivity within the motor putamen. These results delineate a neurologically plausible network of converging corticostriatal projections that may support the integration of reward, executive control, and spatial attention that occurs during spatial reinforcement learning.

#### 4.1 Introduction

It is well known that contextual factors, such as cue/target proximity within the same bounded object, can bias bottom-up visuospatial attention (Posner et al., 1980; Egeth and Yantis, 1997). Recent research has shown that placing a high reward on certain targets can override this intrinsic spatial attention bias (Della Libera and Chelazzi, 2006; Kristjánsson et al., 2010; Lee and Shomstein, 2013, 2014). The abrogating influence of reward feedback on intrinsic spatial attention is consistent with the idea that reinforcement learning (Sutton and Barto, 1998) alters the bottom-up influences of stimulus features on attentional allocation during spatial decision making.

Functionally, reinforcement learning depends on the striatum (Graybiel, 1995; Knutson et al., 2000; Dayan and Abbott, 2001; O'Doherty, 2004; Daw and Doya, 2006). Although many studies focus on the role of the ventral striatum in reinforcement learning (Pagnoni et al., 2002; O'Doherty et al., 2003; McClure et al., 2004; Rodriguez et al., 2006), evidence of dorsomedial caudate involvement in reward-based responses suggests a more global involvement of striatal

systems in behavioral updating (Delgado et al., 2003, 2005; Knutson and Cooper, 2005; Kuhnlen and Knutson, 2005; Lohrenz et al., 2007). This recruitment of distributed striatal systems may reflect an integration of multiple, disparate signals during learning. Indeed, although the striatum is generally viewed as a central integration point of cortical information within strictly closed, but parallel, circuits (Alexander et al., 1986), there is a growing body of evidence for overlap from spatially disparate cortical areas (Haber, 2003; Averbeck et al., 2014). This diffuse overlap of corticostriatal projections has been proposed as an explicit substrate for reinforcement learning that directly integrates reward and executive control signals from the orbitofrontal cortex (OFC) and dorsolateral prefrontal cortex (DLPFC), respectively (for review, see Haber and Knutson, 2010).

Introducing signals from regions that support visuospatial processing into this striatal integration process may be one mechanism by which reinforcement learning can be applied to spatial attention. Visuospatial attention is generally associated with the posterior parietal cortex in humans and nonhuman primates (for review, see Critchely, 1953; Colby and Goldberg, 1999; Silver et al., 2005). Nonhuman primate histology research has shown a topography of parietostriatal connectivity in which posterior parietal projections terminate in distributed clusters along the caudate nucleus, proximal to OFC and DLPFC projection termination sites (Selemon and Goldman-Rakic, 1985, 1988; Cavada and Goldman-Rakic, 1991). This proximity of DLPFC and parietal connectivity has also recently been confirmed functionally in humans (Di Martino et al., 2008; Choi et al., 2012); however, the specific pattern of convergent inputs from parietal, DLPFC, and OFC areas has yet to be confirmed. To this end, we used diffusion spectrum imaging (DSI) and resting state fMRI to explore a neurologically plausible network

of converging projections in the striatum that may support the integration of information from OFC, DLPFC, and posterior parietal areas. The presence of convergent corticostriatal inputs would provide necessary evidence for a structurally and functionally integrative network that underlies mechanisms of spatial reinforcement learning.

## 4.2 Materials & Methods

### 4.2.1 Participants

Sixty participants (28 male, 32 female) were recruited locally from the Pittsburgh, Pennsylvania area as well as the Army Research Laboratory in Aberdeen, Maryland. Participants were neurologically healthy adults with no history of head trauma, neurological or psychological pathology. Participant ages ranged from 18 to 45 years old (mean age, 26.5 years). Informed consent, approved by the Institutional Review Board at Carnegie Mellon University and in compliance with the Declaration of Helsinki, was obtained for all participants. Participants were all financially compensated for their time.

### 4.2.2 MRI acquisition

All 60 participants were scanned at the Scientific Imaging and Brain Research Center at Carnegie Mellon University on a Siemens Verio 3T magnet fitted with a 32-channel head coil. An MPRAGE sequence was used to acquire a high-resolution ( $1 \text{ mm}^3$  isotropic voxels, 176 slices) T1-weighted brain image for all participants. DSI data was acquired following fMRI sequences using a 50 min, 257-direction, twice-refocused spin-echo EPI sequence with multiple q values (TR 11,400 ms, TE 128 ms, voxel size  $2.4 \text{ mm}^3$ , field of view 231x231 mm, b-max

5000 s/mm<sup>2</sup>, 51 slices). Resting state fMRI (rsfMRI) data consisting of 210 T2\*-weighted volumes were collected for each participant with a BOLD contrast with echo planar imaging (EPI) sequence (TR 2000 ms, TE 29 ms, voxel size 3.5 mm<sup>3</sup>, field of view 224x224 mm, flip angle 79 deg). Head motion was minimized during image acquisition with a custom foam padding setup designed to minimize the variance of head motion along the pitch and yaw rotation directions. The setup also included a chin restraint that held the participant's head to the receiving coil itself. Preliminary inspection of EPI images at the imaging center showed that the setup minimized resting head motion to 1 mm maximum deviation for most subjects. Diffusion MRI reconstruction. DSI Studio (<http://dsi-studio.labsolver.org>) was used to process all DSI images using a q-space diffeomorphic reconstruction method (Yeh and Tseng, 2011). A nonlinear spatial normalization approach (Ashburner and Friston, 1999) was implemented through 16 iterations to obtain the spatial mapping function of quantitative anisotropy (QA) values from individual subject diffusion space to the FMRIB 1 mm fractional anisotropy (FA) atlas template. QA is an orientation distribution function (ODF) based index that is scaled with spin density information that permits the removal of isotropic diffusion components from the ODF to filter false peaks, facilitating deterministic fiber tractography resolution. For a detailed description and comparison of QA with standard FA techniques, see Yeh et al. (2013). The ODFs were reconstructed to a spatial resolution of 2 mm<sup>3</sup> with a diffusion sampling length ratio of 1.25. Whole-brain ODF maps of all 60 subjects were averaged to generate a template image of the average tractography space.

#### 4.2.3 Fiber tractography and analysis.

Fiber tractography was performed using an ODF-streamline version of the FACT algorithm (Yeh et al., 2013) in DSI Studio (September 23, 2013 and August 29, 2014 builds). All fiber tractography was initiated from seed positions with random locations within the whole-brain seed mask with random initial fiber orientations. Using a step size of 1 mm, the directional estimates of fiber progression within each voxel were weighted by 80% of the incoming fiber direction and 20% of the previous moving direction. A streamline was terminated when the QA index fell below 0.05 or had a turning angle 75 degrees. Fiber tractography was performed in several stages. First, using the group averaged template brain, we tracked 100,000 streamlines that terminated anywhere within a striatal region of interest mask (ROI). To generate this mask, caudate nucleus and putamen masks from the SRI24 multichannel atlas (Rohlfing et al., 2010) were merged and then expanded by one voxel (2 mm) in all directions. This tractography experiment was performed to visualize the gradients of connectivity within the striatum (see Topography of corticostriatal projections).

After this analysis, we performed ROI-based tractography to isolate streamlines between pairs of ipsilateral cortical and striatal masks. All cortical masks were selected from the SRI24 multichannel atlas. Diffusion-based tractography has been shown to exhibit a strong medial bias (Croxson et al., 2005) due to partial volume effects and poor resolution of complex fiber crossings (Jones and Cercignani, 2010). To counter the bias away from more lateral cortical regions, tractography was generated for each cortical surface mask separately. Twenty-six cortical surface masks (13 per hemisphere) in the frontal and parietal lobes were selected from the SRI24 multichannel atlas as targets for corticostriatal tractography, including: gyrus rectus

(Rectus); ventromedial prefrontal cortex (Frontal\_Med\_Orb); opercular, orbital, and triangular parts of the inferior frontal gyrus (Frontal\_Inf\_Oper, Frontal\_Inf\_Orb, Frontal\_Inf\_Tri); dorsal and orbital middle and superior frontal gyri (Frontal\_Mid, Frontal\_Mid\_Orb, Frontal\_Sup, Frontal\_Sup\_Orb); superior and inferior parietal lobules (Parietal\_Sup, Parietal\_Inf); angular gyrus (Angular) and supramarginal gyrus (SupraMarginal). The same striatal ROI mask was used as in the first tractography run. The QA threshold was set to 0.04 for tracking streamlines from the dorsal middle frontal gyri (Frontal\_Mid) due to detection of significantly fewer corticostriatal projections than expected (Verstynen et al., 2012). Each cortical surface ROI mask was paired with an ipsilateral striatum ROI mask, which were both designated as ends in DSI Studio, and whole-brain seeded tractography continued for 3 108 seeds (3000 samples per voxel in the whole-brain mask). To be included in the final dataset, streamlines had to (1) have a length 120 mm and (2) terminate in the cortical surface mask at one end and within the ipsilateral striatum mask at the other. All cortical surface ROI masks were also paired with the contralateral striatum masks. Streamlines were generated for all datasets using the same tracking parameters previously described and a maximum length constraint of 180 mm to capture longer interhemispheric projections.

Then, to facilitate further analyses, streamlines from the ROI pairings in each hemisphere were combined into three meta-regions. The OFC meta-region was comprised of streamlines from medial and lateral OFC, including: gyrus rectus (Rectus), the orbital part of the inferior frontal gyrus (Frontal\_Inf\_Orb) and middle (Frontal\_Mid\_Orb) and superior frontal (Frontal\_Sup\_Orb) gyri. The DLPFC meta-region consisted of streamlines from opercular

(Frontal\_Inf\_Oper) and triangular (Frontal\_Inf\_Tri) parts of the inferior frontal gyrus, as well as middle (Frontal\_Mid) and superior frontal (Frontal\_Sup) gyri. Streamlines from the superior (Parietal\_Sup) and inferior parietal lobules (Parietal\_Inf), angular gyrus (Angular), and supramarginal gyrus (SupraMarginal) constituted the parietal meta-region. For a more complete assessment of the cortical and striatal topographic organization of the endpoint distributions of the OFC, DLPFC and parietal meta-regions were reconstructed.

To confirm the pattern of connectivity observed through the constrained ROI-based approach, a final tractography (see Figure 4.4) analysis was performed by reseeding from a whole-brain mask with each convergence zone designated as an end. This was repeated separately for all four convergence zone masks across all 60 datasets. Tracking proceeded until a total of 50,000 fibers were detected, rather than 310 8 seeds.

Approximate motor projections into the striatum were used as a control pathway. These were estimated using the precentral gyrus (Precentral) masks from the SRI24 multichannel atlas. The precentral gyrus masks were designated as endpoint masks paired with ipsilateral and contralateral striatum masks for tracking streamlines using the same parameters described above, across all individual datasets. A single cluster of contiguous voxels was isolated from each putamen in all datasets to create mean striatal precentral clusters.

#### 4.2.4 Striatal and cortical endpoint distribution analysis.

The primary tractography variable of interest was the distribution of streamline endpoints.

We looked at these endpoints in two separate ways. First, to capture the major gradients of corticostriatal pathway organization, we labeled each of the 100,000 streamlines from the first tractography run based on the position of its endpoint within the striatum mask according to two gradients: medial–lateral (x position) and rostral–caudal (y position). Each streamline was then color-coded according to its position in each gradient separately and visualized at the whole brain level (see Figure 4.1).

Next, we looked at the distribution of densities of endpoints, across datasets, within each voxel at the subcortical and cortical levels. Custom MATLAB functions were used to generate four striatal endpoint density maps (i.e., convergence zones; see Figs. 4.3 and 4.4) where all cortical metaregions yielded overlapping projections within ipsilateral striatum. First, the 3D coordinates of the streamline projection endpoints from each meta-region in the caudate nucleus and putamen within each hemisphere were extracted. To obtain matrices of striatal endpoint coordinates for each meta-region for all datasets, a mask for each caudate nucleus and putamen were loaded separately into MATLAB with streamlines from each ipsilateral cortical region. A one-sample t test was used to calculate maps of endpoint densities for each set of streamlines from the individual density maps. Significance was calculated with an FDR-corrected threshold ( $q$ ) 0.05 to identify striatal voxels with projection endpoints from each meta-region that were consistent across all datasets.

Striatal endpoints were then extracted and saved as a new mask, resulting in a three-way convergence zone representing the total volume of contiguous voxels (cluster size  $k = 20$ ) within each nucleus where termination points of projections from the OFC, DLPFC, and parietal metaregions were detected. This was done for both caudate nuclei and putamen, resulting in four

(left caudate, left putamen, right caudate, and right putamen) convergence zone masks. Convergence zone masks for each nucleus were then used to calculate maps of the mean convergence zone as well as to assess the consistency and significance of convergence zone volumes across all 60 datasets. The significance at each convergence zone was calculated using a one-sample t test with a  $\alpha = 0.05$ . For comparison, two-way pairwise convergence zones masks (i.e., OFC + DLPFC, DLPFC + Parietal, and Parietal + OFC) were also created in the same fashion as the three-way convergence zones masks.

After the convergence zones were isolated, cortical endpoint coordinates were extracted from the reseeded tracking described in Section 4.2.3. Streamlines between each convergence zone and the whole-brain seed across all datasets were loaded into MATLAB, and the endpoints were saved as masks. A one-sample t test was conducted to identify significant voxels throughout the brain that had consistent structural connectivity with each of the convergence zones.

#### 4.2.5 Resting state fMRI preprocessing and analyses.

SPM8 (Wellcome Department of Imaging Neuroscience, London) was used to preprocess all rsfMRI collected from 55 of the 60 participants with DSI data. To estimate the normalization transformation for each EPI image, the mean EPI image was first selected as a source image and weighted by its mean across all volumes. Then, an MNI-space EPI template supplied with SPM was selected as the target image for normalization. The source image smoothing kernel was set to a FWHM of 4 mm, and all other estimation options were kept at the SPM8 defaults to

generate a transformation matrix that was applied to each volume of the individual source images for further analyses.

The convergence zones and striatal precentral clusters obtained from the tractography analyses were used as seed points for the functional connectivity analysis. A series of custom MATLAB functions were used to do the following: (1) extract the voxel time series of activity for each convergence zone, (2) remove estimated noise from the time series by selecting the first five principal components from the SRI24 tissues white matter and CSF masks, and (3) calculate t and p values of consistent activity with corresponding significance. rsfMRI data were analyzed using AFNI (Cox, 1996) to calculate functional activity throughout the brain correlated with each convergence zone and striatal precentral cluster seed in accordance with previously used methods (Choi et al., 2012). Specifically, functional activity correlations ( $r$ ) were converted to Z-scores using Fisher's r-to-Z transformation for each convergence zone and striatal precentral cluster across all 55 datasets.

First, a convergence zone or striatal precentral cluster mask was loaded into MATLAB 8.1/R2013a (MathWorks) with an individual participant's rsfMRI time series data. The time series of activity corresponding with the volume of the mask was extracted, yielding activity values for each voxel in the mask across all 210 volumes of the rsfMRI BOLD EPI sequence. Next, the time series was denoised by regressing the first five principal components of estimated noise from the white matter and CSF voxels out of the total time series activity. Once denoised, the data were smoothed with a Gaussian kernel (FWHM 2 mm) and a one-sample t

test was run to identify consistent, significant functional activity correlated with the time series across all 55 datasets. Corresponding FDR-corrected values of  $q < 0.05$  were also calculated to create maps of significant functional activity for each convergence zone and striatal precentral cluster mask (see Figure 4.5).

#### 4.2.6 Structural and functional connectivity overlap analysis

Using a custom MATLAB function, t-maps of consistent structural connectivity from the DSI data, and Z-transformed correlation ( $r$ ) maps from the fMRI data were used to calculate the percentage of structurally significant voxels (i.e., a cortical voxel that had significant structural connectivity with a striatal convergence zone) that were also functionally significant. For this, the DSI t-map data were thresholded at  $q < 0.05$  to yield all significant voxels with structural connections that were consistent across all 60 DSI datasets. Corresponding rsfMRI data were also thresholded at  $q < 0.05$ , resulting in maps of voxels with significant functional connectivity across all 55 fMRI datasets. For each convergence zone, t-maps and Z-maps of structural and functional connectivity, respectively, were loaded into MATLAB. A voxel was considered to have significant structural or functional connectivity if the one-sample t test to find consistent connections across all DSI or rsfMRI datasets resulted in a significant  $q$  value. The maps of significant structural and functional connectivity for each convergence zone were binarized such that all voxels with a  $q < 0.05$  were set to 1, and all other voxels were set to 0. After transforming the binary data into single-column vectors, the dot product of significant structural and functional voxels was summed and divided by the number of significant structural voxels. This calculation

yielded the percentage of cortical voxels that had significant structural and functional connectivity with a striatal convergence zone, aggregated across all voxels within a given zone.

Finally, a permutation test was conducted to determine the chance levels of overlap between the structural and functional measures of connectivity. For each convergence zone, a random permutation of the resulting binary data vector of significant functional voxels was generated, and the percentage overlap with the significant structural voxels was recalculated. This process was repeated for 1000 iterations for each convergence zone ROI to construct the 95% confidence interval of chance overlap between structural and functional connectivity (i.e., to construct the null distribution of structurally connected voxels to the convergence zone that randomly overlapped with functionally connected voxels).

## 4.3 Results

### 4.3.1 Topography of corticostriatal projections

We first set out to characterize the major topographic gradients of the corticostriatal pathways. Whereas previous animal work using viral tracers (Kemp and Powell, 1970; Selemon and Goldman-Rakic, 1985; Haber, 2003; Utter and Basso, 2008) shows a primarily medial–lateral organization of corticostriatal projections, recent human imaging work suggests a second rostral-to-caudal organization of these pathways (Draganski et al., 2008; Badre and Frank, 2012; Verstynen et al., 2012; Verstynen, 2014). Here, we evaluate the global structural connectivity of the left and right striatum, respectively, on the average template brain. The streamlines are coded according to their position along either a medial–lateral axis (Figure 4.1a-f) or rostral–caudal axis (Figure 4.1g-l). Along the medial–lateral axis, we find a gross parcellation between

caudate and putamen fibers, with the former receiving projections from rostral prefrontal and OFC, medial wall areas, and dorsal parietal regions, and the latter receiving projections primarily from somatosensory, primary motor, premotor, and caudal prefrontal areas. Within these major nuclear segmentations, there is a somewhat consistent medial–lateral organization such that more medial areas of cortex project to more medial regions in the subcortical nuclei (Figure 4.1a-f, cooler colors), and more lateral areas of cortex project to more lateral striatal regions (Figure 4.1a-f, warmer colors). For example, medial orbitofrontal and ventromedial prefrontal areas project to more medial caudate regions (dark blue) than lateral orbitofrontal cortical streamlines (light blue) (see Figure 4.1c and d). This is largely consistent with previously reported dichotomies of caudate and putamen projections (Alexander et al., 1986) and suggests that, at the gross macroscopic level of major cortical regions, the primary gradient of organization is in a medial-to-lateral plane.

The global medial-to-lateral gradient across striatal nuclei is consistent with previous animal imaging studies; however, there is a strong local rostral–caudal organization within the nuclei themselves. Qualitative inspection of Figure 4.1g-l reveals a rostral–caudal gradient that appears to be isolated within major functionally defined regions. For example, within the lateral prefrontal cortex, which generally projects to the putamen (Figure 4.1a-d), more rostral regions of cortex tend to terminate in more rostral ends of the striatum. However, even this gradient along the sagittal plane segregates some major cortical regions. Motor and somatosensory areas tend to terminate in more caudal regions of the striatum (Figure 4.1g-l, warmer colors), whereas prefrontal and orbitofrontal areas terminate in more rostral regions of the striatum (Figure 4.1g-l, cooler colors). More interestingly, however, parietal projections extend to the more rostral part of

the striatum near the location of lateral frontal projection. This is largely consistent with previous animal tracer studies (Selemon and Goldman-Rakic, 1988; Cavada and Goldman-Rakic, 1991) and inconsistent with a pure, global rostral–caudal organization of corticostriatal systems (for review, see Utter and Basso, 2008).

These results show that two strong organizational gradients exist in corticostriatal pathways. First, there is a strong macroscopic gradient in a medial–lateral orientation that segregates major functional cortical regions and is moderately driven by spatial proximity. For example, lateral motor areas terminate in the lateral striatal nucleus (i.e., the putamen) and medial motor areas terminate in the more medial nucleus (i.e., the caudate; see Figure 4.1d). Second, there is a more local gradient in a rostral–caudal direction that is not driven by pure spatial proximity but appears to reflect local convergence of inputs from disparate cortical regions. An interesting break of this pure rostral–caudal gradient, however, is the observation that parietal streamlines (Figure 4.1g–l, cyan and light green streamlines) project to rostral portions of the striatum in similar regions as prefrontal and orbitofrontal areas. The location of these parietal projections within both gradients of organization is consistent with parietal inputs converging in similar areas of the striatum as frontal cortex.

To determine the gross topographic organization across the three major ROIs for this study, we examined the common regions of endpoint densities in the striatum for all 60 DSI datasets. Thirteen cortical ROIs were tracked and then collapsed into three meta-region maps: OFC, DLPFC, and parietal cortex (for more details, see Fiber tractography and analysis). Figure 2 shows the endpoint fields for each meta-region cluster. As expected, the endpoint clusters of projections from the three meta-regions exhibit similar topographical distributions as what is

shown in the gradient analysis in Figure 1. Specifically, OFC (yellow) areas project most heavily in the most anterior and medial aspects of the striatum, primarily in the caudate nucleus (Figure 4.2a). DLPFC (Figure 4.2b, blue) regions most consistently project just caudal to the OFC clusters and more laterally, although with some visible overlap between the two clusters. Finally, parietal regions (Figure 4.2c, violet) most densely project to areas slightly more caudal than the DLPFC projections, with a bias toward slightly more lateral striatal regions. This rich, topographical organization of cortical projection endpoints along the striatum demarcates a distinct spatial segmentation of cortical inputs while also providing evidence of some local overlap of corticostriatal projections from adjacent cortical networks.

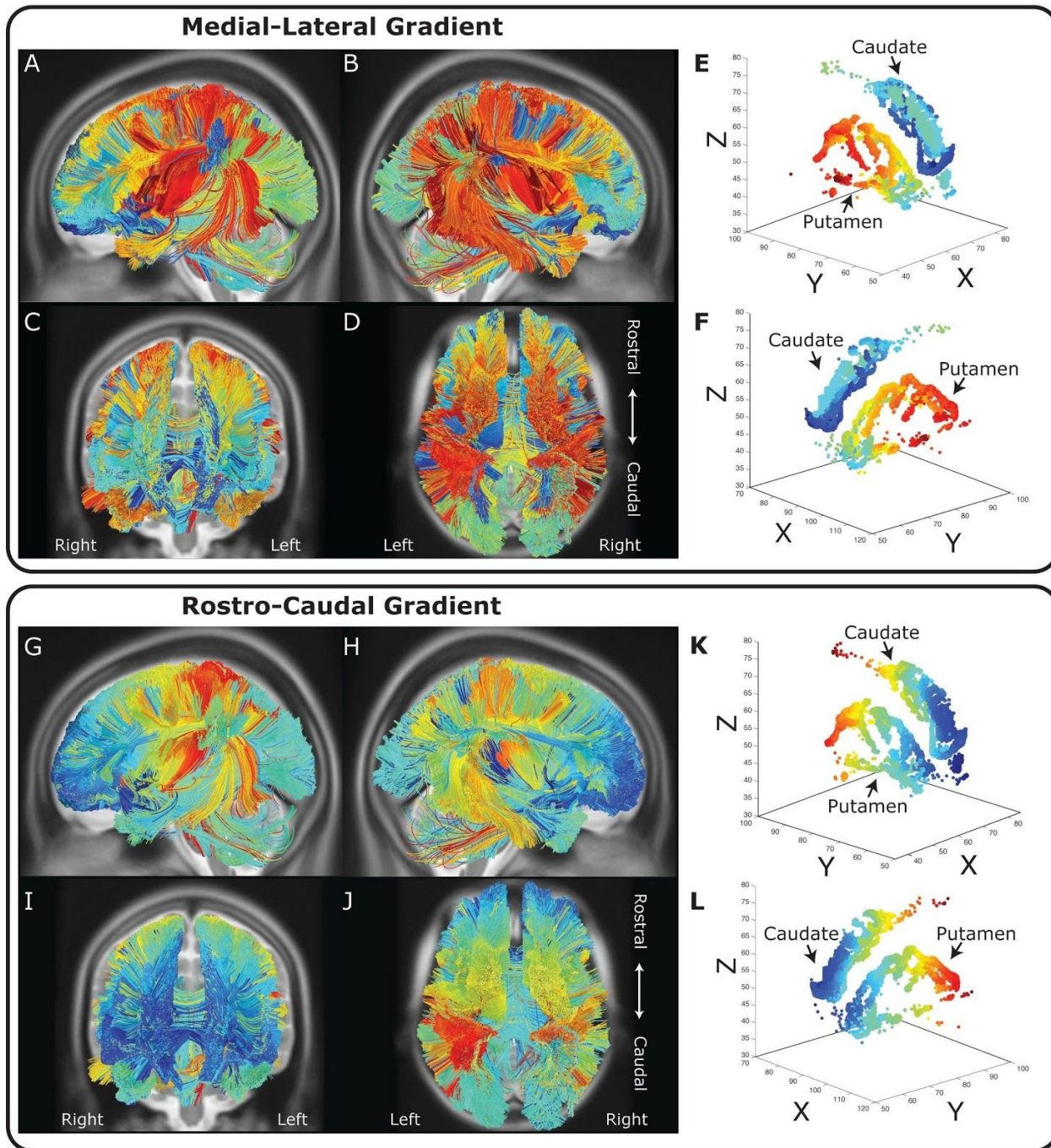


**Figure 4.1** Tractography analysis of medial–lateral (A–F) and rostral–caudal (G–L) striatal topography in the average participant template brain. Streamlines were tracked from whole-brain seeds to caudate and putamen masks. A–F) Cooler colors represent streamlines that terminate more medially, whereas warmer colors represent those that terminate more laterally. Along medial–lateral orientation, spatially proximal cortical areas project to similar locations within the striatum. G–L) Cooler colors represent

streamlines that terminate in more rostral areas, whereas warmer colors represent streamlines that terminate in more caudal striatal areas.

#### 4.3.2 Convergence of corticostriatal projections

Close inspection of Figure 4.2 reveals several common regions with apparent overlapping projections from OFC, DLPFC, and parietal cortical areas. To quantify these overlapping projections, we used a conjunction analysis to identify voxels with significant endpoint densities from OFC, DLPFC, and parietal masks (see Materials and Methods). Clusters of these conjunction voxels ( $k \geq 20$ ) were isolated bilaterally within the caudate nucleus and putamen separately and were consistent across all 60 datasets (all  $t(59)$  values  $2.75$ ,  $q < 0.05$ ). Each nucleus contains a distinct cluster of these convergent fields that appear to be relatively symmetric across hemispheres (Figure 4.3a, left column, b). In the caudate, the convergence zones are isolated along the rostral portion of the body of the caudate. In the putamen, the convergence zones are found on the dorsal and rostral aspects of the nucleus.

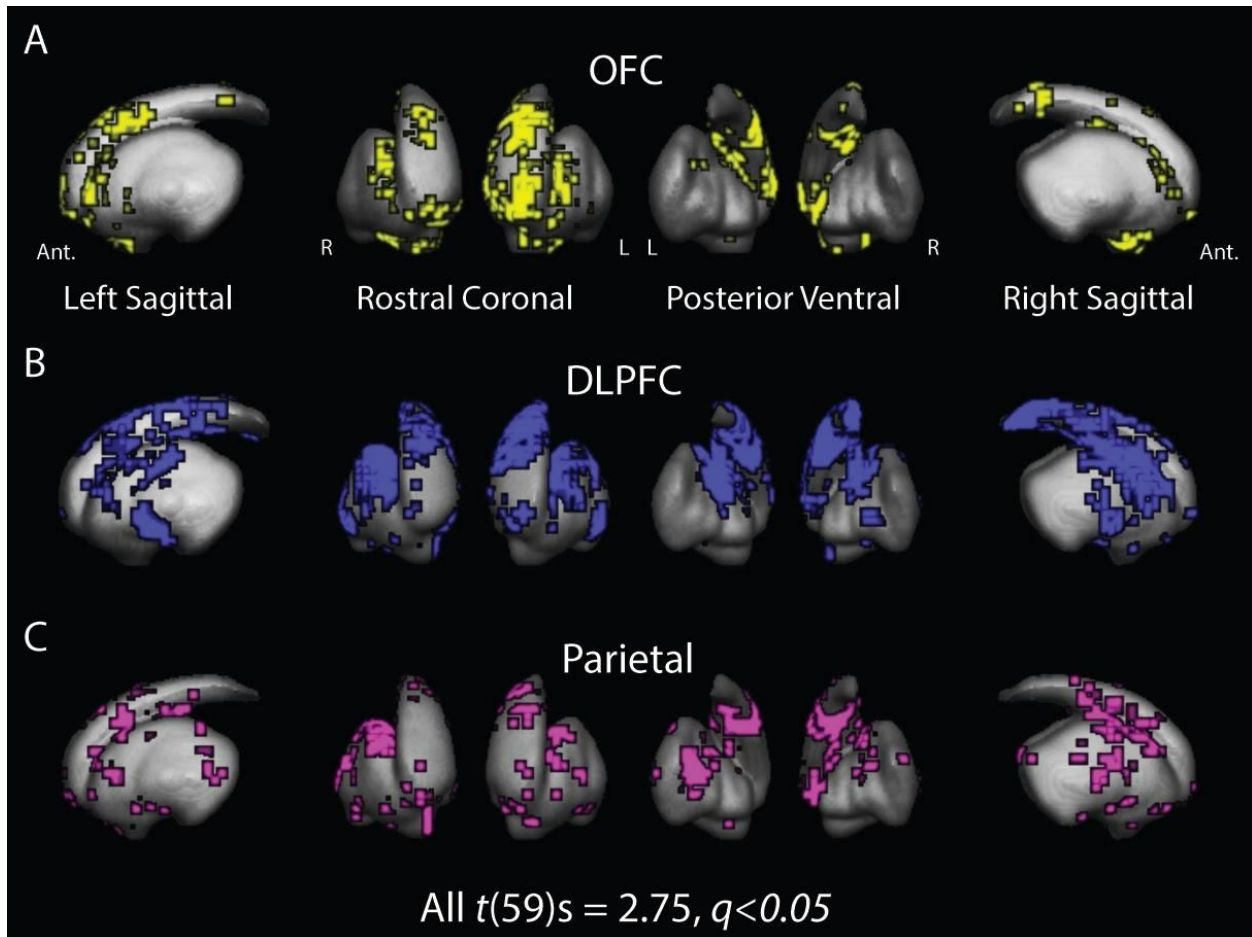


**Figure 4.2** Group statistical maps of common endpoint locations from three cortical meta-regions: OFC (A, yellow), DLPFC (B, blue), and parietal cortex (C, violet). Voxels indicate regions with significant endpoint densities from cortex determined using a one-sample t test and corrected for multiple comparisons.

These three-way convergence zones are smaller than any of pairwise convergence zones between OFC, DLPFC, and parietal cortex. In general, pairwise overlaps with DLPFC are widespread and found across large portions the rostral striatum (Figure 4.3a, second and third columns). The pairwise overlap of OFC and parietal projections is much smaller (Figure 4.3a, fourth column), suggesting that the three-way convergence zones are restricted by the limited overlap of parietal and orbitofrontal connections within the striatum.

It is important to note that the parietal and OFC overlap areas are away from ventral striatal regions that are typically thought of as the main termini of OFC projections (Haber, 2003). For reference, we also mapped the projections from the precentral gyrus as a proxy for the motor inputs into the striatum, which typically terminate in the caudal putamen (Figure 4.3a, right column). In all cases, the striatal areas with convergent projections from OFC, DLPFC, and parietal areas are much more rostral than areas that receive projections from precentral motor areas (i.e., the motor striatum).

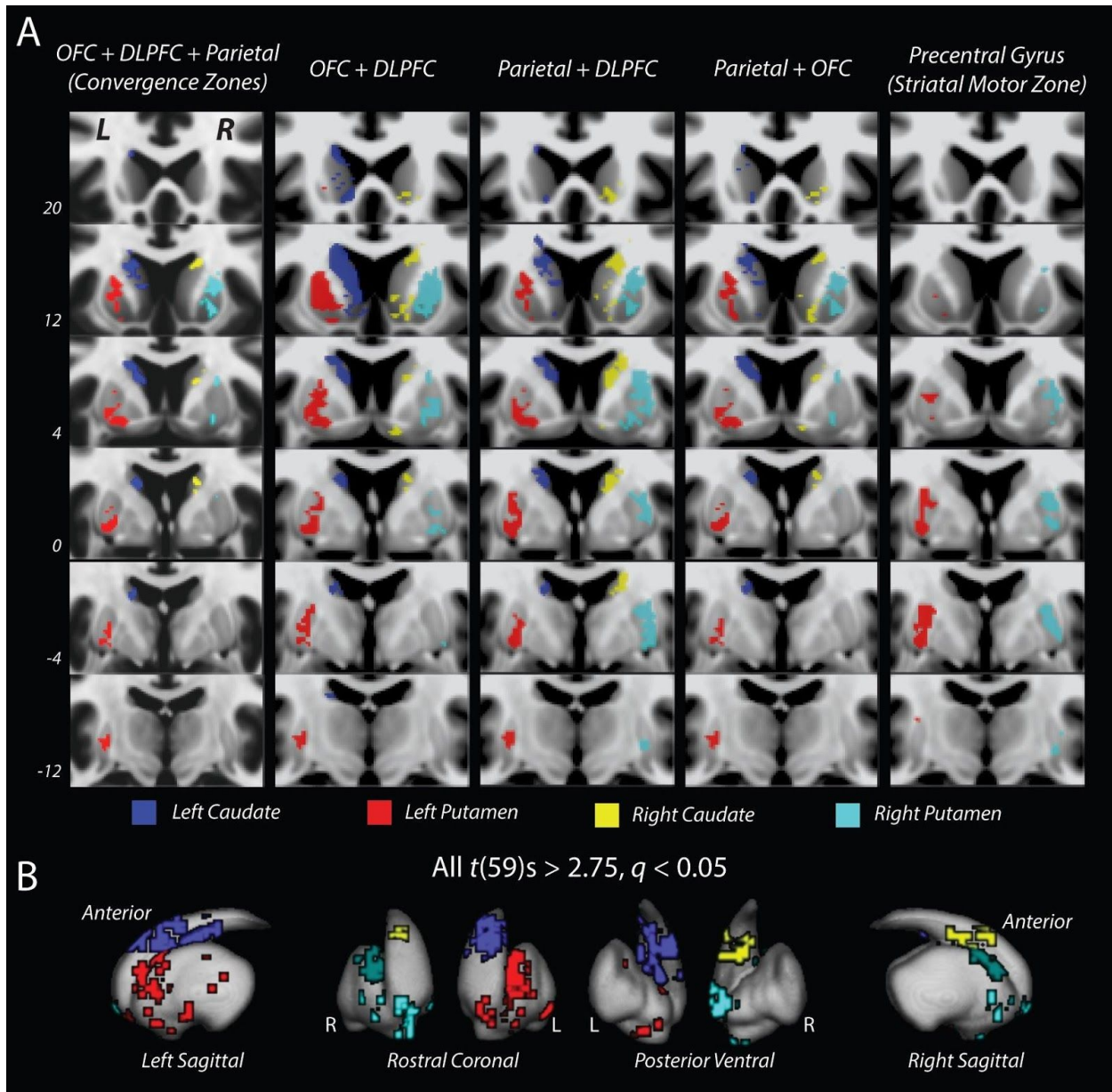


**Figure 4.3** Coronal slice images and 3D representations of mean convergence and nonconvergence zone masks within bilateral caudate nucleus and putamen. A) Coronal slice view of three-way (left column) and two-way (middle three columns) convergence zone, and striatal motor (right column) nonconvergence zone masks on T1-weighted MNI-space brain. Three-way and two-way convergence zones (four left columns) were isolated in both striatal nuclei bilaterally: blue represents left caudate; red represents left putamen; yellow represents right caudate; cyan represents right putamen. Nonconvergence zones (right column) are restricted to regions of putamen (left, red; right, cyan) that received projections from ipsilateral precentral gyrus. All striatal masks consist of single clusters of significant (all  $t(59)$  values  $> 2.75$ , FDR-corrected  $q < 0.05$ )

contiguous voxels (cluster size  $k < 20$ ) with streamline endpoints from the cortical areas indicated above each column. Three-way convergence zones are smaller in volume than two-way convergence zones and are located more rostrally in striatal nuclei than nonconvergence zones. B) 3D surface visualizations of three-way convergence zones.

To get a more complete picture of where the projections into the striatal convergence zones originate along the cortical surface, we performed a second whole-brain tractography analysis, isolating only streamlines that ended in each of the three-way convergence clusters shown in Figure 4.3b. Although the medial bias of the tractography process is somewhat apparent in this second analysis, we still observed significant structural connectivity from lateral prefrontal and parietal regions. Generally, both putamen convergence zones show more distributed projections (Figure 4.4: left, red; right, cyan) than the caudate convergence zones projections (Figure 4.4b: left, blue; right, yellow). The cortical connectivity parietal regions than the caudate connectivity. Within OFC, there are two regions with consistent structural connectivity to the convergence zones. The first is a region along the medial wall that connects largely to the putamen convergence zone. The second is a region on the far lateral borders of the OFC, near the border between Brodmann's areas 11 and 47, that shows consistent connectivity to both the caudate and putamen convergence zones.

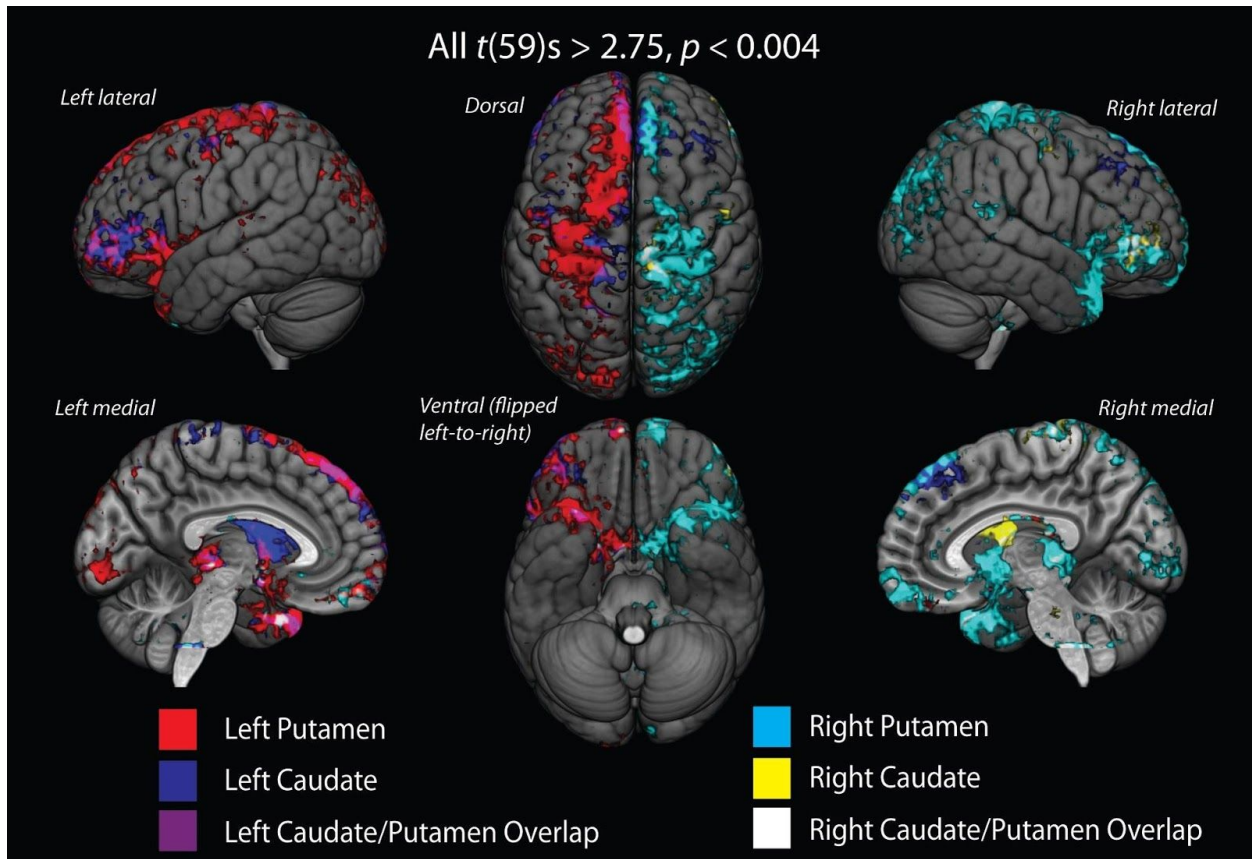


**Figure 4.4** Cortical endpoint density maps of tractography into each convergence zone mask on template brain. Streamlines were tracked from a whole-brain seed to individual three-way convergence zone masks. Maps show cortical and subcortical regions with consistent (all  $t(59)$  values  $> 2.75$ , uncorrected  $p < 0.004$ ) endpoint projections into each convergence zone across all subjects: blue represents left caudate; red represents left putamen; yellow represents right caudate; cyan represents right putamen. Connections with the putamen convergence zone originate from a much larger and more distributed set of cortical areas than those with caudate convergence zone. Overlapping structural connectivity from ipsilateral caudate and putamen convergence zones in OFC, DLPFC, and parietal cortex areas between is shown as purple in the left hemisphere and white in the right hemisphere.

Within the prefrontal cortex, there are two major clusters of connectivity. The first is a cluster on the rostral middle frontal gyrus, approximately at Brodmann's areas 46 and 47, that appears to be contiguous with the lateral OFC clusters and shows a high degree of connectivity

with both the caudate and putamen convergence zones. The second, prefrontal cluster rests along the superior frontal gyrus and reflects primarily inputs to the putamen, although a smaller cluster of voxels sends overlapping projections to the caudate. Finally, most projections to the convergence zones from the parietal cortex appear to originate from regions along the angular gyrus and inferior parietal lobule, whereas some connections within the intraparietal sulcus itself appear to reflect the location of the connections into the caudate convergence zone cluster.

Along with connectivity to our three major ROIs, there is strong connectivity to sensorimotor regions around the precentral sulcus. This is primarily for projections to the putamen convergence zone, although some medial cortical areas show consistent projections to the caudate zone as well. Thus, consistent with the striatal maps in Figure 3A, some sensorimotor regions may also project into rostral portions of the striatal convergence zones, particularly along the putamen. Our original tractography identifying the convergence zones is restricted to ipsilateral corticostriatal projections; however, the reseeded tractography analysis from the left caudate shows several notable interhemispheric connections, particularly with dorsal and medial superior frontal gyrus in the right hemisphere.

Contralateral connectivity between left caudate convergence zone and right dorsolateral prefrontal areas is indeed consistent with nonhuman primate histology (McGuire et al., 1991) and human diffusion imaging work (Lehéricy et al., 2004). No such interhemispheric connectivity is observed from the convergence zone in the right caudate nucleus. However, the lack of strong interhemispheric structural connections may be limited by our initial tractography approach. To correct for this, we conducted a follow-up tractography analysis between convergence zones in one hemisphere and cortical areas in the contralateral hemisphere (Section

4.2.3). After adjusting for multiple comparisons ( $q < 0.05$ ), we did not observe any significant convergence zones from contralateral cortical areas. This null result highlights a limitation of diffusion-weighted imaging approaches for tracking contralateral corticostriatal projections previously reported using histological approaches (Selemon and Goldman-Rakic, 1985; Cavada and Goldman-Rakic, 1989a, 1991).

#### 4.3.3 Functional connectivity of convergence zones

So far, our tractography analysis has revealed converging anatomical projections from orbitofrontal, prefrontal, and posterior parietal areas into the striatum. If these do, indeed, reflect an integrative functional network, then cortical areas that show a high degree of anatomical connectivity to the convergence zones should also show significant functional connectivity to these same striatal regions. To this end, we used rsfMRI data to measure the functional connectivity between cortical areas and each of the striatal convergence zones. The functional activity of striatal convergence zones is correlated with a distributed set of bilateral cortical areas, including the DLPFC, both medial and lateral OFC, sensorimotor areas, and, most importantly, posterior parietal regions (Figure 4.5). Within the OFC, we again see that medial regions are more highly connected to the putamen cluster than the caudate cluster, although the functional connectivity appears to be centered in more caudal regions than the location of structural endpoints. The lateral OFC regions, on the border of approximately Brodmann's areas 11 and 47, also show connectivity to both convergence zone clusters. This pattern is highly similar to what was observed in the structural connectivity analysis, albeit with a much more distributed cortical representation.

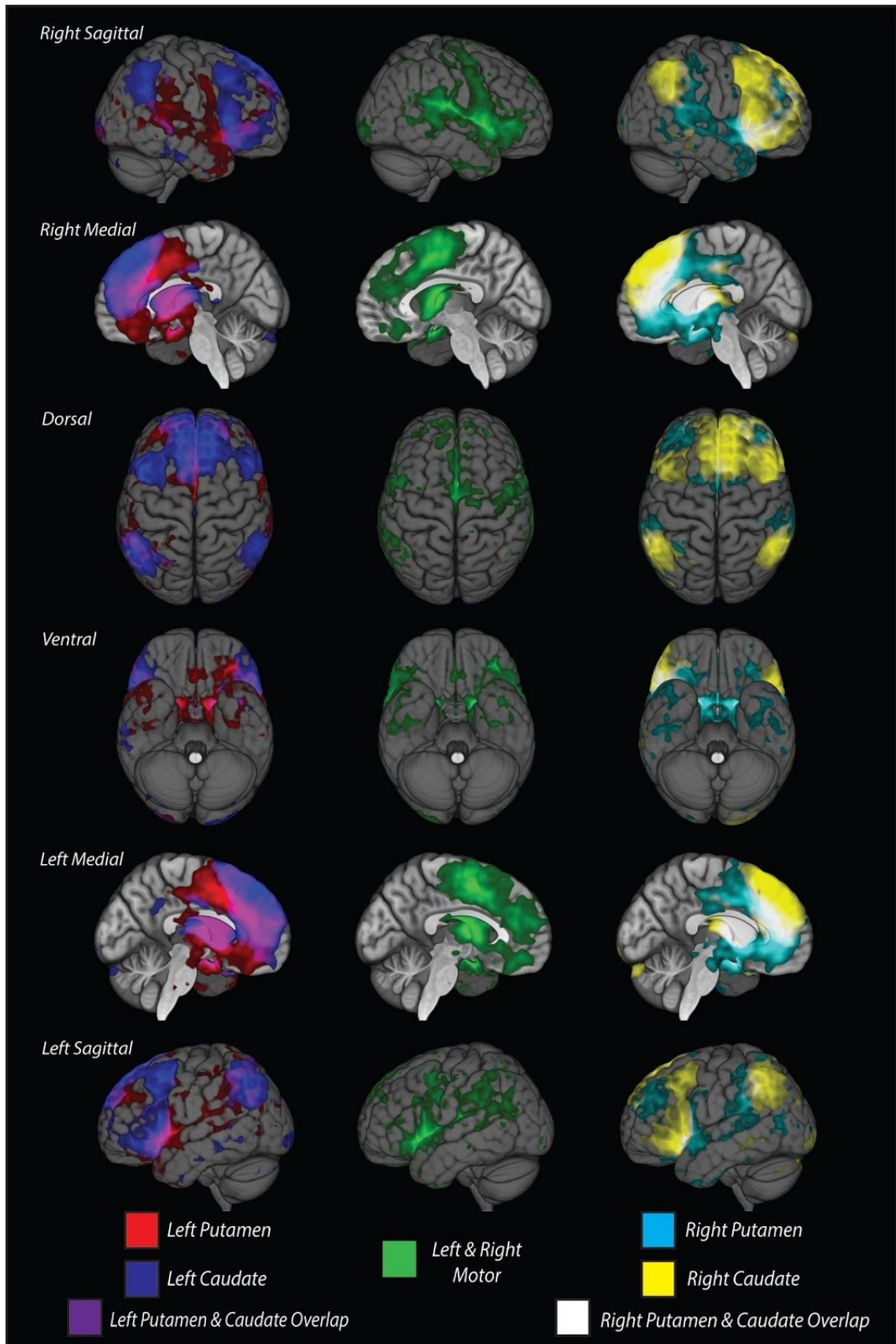


**Figure 4.5** Resting state fMRI maps of functional connectivity of convergence and nonconvergence zones with the whole brain after adjusting for multiple comparisons. Correlations from individual resting state datasets ( $N=55$ ) were normalized using Fisher's r-to-Z transformation, and group maps were calculated using a one-sample t test with an FDR-corrected  $q$  value  $< 0.05$ . Both caudate convergence zone maps were thresholded at  $Z(r) = 0.03 - 0.10$ , and putamen convergence and nonconvergence zone maps were thresholded at  $Z(r) = 0.05 - 0.10$ . Overlaid cortical activity patterns show correlated functional connectivity with the left (left column; blue represents caudate; red represents putamen) and right (right column; yellow represents caudate; cyan represents putamen) convergence zones and bilateral nonconvergence zones in striatal motor regions of the putamen (middle column; green) separately. Significant functional connectivity of ipsilateral caudate and putamen convergence zones overlap in OFC, DLPFC, and parietal areas laterally, and in anterior cingulate cortex medially. Nonconvergence zone functional connectivity is primarily restricted to precentral gyrus and insular cortex laterally, and some anterior cingulate cortex and caudal superior frontal gyrus medially.

In most frontal areas, convergence zones from both nuclei exhibit a similar pattern of functional associations throughout the cortex, particularly in the rostral aspects of the DLPFC, lateral OFC, and anterior cingulate cortex. However, there is also a moderate degree of specificity between the convergence zones on each striatal nucleus. For example, several bilateral cortical regions, including the middle frontal gyrus and medial superior frontal gyrus, show functional connectivity with only the caudate convergence zones. In contrast, aspects of the precentral gyrus, subgenual cingulate, and caudal aspects of the supplementary motor area show unique bilateral connectivity with the convergence zones in the putamen. Functional connectivity with the parietal cortex is restricted along dorsal aspects of the intraparietal sulcus and portions of the inferior parietal lobule. In this case, connectivity to the caudate convergence zone appears to reside in more caudal parietal regions, whereas connectivity to the putamen convergence zone resides in more rostral parietal areas. These regions of unique functional connectivity, along with the unique cortical regions identified in the structural connectivity analysis in Figure 4, suggest

that the convergence zones in the caudate nucleus and the putamen may reflect dissociable networks for integrating information from frontoparietal networks.

Because the striatal nuclei receive some of the most convergent inputs in the brain (Selemon and Goldman-Rakic, 1985), it is possible that the distributed patterns of functional connectivity that we found to the striatal convergence zones are not unique, but that any striatal area will show a broad and distributed connectivity to many neocortical areas. To address this, we included an additional control analysis looking at the functional connectivity to the motor putamen clusters shown in Figure 4.3a (right column). The group-level functional connectivity to the motor putamen is shown in the middle column of Figure 5. As would be expected (Choi et al., 2012), functional connectivity from the cortex to the motor putamen is quite different from that in the convergence zones. There is a much larger representation along the precentral gyrus and central sulcus. Although there is a large cluster of connectivity along the medial wall, this cluster is centered much more caudally than the clusters connected to the convergence zones. Some areas do show overlap with the areas that also project to the striatal convergence zones, particularly along the inferior frontal gyrus, which is thought to contain the ventral premotor cortex (Rizzolatti et al., 1996), as well as some ventral medial wall and ventral parietal areas. However, despite these regions of overlap, the connectivity patterns of the motor putamen demonstrate that the frontoparietal connectivity found in the convergence zones is not a ubiquitous feature of corticostriatal connections.

#### 4.3.4 Structure–function overlap

Comparing the maps in Figures 4.4 and 4.5 reveals qualitative similarities in the patterns of structural and functional connectivity to the striatal convergence zones. To better understand the similarity between these two connectivity estimates, these maps are plotted together on an inflated brain surface (Figures 4.6 and 4.7). Given the relative symmetry of the connectivity patterns between hemispheres, here we will focus on descriptions of ipsilateral connections in the left hemisphere.

On the ventral surface, functional and structural connectivity to the caudate convergence zone overlaps in the same rostral areas of lateral orbital gyrus and ventrolateral inferior frontal gyrus (Figure 4.6, left panels). However, positive functional connectivity is adjacent to clusters of structural connections in the inferior frontal gyrus and extends caudally to regions that correspond approximately with ventral aspects of Brodmann's area 44 and 45. Functional connectivity to the caudate convergence zone also overlaps with clusters of structural connectivity in caudal regions of the orbital gyrus that extend from inferior frontal gyrus to the medial wall. This functional connectivity appears to be restricted to the same lateral orbital gyrus regions where clusters of structural connections are also present.

Ventral connectivity to the putamen convergence zone shows clusters of structural and functional connections in rostral lateral OFC that extend caudally along the ventral inferior frontal gyrus (Figure 4.6, top right). Unlike connections to the caudate convergence zone, structural and functional connections overlap in more central OFC regions as well as throughout ventral aspects of the insula (Figure 4.6, bottom right). Furthermore, large clusters of structural and functional connections to the putamen convergence zone are present along the gyrus rectus. Although a

much larger swatch of functional connectivity is observed throughout much of the orbital gyrus until the approximate border between medial orbital gyrus and gyrus rectus (Figure 4.6, bottom right), these functional clusters appear to subsume the clusters of structural connections to the putamen convergence zone.

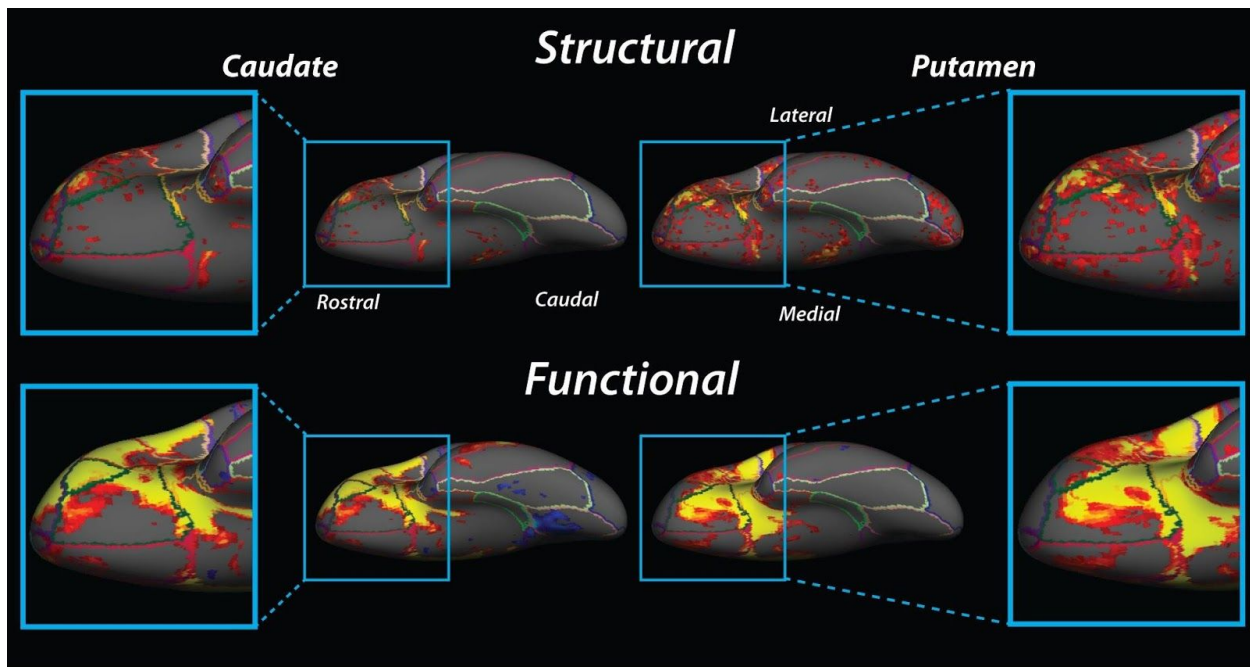


**Figure 4.6** Ventral surface maps of structural and functional convergence zone connectivity in OFC on an inflated brain. Clusters of significant (all  $t$  values  $> 2.75$ , uncorrected  $p < 0.05$ ) structural and functional connectivity are observed to overlap throughout OFC. Warmer colors represent  $t < 2.75$ ; cooler colors represent  $t < -2.75$ . Left panels, Connectivity to the caudate convergence zone. Right panels, Connectivity to the putamen convergence zone.

At the lateral surface, there is a high degree of overlap between structural and functional connections to the caudate convergence zone (Figure 4.7). In DLPFC regions, clusters of structural connections extend caudally from the frontal pole to encompass the rostral two-thirds

of the inferior frontal gyrus. Clusters of structural connections are also present along the full extent of the middle frontal gyrus (Figure 4.7a, top left). This spattering of structural connections to the caudate convergence zone overlap with clusters of strong positive functional connectivity in the DLPFC as well (Figure 4.7a, bottom left). In particular, functional connections extend caudally from the frontal pole along the entire inferior frontal gyrus and the rostral third and caudal half of the middle frontal gyrus, overlapping with many of the regions that also show strong structural connections.

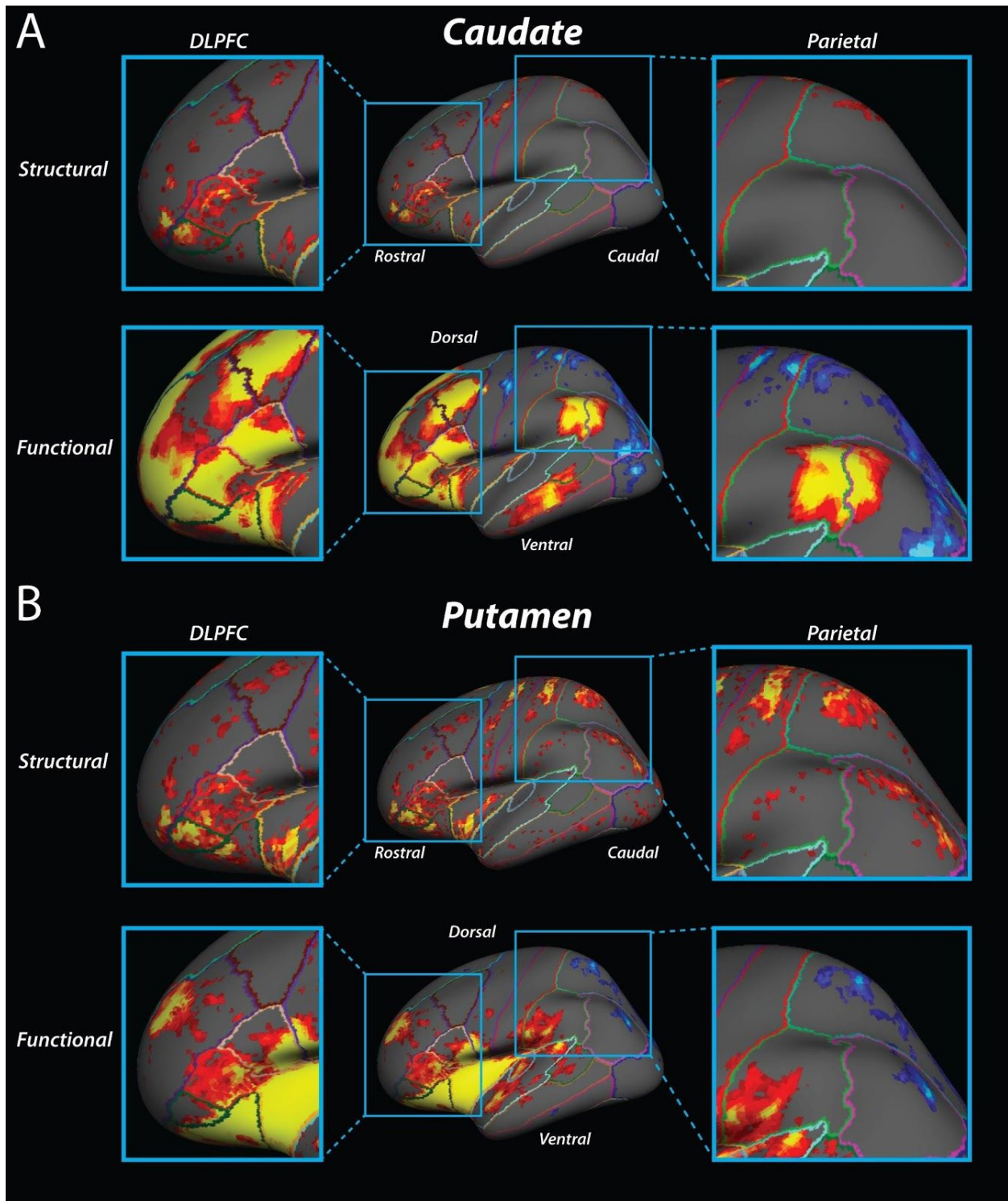


**Figure 4.7** Lateral surface maps of structural and functional convergence zone connectivity in DLPFC and parietal cortex on an inflated brain. A) Connectivity to the caudate convergence zone. B) Connectivity to the putamen convergence zone. Same plotting conventions as in Figure 4.6.

Connectivity to the putamen convergence zone appears to be located in similar areas of anterior prefrontal cortex and along the inferior and middle frontal gyri. The main difference between caudate and putamen convergence zone patterns is in the lateral frontal cortex where clusters of structural connections to the putamen are somewhat larger than structural connections to the caudate. Also, the putamen structural connectivity extends more ventrally in the inferior frontal gyrus (Figure 4.7b, top left). In Figure 4.7b (lower left panel), positive functional connectivity to the putamen convergence zone overlaps with structural connections throughout the inferior frontal gyrus. Small clusters of structural connections appear to overlap with sparse functional connections located in the rostral region of the middle frontal gyrus, contiguous with functional connectivity in rostral superior frontal gyrus; however, the structural connections in this region extend much further back along the middle frontal gyrus than the spread of functional connections.

In parietal areas, an interesting pattern emerges with regards to the specificity of connections to the striatal convergence zones. Functionally, the connections to the striatal convergence zones are separated along a dorsal–ventral plane, with patches of negative connectivity present along the superior parietal lobule and dorsal aspects of the intraparietal sulcus and patches of positive connectivity in ventral parietal regions (Figure 4.7a, b, top right). The dorsal negative connectivity region appears to be more distributed for connections to the caudate than to the putamen convergence zone. More importantly, the negative functional connectivity clusters overlap or are physically adjacent to regions of structural connections to both striatal convergence zones (Figure 4.7a, b, bottom right).

For connections to the caudate convergence zone, the positive functional connectivity area in the ventral parietal cortex resides on the border of the supramarginal gyrus and the angular gyrus (Figure 4.7a, bottom right). In contrast, for connections to the putamen convergence zone, this positive connectivity region is shifted in a rostral direction and isolated primarily within the supramarginal gyrus, near the temporal–parietal junction (Figure 4.7b, bottom right). However, here the structural connections do not overlap well with the pattern of functional connections for either convergence zone. We failed to find any structural connections near the positive functional connectivity cluster for the caudate convergence zone. Although there is distributed structural connectivity to the putamen convergence zone along the supramarginal and angular gyri, only the most rostral clusters of structural connections appear proximal to the positive functional connectivity region on the supramarginal gyrus. Thus, the only region with consistent structure–function overlaps in the parietal cortex extended along the superior parietal lobule.

Given the incomplete qualitative overlap of structural and functional connectivity, we sought to determine the likelihood that this overlap is due to chance. To quantify the degree of overlapping connections, we calculated the probability that structurally connected voxels were also functionally connected (i.e.,  $P(\text{connection fMRI} \mid \text{connection DSI})$ ) (Section 4.3.4) and used randomization statistics to estimate the probability of observing this overlap by chance. These results are summarized in Table 4.1. The highest degree of overlap was found for the caudate convergence zones. These have the highest degree of specificity of all striatal clusters (i.e., strongest overlap within pairwise maps and weakest connectivity with non-pairwise maps). The functional connectivity of the caudate convergence zones significantly overlaps with the

structural connectivity of the two putamen clusters, but the degree of this overlap is much smaller than the overlap with the structural connectivity estimated from the caudate convergence zone. Similarly, functional connectivity to the putamen convergence zone overlapped significantly with the structural connectivity to all three striatal clusters; however, unlike the caudate results, the overall degree of overlap was generally smaller and fairly equally distributed across all three striatal clusters. Thus, in both the convergence zone clusters and in both hemispheres, we see a greater degree of overlap in the patterns of functional and structural connectivity than would be expected by chance. In contrast, the control clusters in the motor putamen do not show this pattern. The functional connectivity to the left motor putamen does not significantly overlap with the structural connectivity from any of the striatal clusters in the ipsilateral hemisphere, although the highest degree of overlap was with the structural connectivity patterns to the same set of voxels. The functional connectivity to the right motor putamen only significantly overlapped with the structural connectivity to the same cluster of voxels, but not to the structural connectivity maps to either of the convergence zones. This overlap of functional and structural connectivity patterns in the cortex provides confirmation that voxels showing direct anatomical connections to the striatal convergence zones have a high likelihood (well above chance) of being associated in their functional dynamics. Furthermore, the cortical distribution of inputs to the convergence zones reflects a unique set of frontoparietal networks and not a general pattern of corticostriatal connectivity.

#### 4.4 Discussion

Our results identify a novel set of regions in the rostral and dorsal striatum that concurrently exhibit structural and functional connectivity to orbitofrontal, lateral prefrontal, and posterior parietal regions of cortex. The location of these convergence zones is anatomically consistent with previous reports of parietal (Selemon and Goldman-Rakic, 1985, 1988; Cavada and Goldman-Rakic, 1991) and frontal (Haber et al., 1995; Averbeck et al., 2014) white matter projections, based on ex vivo nonhuman primate histology. Although the distribution of cortical regions associated with the striatal convergence zones differed to some degree between structural and functional connectivity measures, reflecting methodological limitations of each approach, a majority of cortical areas structurally connected to the convergence zones also showed strong functional connectivity. This supports the notion that these corticostriatal projections form an integrative functional circuit.

The current findings support a growing body of evidence that basal ganglia circuits are more complex and interactive than the classic independent, parallel pathways model (Alexander et al., 1986). We confirmed the presence of two previously described gradients of connectivity within the corticostriatal pathways: a global medial–lateral gradient (Selemon and Goldman-Rakic, 1985; Haber, 2003) and a more local rostral– caudal gradient (Nauta and Whitlock, 1956; Kemp and Powell, 1970; see also Draganski et al., 2008; Verstynen et al., 2012). The complexity of these gradients highlights the fact that demarcating independent corticostriatal circuits remains a challenge (Choi et al., 2012).

Histological work has also shown that corticostriatal pathways from disparate cortical areas have some overlapping termination fields within the striatum (Selemon and

Goldman-Rakic, 1985; Haber, 2003; Haber et al., 2006; Averbeck et al., 2014). Accordingly, we observed clusters of voxels (i.e., convergence zones) bilaterally within striatal nuclei where projections from several cortical areas, including OFC, DLPFC, and posterior parietal cortex, terminate. This is in line with recent work in humans showing that distinct striatal regions are functionally connected with networks of distributed cortical areas, including the frontoparietal association, default mode, and limbic networks (Choi et al., 2012). Although previous work has separately shown projections from OFC (Selemon and Goldman-Rakic, 1985; Haber et al., 2006) and posterior parietal cortex (Selemon and Goldman-Rakic, 1988; Cavada and Goldman-Rakic, 1989b, 1991) overlap with DLPFC projections, to the best of our knowledge, the present findings show the first evidence of a convergence of projections from all three cortical areas to common striatal targets.

We propose that this pattern of convergent connectivity may reflect a potential mechanism for integrating reward processing, executive control, and spatial attention during spatial reinforcement learning (Colby and Goldberg, 1999; Behrmann et al., 2004; Gottlieb, 2007). This type of learning is thought to arise from feedback signals refining behavioral action selections and strategies, to improve efficiency during visual search for highly rewarded spatial targets versus targets that are less rewarded (Della Libera and Chelazzi, 2006; Kristjánsson et al., 2010; Navalpakkam et al., 2010; Lee and Shomstein, 2014). At the neural level, performance on spatial reinforcement tasks has been shown to be associated with concurrent activity of posterior parietal and DLPFC areas (Lee and Shomstein, 2013); however, in order for feedback to bias spatial attention, signals from cortical areas linked to attention must be integrated with reinforcement learning processes (i.e., evaluating previous outcomes and using them to shape

response selection). Functionally, the OFC has been implicated in providing reinforcement signals that influence behavior (O'Doherty, 2004; Hare et al., 2008; Schoenbaum et al., 2010). Thus, convergence of orbitofrontal signals into regions of the striatum that also receive projections from cortical areas linked to spatial attention and executive control could provide a substrate for adapting spatial decisions.

The dual location of the projections from the OFC into the striatal convergence zones may also help to elucidate the role of feedback control in spatial learning. Orbitofrontal areas have a well-described dual topography of representation: one for sensory modality and feedback type (i.e., reward and punishment) and another for complexity of feedback information (for complete review, see Kringelbach and Rolls, 2004). We observed two distinct clusters of orbitofrontal projections into the convergence zones that illustrate this dual topography (see Figure 4.4, bottom row middle). The larger cluster of projections to both striatal nuclei was found in posterior lateral orbitofrontal areas that are linked with processing low complexity visual signals. This supports the idea that these projections are linked to processing signals necessary for visuospatial attention. The second, smaller, cluster of projections originated in anterior medial regions and terminated only within the putamen convergence zones. These may reflect subsets of projections to pure ventral striatal pathways linked directly to reward processing (e.g., the ventral parts of the putamen clusters illustrated in Figure 4.3, left column), suggesting that these striatal convergence zones may reflect multiple forms of feedback processing during spatial learning.

Within the striatal nuclei, the location of the convergence zones also provides some clues as to the possible functional roles of these integrative networks. For example, we observed

convergence zones that extended into the dorsomedial caudate nucleus. This area has been strongly implicated in reinforcement learning in human functional neuroimaging studies (O'Doherty et al., 2004; Delgado et al., 2005; Schönberg et al., 2007; Badre and Frank, 2012). When these previous studies are considered together with our coincidental observation of structural and functional connectivity between OFC, DLPFC, and posterior parietal cortex in the striatum, the convergence of these three corticostriatal pathways, particularly within the dorsomedial caudate, may underlie context-dependent, spatial reinforcement learning suggested in previous research (Nieuwenhuis et al., 2005a; b; Lee and Shomstein, 2013).

Of course, it is possible that at least part of the interaction between parietal, OFC, and DLPFC functions is mediated by direct intracortical structural connections (Ridderinkhof et al., 2004); however, our current findings are consistent with a model in which part of this integration may happen at the corticostriatal level (Haber et al., 2006). Similarly, histological work supports potential models of spatial attention and executive control integration via direct cortical connections between posterior parietal cortex and DLPFC (Cavada and Goldman-Rakic, 1989b), as well as overlapping corticostriatal projections (Cavada and Goldman-Rakic, 1991). Although we cannot rule out a direct corticocortical connectivity hypothesis, our findings afford some confirmation for the integration of spatial attention and executive control signals in striatal areas that also receive inputs from the OFC, which is consistent with a corticostriatal mechanism for spatial reinforcement learning.

Our conclusions about this pathway are tempered, however, by inherent methodological limitations with the neuroimaging techniques that we used. The low spatial resolution of current MRI techniques ( $2\text{--}3 \text{ mm}^3$  voxels), relative to histological approaches, means that it is not

possible to directly infer whether the pathways we visualized are converging on the same striatal cells or merely terminating in adjacent regions of the nucleus. Even considering that it is possible to get subvoxel resolution with tractography on diffusion imaging data (Verstynen et al., 2011, 2012), this resolution is simply not fine enough to detect true converging collaterals on the same neuron. This coarse resolution of current MRI-based approaches limits our inference to interactions that occur at the voxel level.

Another concern relates generally to rsfMRI functional connectivity analyses, which is an indirect measure of connectivity based on correlated activity throughout the brain. At the timescale of the BOLD response, it is impossible to differentiate direct functional connections to a seed region from indirect connections (Cole et al., 2010). Thus, our inferences based on rsfMRI data can only imply that connected regions represent a functional circuit, but they cannot confirm that correlated areas are directly connected to each other. Although fiber tractography provides a more direct estimate of underlying white matter connections, this approach is still highly sensitive to various sources of noise (Jones, 2008) and suffers from several spatial biases that preclude complete identification of all underlying connectivity (Thomas et al., 2014). This bias may explain some of the discrepancies between the structural (Figure 4.4) and functional (Figure 4.5) connectivity patterns in the present study, particularly in DLPFC regions. Finally, neither DSI nor rsfMRI can confirm the task relevance of the cortical areas that we examined. To directly address our hypothesis that this network reflects a neural substrate for spatial reinforcement learning, future work should look at functions of this network during tasks that require the integration of reward, executive control, and spatial attention.

#### 4.5 Conclusion

Despite these limitations, the present findings provide clear evidence that projections from OFC, DLPFC, and posterior parietal cortex terminate in common striatal regions. Although our results are consistent with several independent findings in primate neuroanatomical literature, no previous study has shown the specific convergence of these three corticostriatal pathways in the human brain. This highlights a plausible structural mechanism that could allow for parietally mediated spatial attention processes to contribute to the integration of reward and response selection. Future work should explore the particular dynamics of the neural circuit that we have described here for their potential role in the integration of spatial attention information with reward and executive control processes during reinforcement learning.

# **Chapter 5**

## **Left putamen encodes task context during risky spatial decisions**

Chapters 2 and 3 chart the development of a novel behavioral paradigm that allowed us to provide strong empirical evidence for previously untested theoretical predictions about sensorimotor action selection behavior within the context of risky spatial decision-making research. Namely, we showed that avoidant selection behavior during risky spatial decisions is strongly influenced by significant interactions between cost and sensory variance as well as an interaction between cost and the contextual framing of the decision-making task. In Chapter 4, we identified a network of corticostriatal connectivity in humans that may support the integration of information about cost, sensory uncertainty, and context distributed across frontal and parietal cortices within regions of the anterior striatum that are associated with representations of action-value. For the final project of this dissertation, we examine whether or not this network indeed represents different levels of cost and contextual information to reflect a subjective value signal that impacts sensorimotor selection behavior via convergent corticostriatal circuitry.

### **5.1 Introduction**

Risky spatial decision-making involves multiple cognitive and sensorimotor processes wherein information about task contexts, costs, and sensory uncertainty must be represented. Chapter 1

details both the processes and their associated brain regions in humans and nonhuman primates. Specifically, differential levels of activation in prefrontal cortex (PFC) can be used to distinguish between multiple task contexts that guide action selection (Badre & Frank, 2012), orbitofrontal cortex (OFC) activity tracks reward and penalty associated with sensory stimuli (Kringelbach & Rolls, 2004), and activity in posterior parietal cortex (PPC) represents the spatial targets of movement (Gottlieb, 2002, 2007). Together, information from these disparate cortical areas can contribute to spatial decision-making in risky contexts through integrative cortico-basal ganglia circuitry (Haber, 2016) that loops back to cortical areas involved in motor execution (Alexander et al., 1986; Haber & Calzavara, 2009; Parent & Hazrati, 1995). In Chapter 4 (Jarbo & Verstynen, 2015), our multimodal neuroimaging work has shown that the structural (Averbeck et al., 2014; Selemon & Goldman-Rakic, 1985, 1988) and functional (Choi et al., 2012) PFC, OFC, and PPC connectivity converge within distinct regions of the anterior striatum, which are widely implicated in value-based action decisions (Pauli et al., 2016). This convergent corticostriatal circuitry delineates a potential mechanism by which the contextual framing, costs, and sensory estimates that guide value-based action selections are represented and integrated during risky spatial decision-making.

Our findings presented in Chapter 3 provide evidence that selection behavior changes significantly under varying levels of contextual framing, costs, and sensory uncertainty, which led us to question whether differences in selection behavior were due to distinct mental representations at certain levels of the Drone Strike task conditions. To address this question, we used fMRI with a multivariate pattern analysis method, representational similarity analysis (RSA) (Kriegeskorte, Mur, & Bandettini, 2008), that can be used to examine the differences

between patterns of BOLD activation occurring within and between brain regions. A pattern of activation refers to the levels of BOLD activation for a given task condition of each voxel in a set of voxels that comprise an ROI. Greater differences, or distances, quantify the dissimilarity between patterns of activation and indicate more distinct representations of a condition within or between ROIs, whereas distances closer to zero indicate similar representations. Since univariate fMRI analysis approaches average over these patterns of activity, they are limited to identifying brain regions that are generally involved in a task and may only be sensitive to distinct task conditions when there is significant change in the condition-specific magnitude of BOLD activation in those regions. By quantifying pattern differences using multivariate methods like RSA, both the engagement of a brain region in a task, as well as any potentially distinct representations of different task condition levels within and between regions can be assessed (e.g., individual finger movements in primary motor and sensory cortex (Diedrichsen, Wiestler, & Krakauer, 2013; Walther et al., 2016), face and house exemplars in inferotemporal cortex (Kriegeskorte et al., 2008), and object-specificity in perirhinal cortex (Clarke & Tyler, 2014). RSA provides a powerful method for distinguishing between patterns of neural responses that correspond to condition-specific mental representations of a behavioral task.

In this final dissertation experiment, we address Aim 3 where we hypothesized that patterns of BOLD activity in the anterior striatum encode different levels of task conditions during risky spatial decisions. Based on our identification of convergent corticostriatal connectivity (Chapter 4) (Jarbo & Verstynen, 2015), we used a set of a priori, structurally-defined striatal and cortical ROIs from that study with a version of the Drone Strike paradigm (Chapter 3) adapted for fMRI in a group of healthy adult participants. To determine

whether or not the network differentially represents levels of context (i.e., harm vs help) and cost (i.e., no-penalty vs penalty), we use RSA to assess the degree of similarity between patterns of BOLD activity within regions of PFC, OFC, PPC, and the anterior striatum. In particular, if any of the striatal convergence zones reliably distinguishes between task contexts and costs, then that region may serve as an integrative hub that represents a subjective value signal that can impact action selections during risky spatial decisions.

## 5.2 Methods

### 5.2.1 Participants

We recruited a total of 20 participants (mean age = 23.6, age range = 18-35; 17 female, 3 male) who all performed a revised version of the Drone Strike task (see Section 5.2.2) while we collected whole brain fMRI data of BOLD activity. Prior to the MRI session, 19 participants completed two consecutive 1-hour sessions of the behavioral task described in Chapter 3. The 20th participant completed two full behavioral sessions, but the participant pressed a key that caused the experiment code to terminate immediately before the final run of the task during the second session. The participant completed the final run, but the behavioral data from the first three runs of the task could not be recovered. Their data were excluded from the behavioral analysis, and that individual still participated in the MRI session described below. Fieldmap images for two participants (one female; one male) could not be reconstructed and then used to correct magnetic field inhomogeneities in the echo planar images (EPI) we acquired while the participants performed the task. Imaging data for those participants were excluded from all MRI analyses.

All participants were neurologically healthy adults with no history of head trauma, neurological or psychological pathology. Additionally, all participants were screened for normal or corrected-to-normal vision, colorblindness, right-handedness and unobstructed use of the right arm and hand to use an MRI-safe mouse during scanning, as well as any other standard contraindications to safely participating in an MRI scan. An experimenter reviewed a paper consent form with each participant and obtained informed consent approved by the Institutional Review Board at Carnegie Mellon University and the University of Pittsburgh from all participants in the study. All participants were compensated \$30 per hour for a total of \$45 upon completion of the 90-minute MRI scanning session.

### 5.2.2 Behavioral Experimental Design

Psychophysics Toolbox 3.0.12 (Brainard, 1997; Kleiner et al., 2007) with MATLAB (Release 2016a, The MathWorks, Inc., Natick, MA, United States) was used to conduct the experiment on a desktop computer running Ubuntu 16.04. All experimental task instructions and stimuli were presented on a 24" LCD screen with a total resolution of 1920 x 1200 pixels and a 60 Hz screen refresh rate that was positioned at the rear end of the magnet bore. All participants reported having full view of the screen via a mirror positioned atop the head coil. In the scanner, participants used an MR-safe optical computer mouse (MagDesign) and mouse pad fitted onto a plastic lapboard to perform the behavioral task.

In this revised version of the Drone Strike paradigm, we used a 2x2 (harm vs. help context x no-penalty vs. penalty) within-subject design. Based on our findings in Chapter 3, the significant interaction between context and cost is of interest in this study and it is directly

relevant to our prediction that the contextual framing of a spatial decision influences action-value representations within the striatum. Also, given that the significant effect of target variance on selection behavior has been well-established via replication across both experiments in Chapters 2 and 3, we eliminated the low variance condition, so that the target stimuli across all conditions and trials had high variance, i.e., standard deviation = 100 pixels. We provide additional details below about how stimulus presentation here differs from the version of Drone Strike described in Chapter 3. All participants completed a total of eight fMRI scan runs that lasted 7:10 minutes. We used a block design with 20 s of task followed by a rest period of 12-20 s (uniformly sampled, mean rest period = 16 s) to allow for relaxation of the BOLD signal after the final trial of a block. Participants attempted to complete as many trials as possible within each of eight task blocks. The order of blocks was counterbalanced within runs using a Latin square approach that minimized the correlation between block orders across runs for each participant.

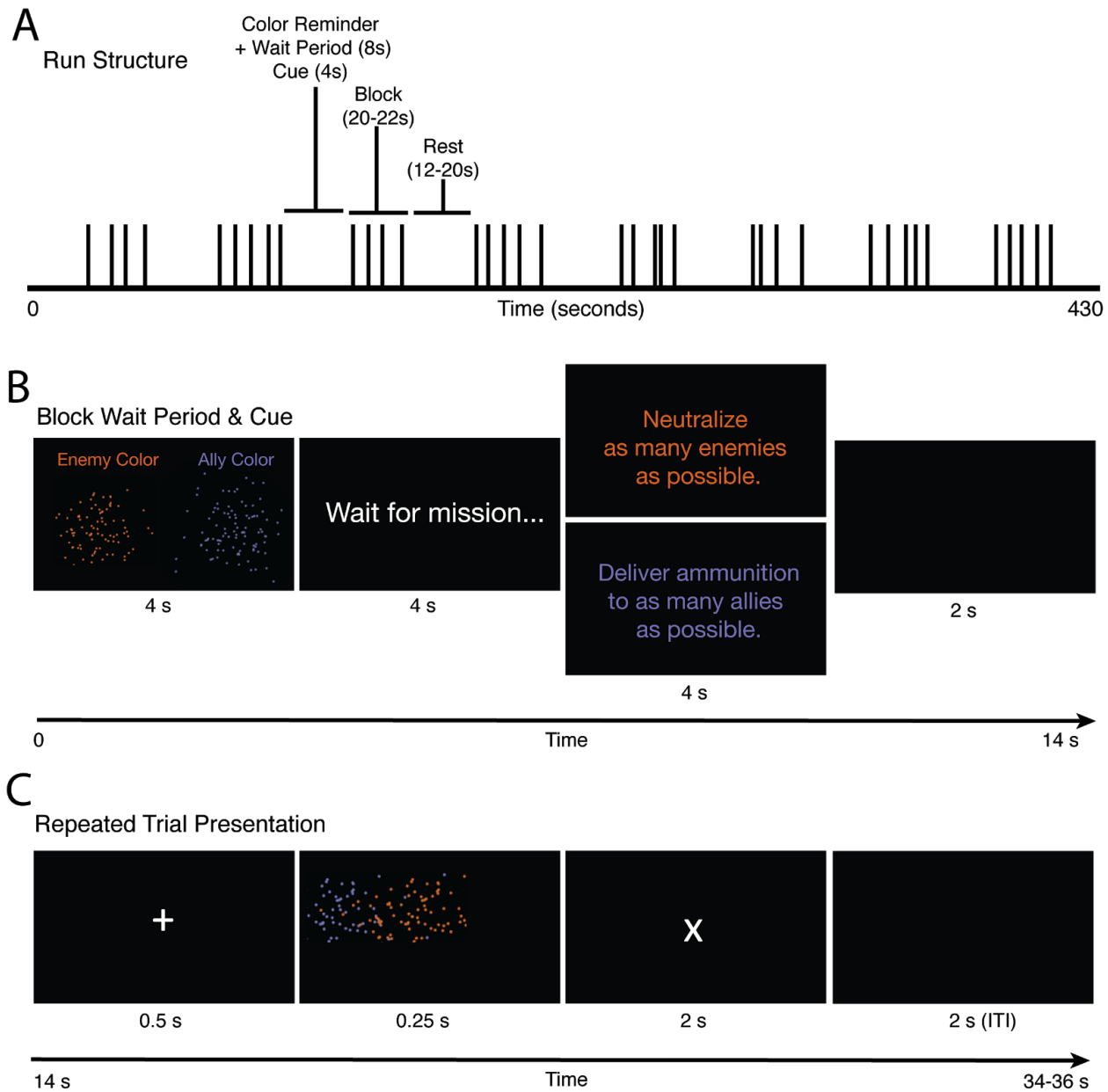


**Figure 5.1** Experimental run, block, and trial timelines. A) In each run, participants completed eight blocks of trials that lasted 20-22 s that were each followed by 12-20 s of rest. A run lasted 7:10 minutes. B) At the beginning of each block, text reading “Wait for instructions” appeared for 4 s and cued participants to the upcoming set of block instructions. Then, participants received a reminder of the enemy, ally, and tree distribution colors for 4 s followed by a 4 s presentation of text instructions in the font color the same color as the target distribution for that block. The offset of block instructions onscreen signaled the beginning of each block. A blank screen was then presented for 2 s prior to the first trial within each block. C) A fixed ITI = 2 s was used

prior to each trial. Each trial began with a fixation (+) presented at the center of the screen. Participants had to click and hold the left button within 500 ms of fixation onset to initiate the trial or else an “ABORT” message appeared for 500 ms indicating a failed trial. On a successfully initiated trial, the target and non-target stimulus distributions appeared onscreen for 250 ms and then disappeared. Participants then had 2 s to indicate their target selection by dragging the cursor (x) and releasing the mouse button. An “ABORT” message was displayed for 500 ms on trials where participants failed to execute a selection within 2 s. The next trial began 2 s after a selection was made or after the “ABORT” message disappeared. At the end of each block, a blank screen was presented during the 12-20 s rest period until the next set of stimulus reminders and block instructions were presented. Note: Stimuli and fonts in figure are rescaled here for clarity.

On each block of trials, participants were tasked with using a computer mouse to select a location within a target stimulus distribution that was visually overlapped by a non-target stimulus distribution presented simultaneously onscreen (Figure 5.1). Participants were also instructed to attempt to complete as many trials as possible within each block and across the entire experiment. We continued to use the same wartime scenario used in the original version of Drone Strike to provide contextual framing for each task condition, wherein participants selected either the location of a missile strike on enemies or an ammunition delivery to allies from a drone on a series of trials within a block. Prior to the experimental task runs, participants completed four practice blocks to familiarize themselves with using the optical mouse and lapboard during the acquisition of a T1-weighted structural image. An experimenter simultaneously verified practice performance of each participant via a monitor in the scanner control room. All participants verbally confirmed that they were comfortable performing the task and understood the new task timing structure.

Before each block of trials, participants were presented for 4 s with a visual reminder of the colors that corresponded to the enemy and ally stimuli. To control for the effect of stimulus

color on selection behavior, two sets of three colors (set 1: purple, red, white; set 2: magenta, blue, yellow) were alternated between participants with the colors of enemies, allies, and trees being counterbalanced within participants. Each participant only saw one set of colors, and the colors that corresponded to each of the three stimulus types remained the same for the entire experiment. We selected sets of colors such that any stimulus color in a pair was readily discriminable.

After a wait screen was presented for 4 s, the instruction for the upcoming set of trials was presented for 4 s. On “drone strike” missions, participants were instructed to “Neutralize as many enemies as possible” and to “Deliver ammunition to as many allies as possible” on “ammunition delivery” missions. In both cases, the color of the instruction text matched the target stimulus (i.e., enemies on drone strikes and allies on ammunition deliveries). Following the instruction period, a blank screen was presented before a fixation (+) appeared at the center of the screen indicating the onset of a trial. A fixed ITI = 2 s was used as the onset time for each trial within a block.

To initiate a trial, the participant had to click and hold the left mouse button within 500 ms, otherwise they received an “ABORT!!!” message at the center of the screen indicating a failed trial. For successfully initiated trials, the target and non-target distributions were presented together for 250 ms before disappearing. Both the target and non-target distributions appeared completely on the screen. Each stimulus distribution was presented as a Gaussian distribution of 100 dots that were three pixels in diameter. The non-target distribution could appear either to the right or left of the target distribution with equal probability across trials. The means of the distributions were separated by fixed horizontal distance of 50 pixels and were randomly

sampled from a distribution of 2D coordinates to appear a minimum of 350 pixels away from the center of the screen. On no-penalty blocks, the non-target stimulus distribution represented the position of trees. On penalty blocks, the target and non-target distributions represented the positions of enemies and allies, respectively. The standard deviation of both the target and non-target distributions were held constant at 100 and 25 pixels, respectively, across the entire experiment for all participants.

After the stimulus distributions disappeared, the mouse cursor was immediately presented as an “x” at the center of the screen. Participants then had 2 s to drag the cursor to a location and then release the mouse button to indicate their selection for each drone strike or ammunition delivery. Upon completion of a successful or failed trial, a subsequent trial was immediately initiated after the 2 s ITI until the end of the 20 s block. An additional 2 s padded the end of each block in the event that an initiated trial was in progress after 20 s from block onset to allow for the participant to complete the trial. All participants completed at least 319 total trials across the entire experimental session. At the end of each block and run, a report screen was presented that indicate the progress through the experiment along with a running total of enemies killed, allies killed, ammunition delivered, and ammunition intercepted. This report remained on the screen for 4 s followed by a blank screen until the cue for the next block appeared on the screen at the end of the 12-20 s rest period. A final score report screen was presented at the end of the scanning session before the participant was removed from the scanner.

The same scoring structure used in Chapters 2 and 3 were used in this experiment. Regardless of context (i.e., drone strike or ammunition delivery) or cost (i.e., no-penalty or penalty) condition, selecting the mean of the target distribution guaranteed the maximum

possible score on a trial. *Equations 2.2-2.4* were used to calculate scores across trials. First, the Euclidean distance between a selection and the target distribution mean (*Equation 2.2*) and the non-target distribution mean (*Equation 2.3*) were computed. These distances were used in weighted hyperbolic functions with a  $1/d$  falloff to compute the score for each trial. *Equation 2.3* shows the target function weighted by  $\omega$  and the non-target by  $1-\omega$ . In no-penalty blocks,  $\omega = 1$ , so that only the selection distance from the target contributed to the score (i.e., no loss, only enemy kills or ammunition delivered), while  $\omega = 0.33$  to additionally reflect losses on penalty blocks as ally kills or ammunition intercepted. As in Chapter 3, the computed scores were multiplied by 1000, rather than 100, and rounded to yield an integer value between 0 and 100 for each trial. The total score for each block of trials was added to a running total across all blocks within each experimental session.

### 5.2.3 Behavioral Data Analysis

For the present study, we performed analyses on the same behavioral dependent measures as Chapter 3 with the exception of selection variability: selection bias away from the target, selection variability (SV), reaction time (RT), movement time (MT), maximum mouse cursor velocity (maxV), and average mouse cursor velocity (avgV). All calculations used to compute each dependent variable from selection, timing, and movement data were the same as previously described. We refer the reader to Section 3.2.3, for full details of these calculations.

All dependent variables were subjected to a two-way repeated measures ANOVA to observe whether there were any significant 2-way interactions or main effects of context and cost. Since five dependent variables were subject to ANOVA, a Bonferroni correction of  $\alpha =$

$0.05/6 = 0.008$  was used as a threshold for statistical significance. For significant results on omnibus F tests, effect sizes were estimated as  $\eta_p^2$ . In order to determine the directionality of significant main effects or interactions from the omnibus F tests, we report the group means and standard errors for each dependent variable across all conditions, and the results of 1-sample and paired sample t-tests with effect sizes computed as Cohen's d.

#### 5.2.4 MRI Acquisition

All MRI data were acquired at the Scientific Brain Imaging Research Center at Carnegie Mellon University on Siemens Verio 3T magnet fitted with a 32-channel head coil. Full details of our scanning protocol and acquisition parameters used for all participants are presented in Table 5.1. Whole brain images were acquired for all scan sequences. After the two localizer scans, a T1-weighted structural image was then acquired while participants practiced the task. The structural scan was followed by the first four runs of the task, field maps, and final four runs of the task. The entire MRI session took no longer than 90 minutes with approximately 70 minutes of scanning time per participant.

**Table 5.1** MRI scanning protocol and acquisition parameters

| Scan Type   Parameters  | T1 (structural)                 | BOLD-EPI (functional)           | Field Map                       |
|-------------------------|---------------------------------|---------------------------------|---------------------------------|
| No. of scans            | 1                               | 8                               | 1                               |
| No. of volumes          | 1                               | 210                             | 1                               |
| Pulse sequence type     | T1                              | echo-planar                     | gradient echo                   |
| Parallel imaging        | GRAPPA = 2                      | Multiband = 3                   | N/A                             |
| Field of view           | 256 x 256 x 176 mm <sup>3</sup> | 212 x 212 x 138 mm <sup>3</sup> | 212 x 212 x 138 mm <sup>3</sup> |
| Matrix size             | 256 x 256                       | 106 x 106                       | 106 x 106                       |
| Slice thickness         | 1 mm                            | 2 mm                            | 2 mm                            |
| Interslice skip         | 0.5 mm                          | 0 mm                            | 0 mm                            |
| Acquisition orientation | sagittal                        | axial<br>-38 deg tilt           | axial<br>-38 deg tilt           |
| Acquisition order       | single-shot<br>ascending        | interleaved                     | sequential<br>ascending         |
| Echo time (TE)          | 1.97 ms                         | 30.0 ms                         | 4.60 ms<br>7.06 ms              |
| Repetition time (TR)    | 2300 ms                         | 2000 ms                         | 8.8 ms                          |
| Flip angle              | 9 deg                           | 79 deg                          | 72 deg                          |

### 5.2.5 MRI Preprocessing

All MRI preprocessing was conducted using a combination of functions from SPM12 (version 7219; <http://www.fil.ion.ucl.ac.uk/spm>) and FSL (version 5.0.9; <https://fsl.fmrib.ox.ac.uk/fsl>). DICOM images for the T1, EPI, and field map images were converted into NIfTI volumes using `spm_dicom_convert` and `spm_file_merge` to combine all 3D EPI images into a single 4D volume. The same preprocessing steps were applied for all participant imaging data. First, the T1-weighted structural image dimensions were reoriented to RPI (right-left, posterior-anterior,

inferior-superior) using the `fslswapdim` function to match the MNI space convention of the `MNI152_T1_1mm.nii` T1-weighted 1 x 1 x 1 mm template image provided with FSL. To align the structural and functional scans within participants, we estimated the rigid body coregistration parameters for aligning the native space T1 to MNI space. We similarly estimated the coregistration parameters for aligning all EPI volumes of all scan runs to the `EPI.nii` T2\*-weighted 2 x 2 x 2 mm template provided with SPM. For both coregistration steps, we used the same estimation options (cost function = ‘`nmi`’, normalized mutual information; separation = [4 2]; tolerances = [0.02 0.02 0.02 0.001 0.001 0.001 0.01 0.01 0.01 0.001 0.001 0.001]; FWHM = [7 7]; interpolation = 4th degree spline; no wrapping; no masking) Next, to correct for any head movements that may have occurred during each scan run, we estimated six motion correction parameters for x, y, and z translation and rotation roll, pitch, and yaw axes (realign options: quality = 1; FWHM = 5 mm; separation = 2; realign to first image; wrap along y-axis = [0 1 0]; interpolation = 4th degree spline). These motion correction parameters were then included as regressors in our general linear model analysis. To apply the estimated coregistration and realignment parameters, we resliced (reslice options: masking = 1; interpolation = 4th degree spline; reslice all images and mean, which = [2 1]; wrap = [0 1 0]) resulting in the alignment of all EPI image volumes to the first volume of the first EPI run. We used a threshold of 2 mm of translation movement in any direction or 2 degrees of rotation on any axis as an exclusion criterion for motion. All participants had fewer than x mm and x degrees of movement. To correct for magnetic field inhomogeneities (B0 distortions), we created a voxel displacement map aligned to the first volume of the first EPI run using the FieldMap Toolbox provided with SPM12. The field map phase image and short TE magnitude image were used to estimate a voxel

displacement map using the FieldMap Toolbox default parameters, total readout time = 7.6318 ms. For two participants, field map reconstruction failed for reasons that we still have to investigate. Since correcting for B0 distortions can improve BOLD signal in regions of particular interest for this study (i.e., orbitofrontal cortex), we seek to address, and hopefully rectify, this issue to reanalyze the fully preprocessed EPI data. For successful voxel displacement map reconstructions, the map can be applied to EPI data to counter signal dropout that commonly occurs in ventral prefrontal brain regions during fMRI (Weiskopf, Hutton, Josephs, & Deichmann, 2006). Subsequent preprocessing and analyses were conducted on data without field map correction for all participants. To prepare the EPI data for group-level GLM analyses, we spatially normalized the motion corrected images using SPM12's batch normalization functions to estimate (normalization estimate options: bias regularization = 0.0001, bias kernel FWHM = 60; affine registration template = ‘mni’; regularization = [0 0.001 0.5 0.05 0.2]; smoothing kernel FWHM = 0; sampling distance = 2) the nonlinear transformation from native to MNI space using a set of tissue probability maps for gray matter, white matter, and CSF supplied by SPM12, and then apply (normalization write options: bounding box = [-78 -112 -70; 78 76 85]; resampled voxel resolution = [2 2 2]; interpolation = 4th degree spline) the transformation to all participant images. Lastly here, we smoothed the normalized data with a FWHM = [6 6 6] smoothing kernel.

### 5.2.6 Modeling BOLD Responses for General Linear Model (GLM) Analysis

Using a general linear model (GLM) approach, we estimated the BOLD response across the whole brain using a robust weighted least squares approach. From our block design, we used the

onset times (starting with the cue presentation) for both blocks of a given condition within a run to specify the first four regressor values within our design matrix for each condition: 1) harm x no-penalty, 2) harm x penalty, 3) help x no-penalty, 4) harm x penalty. As task regressors, we specified a fixed block duration of 26 s to include the cue presentation duration (4 s) and block duration with padding (22 s). We also included the six regressors that were estimated from the motion correction step described in Section 5.2.5. All regressors were orthogonalized with respect to the first regressor of a given scan run. We assumed the canonical hemodynamic response function (HRF) in SPM12 to model the BOLD response and high-pass filtered the time series using a discrete cosine transform with a cutoff of 96 s. To account for serial correlations in the data, we used an autoregressive AR(1) model globally across the whole brain. We constructed four separate contrasts on the task regressors to evaluate whether there were significant differences in the BOLD response for 1) task - rest: [1 1 1 1], 2) harm - help: [1 1 -1], 3) penalty - no-penalty: [-1 1 -1 1], and 4) context x cost interaction: [-1 1 1 -1]. After fitting the GLM, we generated contrasts images for all participants and then performed group-level inference by computing group t stat and p-value maps to determine which areas, if any, across the whole brain showed significantly different levels of BOLD activation for each contrast. To correct for multiple comparisons, we used an FDR threshold  $q < 0.05$ .

### 5.2.7 Defining Regions-of-Interest (ROIs)

To define the ROIs for analysis of our fMRI data, we used an a priori set of structurally connected striatal and cortical ROIs using diffusion spectrum imaging and fiber tractography that were validated by resting state functional connectivity described in Chapter 4 (Jarbo &

Verstynen, 2015). All four striatal ROIs contained endpoints from streamlines tracked separately from regions in dorsal prefrontal, orbitofrontal, and posterior parietal cortex to ipsilateral caudate and putamen for both hemispheres. Only contiguous voxels in each striatal nucleus that contained streamline endpoints from all three cortical regions comprised the striatal convergence zone ROIs. Those convergence zone ROIs were then used as seeds for tractography to create maps of ipsilateral cortical regions that were structural connected to each of the striatal convergence zones. As a control, we also tracked streamlines between the precentral gyrus (i.e., primary motor cortex) into ipsilateral putamen to identify motor putamen regions. Generally, the striatal ROIs were localized just caudal to nucleus accumbens and, in the putamen, rostral to motor-specific striatal regions. Clusters of endpoint terminations in the cortex were distributed broadly across all three cortical regions bilaterally. All 14 ROIs are listed in Table 5.2 and depicted in Figure 5.2.

**Table 5.2** Structurally-defined a priori striatal and cortical regions-of-interest

| Striatal           | Cortical                             | Motor (Control)             |
|--------------------|--------------------------------------|-----------------------------|
| Caudate (163, 34)  | Dorsolateral prefrontal (1440, 1437) | Precentral gyrus (879, 355) |
| Putamen (213, 109) | Orbitofrontal (215, 295)             | Motor putamen (176, 153)    |
|                    | Posterior parietal (407, 1201)       |                             |

All ROIs are bilateral and the number of voxels for the left and right ROI, respectively, are listed in parentheses

### 5.2.8 Transforming ROIs from MNI to native space

All cortical and striatal ROIs were generated in MNI template space and had to be transformed into the native space of each participant's EPI data to conduct the representational similarity

analysis. SPM12's spatial normalization function outputs a deformation field file in NIfTI format. The deformation field consists of a set of vector fields that describe the nonlinear transformation from native T1 space to MNI space. Using the pullback procedure in SPM12's deformation utility, we estimated the inverse deformation field and used a 4th-degree spline interpolation with no smoothing (i.e., Gaussian blurring) in order to warp the ROIs from MNI space into the native T1 space for each participant's dataset. Masking was enabled to ensure that no voxels outside of the images were sampled to estimate the transformation. Each of the ROIs was then resliced, using the `spm_reslice` function with a 4th-degree spline interpolation, masking enabled, and no wrapping, to the realigned and fieldmap corrected mean EPI volume from the first functional run.

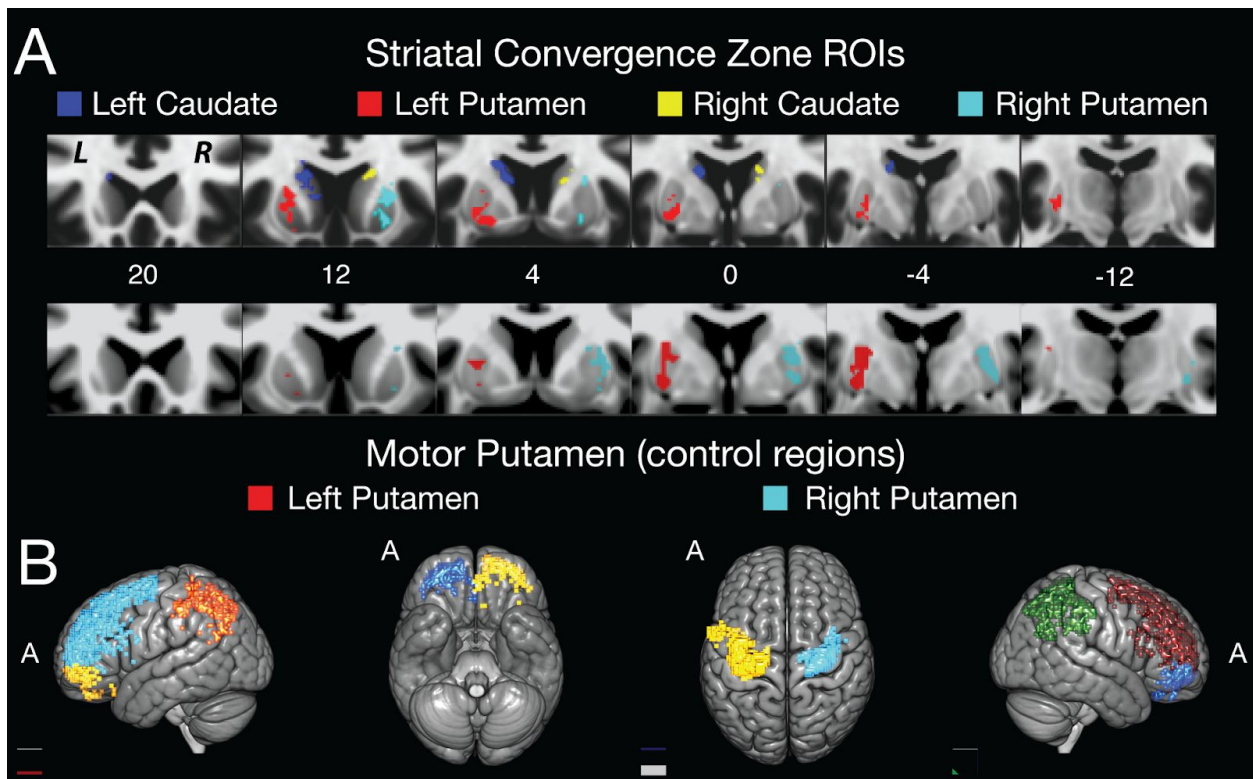


**Figure 5.2** Structurally-defined striatal and cortical ROIs. ROI-based analyses used a set of a priori ROIs located bilaterally within each nucleus of the striatum as well as prefrontal, orbitofrontal, and posterior parietal regions (Chapter 4). Each ROI was transformed from MNI space into the native EPI space for each participant’s dataset and the timeseries of BOLD activity across all scan sessions were extracted for all voxels in each ROI for subsequent analyses. A) Striatal convergence zones (top row) are located in the anterior striatum, just caudal to the nucleus accumbens and rostral to motor regions within the putamen with some overlap on the rostral-caudal axis. The images show coronal slices of a template brain in MNI space (larger positive numbers are more rostral) with the left caudate (blue), left putamen (red), right caudate (yellow), and right putamen (cyan) ROIs overlaid. Control regions in the motor putamen (bottom row; left = red, right = cyan) overlap with the convergence zones but are largely situated more caudally in the putamen. B) Cortical ROIs shown on a 3D brain, defined by endpoints of diffusion tractography seeded from ipsilateral striatal convergence zones, are located in lateral regions of dorsal prefrontal, orbitofrontal, and posterior parietal cortices. Views from left to right: left sagittal (OFC = yellow, DLPFC = cyan, PPC = orange), bottom-up axial (Right OFC = blue, Left OFC = yellow), top-down axial (Left Precentral = yellow, Right Precentral = cyan), right sagittal (OFC = blue, DLPFC = red, PPC = green). For orientation, a small capital letter A denotes the anterior/rostral direction.

### 5.2.9 ROI-based GLM contrast analysis

To investigate whether or not each ROI showed differences in the magnitude of BOLD activation across conditions, we compared the mean contrast values for each ROI estimated from the GLM. We constructed four contrasts for each condition: 1) Harm x No-Penalty: [3 -1 -1 -1], 2) Harm x Penalty: [-1 3 -1 -1], 3) Help x No-Penalty: [-1 -1 3 -1], 4) Help x Penalty: [-1 -1 -1 3]. For the group level analysis, we extracted contrasts values for each ROI from each participants spatially normalized and smoothed EPI data. We used custom MATLAB functions to index the voxel locations for each ROI for all participants and then took the corresponding values from the contrast image for each condition . We then conducted a two-way repeated measures ANOVA on the group means and computed the effect size for significant main effects

and interactions as  $\eta_p^2$ . Post-hoc t-tests were then performed to examine the magnitude and direction of significant main effects on contrast values.

### 5.2.10 Modeling BOLD responses for representational similarity analysis

To prepare data for ROI-based representational similarity analysis (RSA), we used a set of custom MATLAB scripts. First, the raw time series data for all voxels in each ROI were extracted from the motion corrected EPI data. We used the pca function with singular value decomposition in MATLAB to orthogonalize the time series data that were then high-pass filtered with a 96 s cutoff. A custom MATLAB function was used to estimate prewhitened beta parameters from the time series data. This prewhitening step accounts for the structure of noise variance and covariance between voxels in order to yield an unbiased estimate of distances between multivoxel patterns of activity (i.e., Mahalanobis distance) (Kriegeskorte, Goebel, & Bandettini, 2006).

### 5.2.11 Representational similarity analysis

To evaluate patterns of BOLD activity, we assume that each voxel in an ROI, for instance, responds similarly to repeated presentations of the same condition or trial type and a different response to. Correspondingly, we that same voxel is expected to show a different response to a different condition. This assumption extends to the multivoxel level in that every voxel in an ROI, constituting a pattern, is assumed to show a set of unique single-voxel responses to one condition and a distinguishable set of responses to another condition. The difference between two patterns can be computed as a distance, e.g., Euclidean, such that greater distances indicate

greater dissimilarity between information encoded by the voxel activity patterns within or between ROIs. We computed the Mahalanobis distance because its calculation accounts for the variance in voxel responses based on their spatial proximity to blood vessels as well as the covariance in responses of groups of nearby voxels. We used *Equation 5.1* to estimate the cross-validated Mahalanobis distance ( $\hat{d}$ ) between patterns ( $u$ ) for each pair of conditions ( $i, j$ ) and averaged across every pair of runs ( $m, l$ ; total runs  $M = 8$ ) for a total of (8 choose 2) 28 folds.

$$\hat{d}_{i,j}^2 = \sum_{l,m; m \neq l}^M (u_i^m - u_j^m)^T (u_i^l - u_j^l) / M(M - 1)$$

Eq. 5.1

Computing the Mahalanobis distance, downweights noisy and highly correlated voxels by estimating the variance and covariance of pattern responses (Kriegeskorte et al., 2006). Another advantage of computing the Mahalanobis distance is that the expectation for patterns that are the same or similar is 0 (Walther et al., 2016). This aspect makes the distance metric straightforward to interpret: When two patterns are the same or similar, then their true distance is 0, and positive distance values are indicative of uniquely represented information for each pattern. We then used a leave-one-run-out cross-validation to obtain the final Mahalanobis distance estimate  $\hat{d}$  for all six pairwise condition comparisons: 1) harm x no-penalty vs. harm x penalty, 2) harm x no-penalty vs. help x no-penalty, 3) harm x no-penalty vs. help x penalty, 4) harm x penalty vs. help x no-penalty, 5) harm x penalty vs. help x penalty, and 6) help x no-penalty vs. help x penalty. This 8-fold cross-validation yielded 28 unique  $\hat{d}$  values that we averaged together for

each pairwise condition comparison in all 14 ROIs to generate representational dissimilarity matrices (RDMs) (Kriegeskorte et al., 2008) (Figure 5.5). To get the average  $\hat{d}$  value for each RDM, we computed a statistic H that controlled for all the pairwise comparisons within the RDM (Beukema, Diedrichsen, & Verstynen, 2018). In Equation 2,  $d_{i,j}^2$  represents the Mahalanobis distance between the two patterns compared in each fold and  $k = 4$  task conditions.

$$H = \sum_{i \neq j}^k d_{i,j}^2 / k(k - 1)$$

Eq. 5.2

Lastly, to determine whether any ROI showed H values that were significantly greater than 0 across all participants, we conducted a right-tailed one-sample t-test against 0 on the group H values for all ROIs using a Bonferroni-corrected  $\alpha = 0.005$  to control for multiple comparison across all 10 cortical and striatal ROIs, excluding the four control regions in motor putamen and precentral gyri.

### 5.3 Behavioral results

We report our two-way repeated measures ANOVA results along with post hoc t-tests examining any interactions or main effects of context (harm vs help) and cost (no-penalty vs penalty) on selection behavior characterized by six dependent measures: selection bias, SV, RT, MT, maxV, and avgV (Figure 5.3 A-F). We also refer the reader to Tables 5.1 and 5.2 for all statistics, including group means and standard errors for each dependent variable. Overall, neither the

2-way interaction between context and cost nor the main effect of context were significant for any of the six dependent variables, all  $F(1,19)$ s  $< 3.841$ , all  $p > 0.065$ . We will further address these findings in light of our results in Chapter 3 in the Discussion (Section 5.4) of this chapter.

**Table 5.2** 2-way repeated measures ANOVA interaction and main effect results for dependent variables: selection bias, RT, MT, maxV, and avgV.

|                      | DV   | F(1,19) | p       | Sig. | $\eta_p^2$ | t(19)  | p       | Sig. | Cohen's d |
|----------------------|------|---------|---------|------|------------|--------|---------|------|-----------|
| Context<br>x<br>Cost | Bias | 3.757   | 0.068   | ns   | -          | -      | -       | -    | -         |
|                      | SV   | < 0.001 | 0.998   | ns   | -          | -      | -       | -    | -         |
|                      | RT   | 1.494   | 0.237   | ns   | -          | -      | -       | -    | -         |
|                      | MT   | 0.298   | 0.592   | ns   | -          | -      | -       | -    | -         |
|                      | maxV | 0.357   | 0.557   | ns   | -          | -      | -       | -    | -         |
|                      | avgV | 0.084   | 0.775   | ns   | -          | -      | -       | -    | -         |
| Context              | Bias | 0.070   | 0.794   | ns   | -          | -      | -       | -    | -         |
|                      | SV   | 0.339   | 0.567   | ns   | -          | -      | -       | -    | -         |
|                      | RT   | 0.332   | 0.571   | ns   | -          | -      | -       | -    | -         |
|                      | MT   | 3.841   | 0.065   | ns   | -          | -      | -       | -    | -         |
|                      | maxV | 0.017   | 0.896   | ns   | -          | -      | -       | -    | -         |
|                      | avgV | 0.439   | 0.515   | ns   | -          | -      | -       | -    | -         |
| Cost                 | Bias | 31.888  | < 0.001 | ***  | 0.627      | 5.647  | < 0.001 | ***  | 1.809     |
|                      | SV   | 34.255  | < 0.001 | ***  | 0.643      | -5.853 | < 0.001 | ***  | -1.613    |
|                      | RT   | 6.810   | 0.017   | *    | 0.264      | -2.610 | 0.017   | *    | -0.150    |
|                      | MT   | 17.795  | < 0.001 | ***  | 0.484      | -4.218 | < 0.001 | ***  | -0.289    |
|                      | maxV | 5.075   | 0.036   | *    | 0.211      | 2.253  | 0.036   | *    | 0.145     |
|                      | avgV | 17.678  | < 0.001 | ***  | 0.482      | 4.201  | < 0.001 | ***  | 0.296     |

Bonferroni-corrected  $\alpha = 0.008$  denoted by (\*\*\*)<sup>1</sup>. Significant uncorrected p-value  $\alpha = 0.05$  denoted by (\*). Post hoc paired t-tests for Context = harm - help and Cost = no-penalty - penalty.

**Table 5.3** Condition-wise group (N = 20) means and standard errors (SE) for dependent variables: selection bias, RT, MT, maxV, and avgV.

| Condition                        | Bias (pixels) |      | SV (pixels) |      | RT (ms) |     | MT (ms) |      | maxV<br>(pixels/s) |      | avgV<br>(pixels/s) |      |
|----------------------------------|---------------|------|-------------|------|---------|-----|---------|------|--------------------|------|--------------------|------|
|                                  | M             | SE   | M           | SE   | M       | SE  | M       | SE   | M                  | SE   | M                  | SE   |
| <i>Harm</i><br><i>No Penalty</i> | -27.15        | 5.77 | 59.73       | 5.27 | 32.3    | 3.1 | 521.1   | 41.8 | 85.03              | 4.16 | 16.78              | 0.94 |
| <i>Harm</i><br><i>Penalty</i>    | -61.83        | 4.43 | 89.52       | 3.00 | 33.8    | 3.1 | 580.1   | 43.6 | 81.87              | 4.05 | 15.61              | 0.79 |
| <i>Help</i><br><i>No Penalty</i> | -23.34        | 5.09 | 60.68       | 5.40 | 31.9    | 2.9 | 532.7   | 44.0 | 84.64              | 4.03 | 16.70              | 0.95 |
| <i>Help</i><br><i>Penalty</i>    | -64.68        | 4.17 | 90.45       | 3.36 | 34.8    | 3.7 | 585.6   | 44.1 | 82.43              | 4.41 | 15.57              | 0.81 |

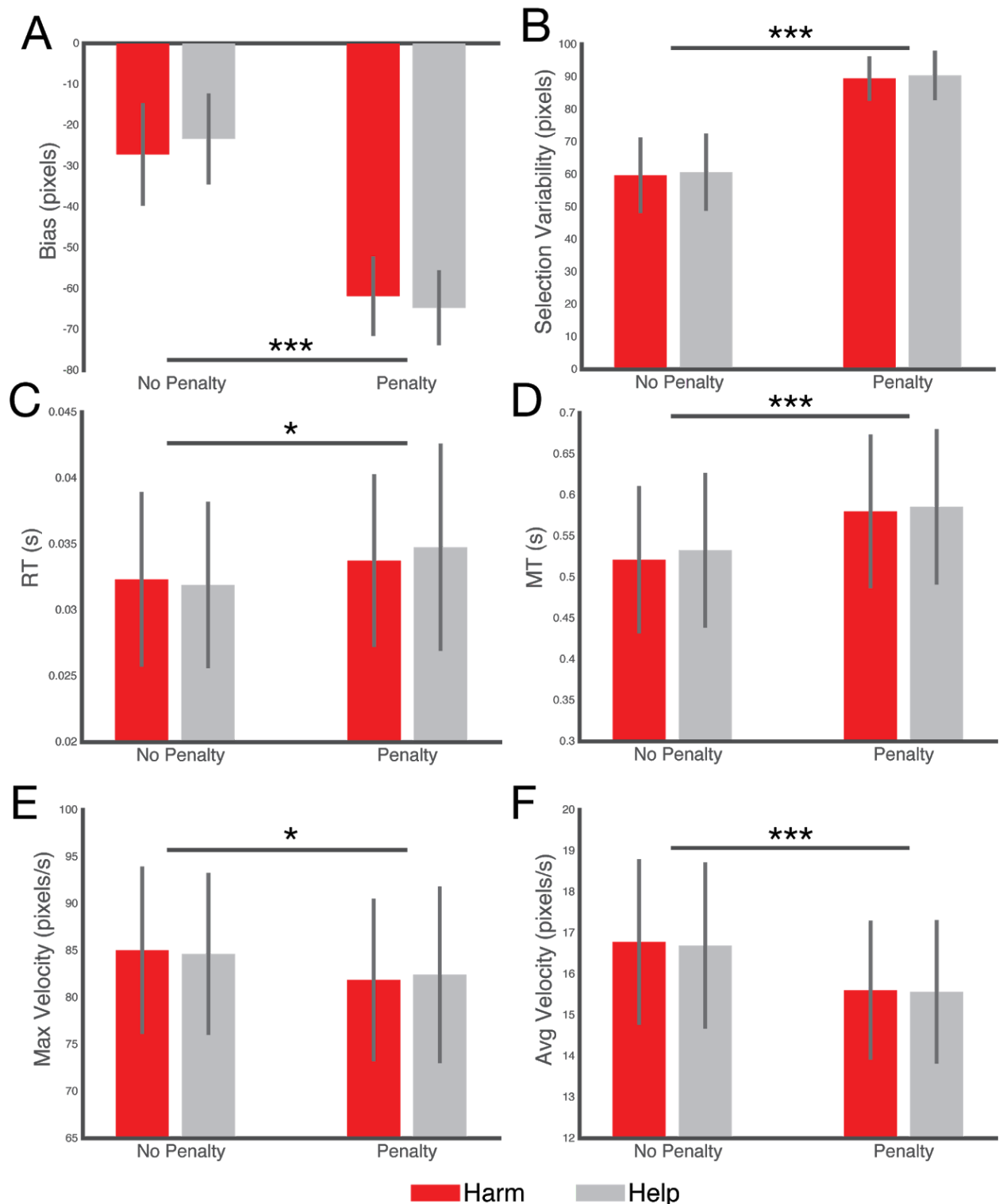


**Figure 5.3** Bar graphs with significant main effects of cost. In each panel, bars (red/left= harm, gray/right = help) represent the group means of each dependent variable across all conditions with error bars reflecting the 95% confidence intervals of the means.

Bonferroni-corrected  $\alpha = 0.008$  denoted by \*\*\* and uncorrected  $p < 0.05$  by \*. A) Selection bias measured in pixels and larger negative values indicate selections further away from the non-target distribution, while less negative and positive values reflect closer selections. The main effect of cost is denoted by a horizontal line in the bottom half of the panel. B) Selection variability is measured as the standard deviation of selections in pixels. Greater values correspond to greater selection variability. Horizontal line represents a significant main effect of cost. There were no significant interactions for RT, MT, maximum and average velocity, represented in panels C-F. Though a significant main effect of cost was observed for each as denoted by the horizontal lines. Greater values for RT and MT reflect slower times, while greater values for both velocity measures indicate faster mouse movements. All significant main effects, group means, and standard errors are also reported in Tables 5.2-5.3.

### 5.3.1 Selection bias and variability

We measured selection bias as the distance, in pixels, between a selection and the target mean on a trial as we did in Chapters 2 and 3. More negative values indicate selections further from the target mean in the direction away from the non-target. Less negative and positive values indicate selections closer to the non-target (Figure 5.3a). We found no significant interaction between context and cost,  $F(1,19) = 3.757$ ,  $p = 0.068$ , nor significant main effect of context,  $F(1,19) = 0.070$ ,  $p = 0.794$ , on selection bias. (However, we note that the context x cost interaction did trend toward significance, as expected based on our findings in Chapter 3. Using Grubb's test (Grubbs, 1969) on the selection bias data, we identified one participant whose bias scores across context conditions fell further than three standard deviations away from the group mean. When that participant's data were removed from the behavioral analysis, the context x cost interaction became significant,  $F(1,18) = 12.916$ ,  $p = 0.002$ ,  $\eta_p^2 = 0.418$ , suggesting that the current sample size is underpowered for detecting effects driven by the interaction.) The ANOVA revealed a significant main effect of cost on selection bias,  $F(1,19) = 31.888$ ,  $p < 0.001$ ,  $\eta_p^2 = 0.627$ . A post

hoc t-test confirmed that selection bias was less negative, i.e., closer to the non-target, in no-penalty conditions than penalty conditions,  $t(19) = 5.647$ ,  $p < 0.001$ , Cohen's  $d = 1.809$  (Tables 5.2 and 5.3).

Though we did not manipulate target variance here as we did in Chapters 2 and 3, we still measured and analyzed the effects of context and cost on selection variability. We computed selection variability as the standard deviation of selection endpoints across trials within each condition. Greater values indicate larger variance, or spread, of selection endpoints about the target mean (Figure 5.3B). We found no significant context x cost interaction or main effect of cost. We did observe a significant main effect of penalty on selection variability,  $F(1,19) = 34.255$ ,  $p < 0.001$ ,  $\eta_p^2 = 0.643$ . Selection variability was greater in penalty conditions than no-penalty conditions,  $t(19) = -5.853$ ,  $p < 0.001$ , Cohen's  $d = -1.613$  (Tables 5.2 and 5.3). Our findings for the main effect of cost on selection bias and variability closely match those of Chapters 2 and 3.

### 5.3.2 Reaction and movement time

Reaction time was recorded at the first mouse movement detected after stimulus offset (Figure 5.3c). We found no significant context x cost interaction nor main effect of context on RT,  $F(1,19)s < 1.494$ , all  $ps > 0.237$ . Though above the Bonferroni-corrected threshold ( $\alpha = 0.008$ ), we saw a small main effect of cost on RT that was significant at an uncorrected  $p < 0.05$ ,  $F(1,19) = 6.810$ ,  $p < 0.017$ ,  $\eta_p^2 = 0.264$ . RTs were slightly slower in penalty conditions than no-penalty conditions,  $t(19) = -2.610$ ,  $p < 0.017$ , Cohen's  $d = -0.150$  (Tables 5.2 and 5.3). Movement time was computed as the difference between the time recorded when the selection was made (i.e.,

mouse button released at selection location) and the RT on a trial (Figure 5.3d). While there was no significant interaction between context and cost, there was a significant main effect of cost on MT,  $F(1,19) = 17.794$ ,  $p < 0.001$ ,  $\eta_p^2 = 0.484$ . In penalty conditions, MTs were significantly longer than in no-penalty conditions,  $t(19) = -4.218$ ,  $p < 0.001$ , Cohen's  $d = -0.289$  (Tables 5.2 and 5.3). Replicating our findings in Chapter 3, the analysis of RTs and MTs showed the participants took longer to initiate movements and make selections in penalty conditions.

### 5.3.3 Maximum and average velocity

By recording mouse cursor positions and button press and release times, we computed the maximum and average velocity of the mouse cursor movements during selections on each trial. There were no significant context x cost interaction or main effect of context on maxV or avgV, all  $F(1,19)s < 0.439$ , all  $ps > 0.515$ . We did see a significant main effect of cost on maxV at an uncorrected  $p < 0.05$ ,  $F(1,19) = 5.075$ ,  $p < 0.036$ ,  $\eta_p^2 = 0.211$ , and at the corrected threshold for avgV,  $F(1,19) = 17.678$ ,  $p < 0.001$ ,  $\eta_p^2 = 0.482$  (Figure 5.3e and f). Post hoc t-tests showed greater (faster) maxV,  $t(19) = 2.253$ ,  $p < 0.036$ , Cohen's  $d = 0.145$ , and avgV,  $t(19) = 4.201$ ,  $p < 0.001$ , Cohen's  $d = 0.296$ , in no-penalty conditions compared with penalty conditions (Tables 5.2 and 5.3). As expected, the faster velocities we observed parallel our MT findings, wherein longer MTs corresponded to slower movement during penalty conditions.

## 5.4 fMRI results

### 5.4.1 Whole-brain GLM results

As a first pass, we conducted a univariate GLM and group-level analysis on the contrasts to determine the extent to which regions across the entire brain were engaged by the task consistently across participants. The task-rest contrast showed significant (FDR-corrected  $q < 0.05$ ,  $p < 0.004$ ) levels of activity above baseline globally throughout the brain. As expected, we saw clusters of activation in left primary motor regions (participants did task with right hand), throughout the cerebellum, as well as the and visual cortex. We also observed contiguous clusters of activation in the putamen bilaterally, but not within either of the caudate nuclei. Small clusters of activation were observed in posterior and lateral regions of the left OFC, with multiple larger clusters distributed throughout the left DLPFC. Posterior parietal activity was left lateralized and primarily in regions of the inferior parietal lobule, including the angular and supramarginal gyri and intraparietal sulcus. Very little activation was present in the lateral regions of right parietal cortex. In addition to the areas where our a priori ROIs were located, we observed task-related activation in the brainstem, insula and amygdala bilaterally, as well as in large patches along the medial wall in anterior prefrontal cortex, and anterior and posterior cingulate cortex. Figure 5.5 shows a multislice axial view of the FDR-corrected map for the task-rest contrast. Overall, the task broadly engages a substantial number of regions across the brain at the cortical and subcortical levels, including the brainstem and cerebellum. Since none of the other contrasts yielded voxels that survived FDR correction, we will only report the location of the small number of voxels that were present using a threshold of  $p < 0.001$ . For the harm - help contrast, we found two very small clusters in the right caudate and right insula. Sparse

clusters throughout the cerebellum, along with very small clusters in the pulvinar of the right thalamus and in right insula, and a medial area of the right middle frontal gyrus were found in the penalty - no-penalty contrast. Lastly, the interaction contrast showed a small cluster of activation present in the right caudate as well as in the optic radiations bilaterally.

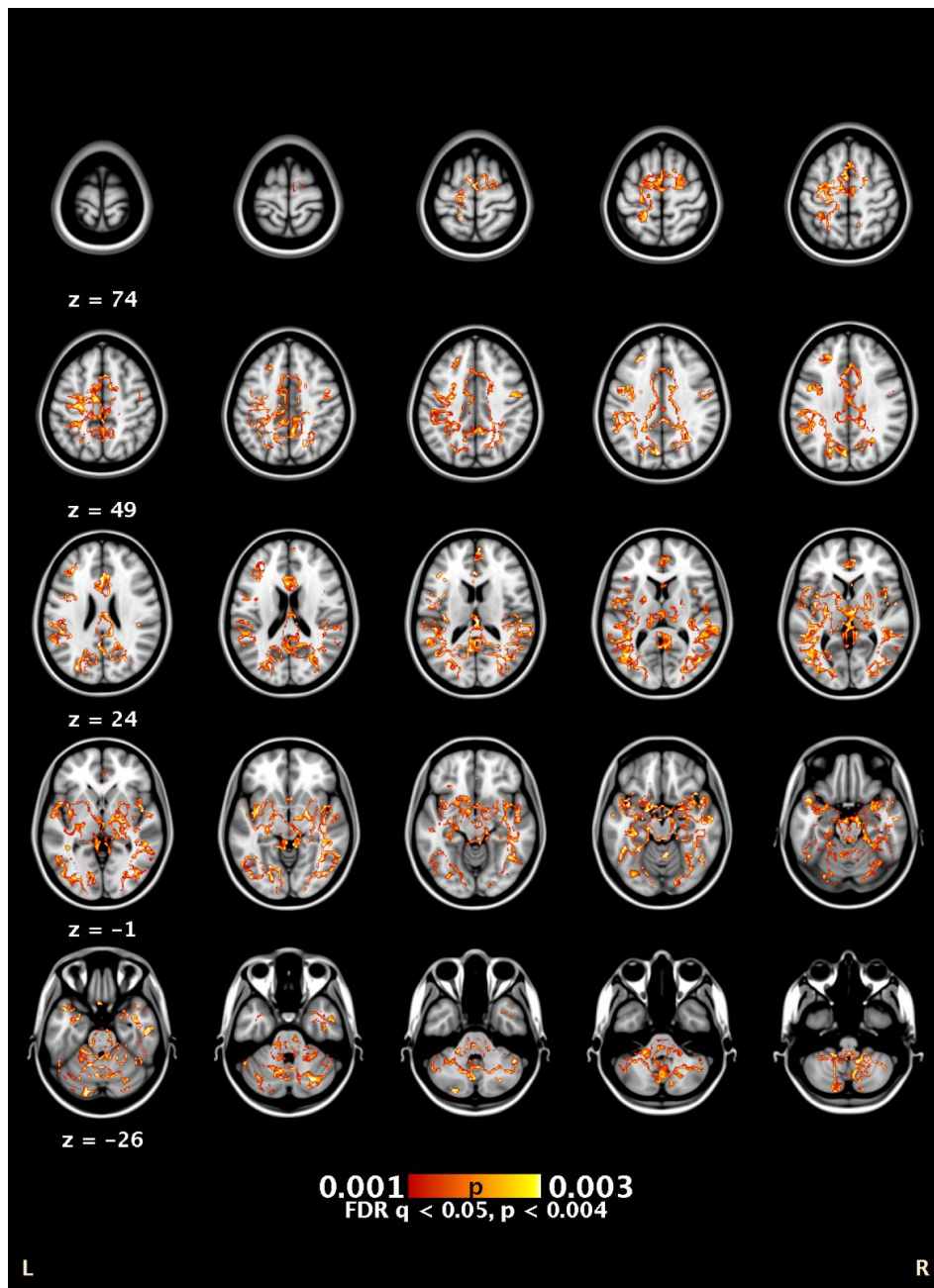


**Figure 5.5** GLM results: Map of significant task-related activation for the task - rest contrasts. A map of voxel activations that survived the FDR-corrected threshold  $q < 0.05$ ,  $p < 0.004$  is overlaid on an MNI template brain. In this map, darker orange colors correspond to lower p values, while lighter yellow and white colors indicate higher p values. All voxels shown here have  $p < 0.001$ . A large number of cortical, subcortical, cerebellar, and brainstem regions were significantly active during the task above baseline. We observed clusters of activation in left and right putamen and DLPFC, left OFC, and left PPC, confirming that several of our a priori ROIs were engaged by the task.

#### 5.4.2 ROI-based GLM contrast results

We report the group mean contrast values with standard errors for each ROI in Table 5.4 and the two-way repeated measures ANOVA results in Table 5.5. We observed a significant main effect of context in the left motor putamen,  $F(1,19) = 4.402$ ,  $p = 0.050$ ,  $\eta_p^2 = 0.188$ , wherein the magnitude of BOLD activation in harm conditions was positive and significantly greater than in help conditions where contrast values were negative, paired  $t(39) = 2.226$ ,  $p = 0.032$ , Cohen's  $d = 0.809$ . There was no significant main effect of cost, nor a significant context x cost interaction in the left motor putamen ROI. We also found a significant interaction between context and cost in the right precentral gyrus (i.e., primary motor cortex),  $F(1,19) = 7.612$ ,  $p = 0.013$ ,  $\eta_p^2 = 0.286$ . However, neither main effect of context or cost was significant in the right precentral gyrus ROI. In the harm context, contrast values are positive in no-penalty conditions, but negative in penalty conditions. This relationship is reversed in the help context: contrast values are negative in no-penalty conditions and positive in penalty conditions.

**Table 5.4** Contrast value means and standard errors by condition for all regions of interest

|                    |                      | Harm<br>No-Penalty |      | Harm<br>Penalty |      | Help<br>No-Penalty |      | Help<br>Penalty |      |
|--------------------|----------------------|--------------------|------|-----------------|------|--------------------|------|-----------------|------|
| Region-of-Interest |                      | M                  | SE   | M               | SE   | M                  | SE   | M               | SE   |
| <b>Left</b>        | <i>Caudate</i>       | 0.05               | 0.51 | 0.60            | 0.48 | -0.52              | 0.36 | -0.13           | 0.36 |
|                    | <i>Putamen</i>       | 0.01               | 0.41 | 1.01            | 0.45 | -0.62              | 0.54 | -0.40           | 0.44 |
|                    | <i>Motor Putamen</i> | 0.16               | 0.38 | 0.97            | 0.44 | -0.72              | 0.54 | -0.41           | 0.36 |
|                    | <i>OFC</i>           | -0.49              | 0.67 | 0.43            | 0.62 | 0.41               | 0.89 | -0.34           | 0.75 |
|                    | <i>PFC</i>           | -0.28              | 0.74 | 0.02            | 0.65 | 0.17               | 0.88 | 0.09            | 0.93 |
|                    | <i>PPC</i>           | -0.20              | 0.65 | -0.96           | 0.76 | 0.18               | 0.90 | 0.99            | 0.98 |
|                    | <i>Precentral</i>    | 0.82               | 0.64 | -0.82           | 0.45 | 0.15               | 0.77 | -0.16           | 0.80 |
|                    | <i>Caudate</i>       | 0.66               | 0.56 | 0.23            | 0.64 | -0.68              | 0.62 | -0.21           | 0.50 |
| <b>Right</b>       | <i>Putamen</i>       | -0.12              | 0.44 | 0.07            | 0.41 | -0.47              | 0.56 | 0.52            | 0.60 |
|                    | <i>Motor Putamen</i> | -0.09              | 0.46 | 0.96            | 0.48 | -0.66              | 0.43 | -0.21           | 0.39 |
|                    | <i>OFC</i>           | -0.39              | 0.67 | 1.07            | 0.68 | -0.62              | 0.70 | -0.06           | 0.69 |
|                    | <i>PFC</i>           | -0.45              | 0.55 | 0.43            | 0.49 | -0.41              | 0.80 | 0.43            | 0.77 |
|                    | <i>PPC</i>           | -0.93              | 0.79 | -0.83           | 0.71 | -0.43              | 0.88 | 2.18            | 1.10 |
|                    | <i>Precentral</i>    | 0.51               | 0.78 | -1.06           | 0.87 | -1.21              | 0.89 | 1.75            | 0.89 |

**Table 5.5** Two-way repeated measures ANOVA results on mean contrast values by condition

|                    |                      | Context     |        |            | Cost        |       |            | Context x Cost |        |            |
|--------------------|----------------------|-------------|--------|------------|-------------|-------|------------|----------------|--------|------------|
| Region-of-Interest |                      | F<br>(1,19) | p      | $\eta_p^2$ | F<br>(1,19) | p     | $\eta_p^2$ | F<br>(1,19)    | p      | $\eta_p^2$ |
| <b>Left</b>        | <i>Caudate</i>       | 1.903       | 0.184  | -          | 0.684       | 0.418 | -          | 0.031          | 0.863  | -          |
|                    | <i>Putamen</i>       | 3.676       | 0.070  | -          | 1.210       | 0.285 | -          | 0.590          | 0.452  | -          |
|                    | <i>Motor Putamen</i> | 4.402       | *0.050 | 0.188      | 1.345       | 0.261 | -          | 0.267          | 0.611  | -          |
|                    | <i>OFC</i>           | 0.011       | 0.918  | -          | 0.009       | 0.924 | -          | 0.744          | 0.399  | -          |
|                    | <i>PFC</i>           | 0.134       | 0.719  | -          | 0.011       | 0.917 | -          | 0.036          | 0.851  | -          |
|                    | <i>PPC</i>           | 1.492       | 0.237  | -          | <<1         | 0.980 | -          | 0.601          | 0.448  | -          |
|                    | <i>Precentral</i>    | <<1         | 0.993  | -          | 1.028       | 0.323 | -          | 1.238          | 0.280  | -          |
|                    | <i>Caudate</i>       | 1.427       | 0.247  | -          | <<1         | 0.975 | -          | 0.558          | 0.464  | -          |
| <b>Right</b>       | <i>Putamen</i>       | 0.007       | 0.933  | -          | 0.825       | 0.375 | -          | 0.568          | 0.460  | -          |
|                    | <i>Motor Putamen</i> | 2.431       | 0.136  | -          | 2.106       | 0.163 | -          | 0.431          | 0.520  | -          |
|                    | <i>OFC</i>           | 0.678       | 0.420  | -          | 1.305       | 0.268 | -          | 0.463          | 0.504  | -          |
|                    | <i>PFC</i>           | <<1         | 0.976  | -          | 0.876       | 0.361 | -          | <<1            | 0.978  | -          |
|                    | <i>PPC</i>           | 1.979       | 0.176  | -          | 1.920       | 0.182 | -          | 2.670          | 0.119  | -          |
|                    | <i>Precentral</i>    | 0.220       | 0.644  | -          | 0.523       | 0.478 | -          | 7.612          | *0.013 | 0.286      |

\* denotes significance at  $p < 0.05$ ; value for Left Motor Putamen is rounded up from  $p = 0.0495$  for table uniformity

#### 5.4.3 RSA Results

To determine whether any ROIs showed reliable differences in encoding unique levels of task conditions, we computed a summary statistic H over the  $\hat{d}$  values in the RDM for each ROI across all participants. The group mean H values and 95% confidence intervals are shown in Figure 5.5. We visualized the pattern distances for each pairwise condition comparison by constructing RDMs for each ROI. Since the RDMs are symmetric square matrices, the same pairwise distance comparisons are represented in the upper and lower triangles. The matrix

diagonal represents the distances between patterns of the same condition, which equal 0. Figure 5.5 shows the group mean RDMs for all of the striatal (Figure 5.5a) and cortical ROIs (Figure 5.5b). In each panel, the top row shows left hemisphere ROIs and right hemisphere ROIs in the bottom rows. The scales on the right of each panel show the colors that correspond to pattern distances reflected in each RDM. Darker (blue) colors represent smaller distances, indicating that patterns of activity within that ROI are very similar for the conditions being compared in a given cell in the RDM. Lighter (yellow) colors represent greater distances, indicating more dissimilar activity patterns for the conditions in a cell. Only the left putamen striatal ROI showed a significant nonzero H at the Bonferroni-corrected threshold  $\alpha = 0.005$ , right-tailed  $t(19) = 3.146$ ,  $p = 0.003$ , Cohen's  $d = 0.704$ . The left OFC ROI also showed a significant H at an uncorrected p value, right-tailed  $t(19) = 2.053$ ,  $p = 0.027$ , Cohen's  $d = 0.459$ . However, this did not survive the threshold of multiple comparisons correction. Neither were any of the other cortical or striatal ROIs significant at the  $p < 0.05$  level, all  $t(19)s < 1.399$ , all  $ps > 0.089$  (Table 5.6).

**Table 5.6** Group mean  $H$  values and one-sample t-test results for all ROIs

| ROI          |                      | $H$ mean | $H$ SE | t(19)  | p     | Sig. | Cohen's d |
|--------------|----------------------|----------|--------|--------|-------|------|-----------|
|              | <b>Caudate</b>       | 0.0028   | 0.004  | 0.657  | 0.260 | -    | -         |
|              | <b>Putamen</b>       | 0.0075   | 0.002  | 3.146  | 0.003 | ***  | 0.704     |
|              | <b>Motor Putamen</b> | -0.0013  | 0.004  | -0.315 | 0.623 | -    | -         |
| <b>Left</b>  | <b>OFC</b>           | 0.0083   | 0.004  | 2.053  | 0.027 | *    | 0.459     |
|              | <b>PFC</b>           | 0.0012   | 0.001  | 1.140  | 0.134 | -    | -         |
|              | <b>PPC</b>           | 0.0016   | 0.003  | 0.542  | 0.297 | -    | -         |
|              | <b>Precentral</b>    | 0.0004   | 0.002  | 0.281  | 0.391 | -    | -         |
| <b>Right</b> | <b>Caudate</b>       | 0.0040   | 0.010  | 0.414  | 0.342 | -    | -         |
|              | <b>Putamen</b>       | -0.0020  | 0.004  | -0.465 | 0.676 | -    | -         |
|              | <b>Motor Putamen</b> | 0.0020   | 0.004  | 0.462  | 0.325 | -    | -         |
|              | <b>OFC</b>           | 0.0031   | 0.004  | 0.813  | 0.213 | -    | -         |
|              | <b>PFC</b>           | 0.0002   | 0.001  | 0.149  | 0.442 | -    | -         |
|              | <b>PPC</b>           | 0.0003   | 0.001  | 0.262  | 0.398 | -    | -         |
|              | <b>Precentral</b>    | 0.0041   | 0.003  | 1.399  | 0.089 | -    | -         |

\*\*\* denotes Bonferroni-corrected  $\alpha = 0.005$  significance threshold. \* denotes uncorrected  $p < 0.05$ .

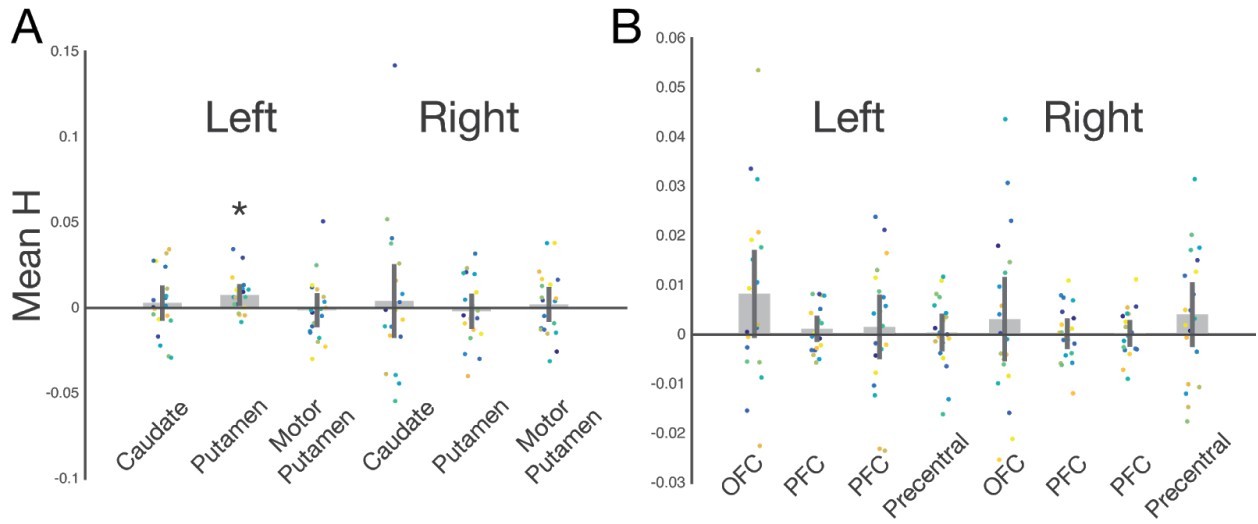


**Figure 5.4** Mean H statistic values. For each ROI (A - striatal, B - cortical), we plot the means (gray) and 95% CI error bars of the H statistic that was computed as an omnibus measure of condition-wise pattern distances between each pair of context and cost conditions. Each colored dot represents the H value for an individual participant. A positive H value indicates the presence of a significant pattern distance among the six pairwise condition comparisons, with greater H values corresponding to greater distances. We observed significant group-level pattern distances within the left putamen striatal convergence zone. The left OFC region also showed significant encoding at an uncorrected  $p < 0.05$ , but this result did not survive the Bonferroni-corrected multiple comparisons threshold of  $\alpha = 0.005$  (for all statistics, see Table 5.6).

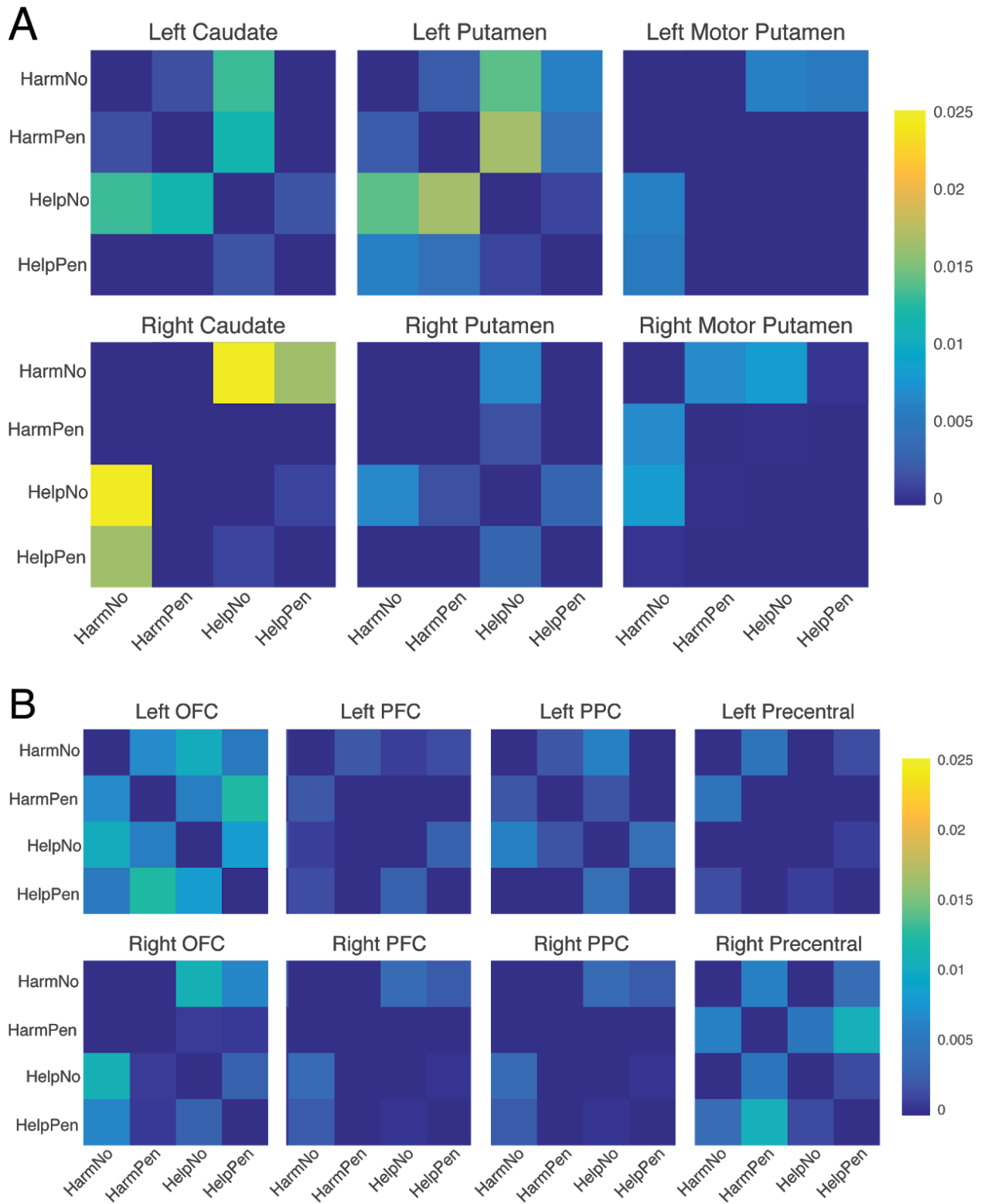


**Figure 5.5** Representational dissimilarity matrices (RDMs) for ROI-based analyses. Each RDM is a symmetric square matrix that shows the group mean cross-validated Mahalanobis distances between activity patterns for each pair of conditions for all ROIs. Values along the diagonal equal 0 (darkest/blue color) since there is no expected difference between activity patterns for the same condition. More similar patterns with positive distances closer to 0 are represented by dark/blue hues, while more dissimilar patterns with relatively larger positive distances (lightest/yellow colors) indicate that activity in a given region reliably distinguishes between a pair of conditions. The left putamen RDM (panel A, top middle) provides evidence that activity patterns in that ROI differentially represents harm and help conditions (four upper right quadrants) during the task with the largest distances between the help x no-penalty condition and both harm conditions. Also, H value for the left OFC ROI (panel B, top leftmost) was significant at the uncorrected  $p < 0.05$  level and shows marginal evidence for differential encoding of task conditions reflected by similar positive distances for all pairwise comparisons.

#### 5.4 Discussion

For the final experiment of this dissertation, we adapted our novel behavioral task, Drone Strike, to address Specific Aim 3 that examines whether neural representations within the striatum encode different levels of context and cost during spatial decision-making under risk. First, we replicate our previous behavioral findings (Chapter 2 and 3), to confirm that avoidant selection behavior is driven by penalties associated with non-target regions of spatial stimuli. Second, to the best of our knowledge, we provide the first evidence that an anterior striatal region associated with action-value (Pauli et al., 2016) represents distinct levels task context that frame cost outcomes on risky spatial decisions. Furthermore, we show that patterns of activity in a cortical region with direct structural and functional connectivity with the anterior striatum (Jarbo & Verstynen, 2015) also encodes levels of context and cost. Together, these findings highlight part of corticostriatal network that may show how the contextual framing of losses can impact

subjective value signals that drive avoidant selection behavior during risky spatial decision-making.

Behaviorally, our results followed the same pattern of results observed in Chapters 3, where the level of cost condition drove significant differences in selection behavior as measured by all dependent variables. Overall, selections were biased further away from the non-target under penalty conditions. We did not observe a significant main effect of context on selection bias, nor did we find a significant interaction between context and cost. However, we found that one participant exhibited selection behavior across context conditions that was more than three standard deviations away from the group mean. This indicates that the participant did not closely comply with task instructions and suggests that the small sample size used for this study was underpowered for detecting the context x cost interaction that we observed in larger behavioral study in Chapter 3. Indeed, an analysis of the behavioral data without that outlier participant showed a significant context x cost interaction, such that the greatest selection bias would be observed in the harm context with penalty conditions (see Section 5.3.1). Moreover, the presence of this replicated contextual framing effect in a small sample size demonstrates the robustness of the Drone Strike paradigm. In addition to increased bias, we found that selection variability also increased significantly in penalty conditions. This finding merits further investigation as it is not predicted by the maximum expected gain model that we used as a basis for our behavioral hypotheses, nor did we expect to see an increase in variability given that we did not manipulate target variance in this study. Regarding the initiation and execution of selections, we found that participants took longer to begin movements and complete selections while also moving slower overall during penalty conditions than no-penalty conditions. Taken together, the behavioral

findings further confirm that participants engage in more loss averse selection behavior during risky spatial decisions, replicating our results from Chapters 2 and 3.

Using a priori structurally and functionally connected ROIs, we identified an anterior striatal region that reliably distinguishes between levels of context and cost during risky spatial decision-making. In the striatum, the left putamen convergence zone showed patterns of activity that differentiated between harm and help contexts as well as no-penalty and penalty conditions (Figure 5.5a). Given the major role of the putamen in motor preparation and execution (Wolfram Schultz & Romo, 1992), it is not surprising to see significant task-related engagement of the putamen in general. However, we found that the motor putamen ROI that we used as a control region in our analyses did not differentiate between task conditions, despite having high degree of spatial overlap with the rostrally adjacent convergence zone. This provides strong support for our predicted finding that anterior striatal regions that are structurally and functionally connected to a broad set of prefrontal and parietal regions are associated with action-value (Pauli et al., 2016) and not simply motor preparation and execution as more posterior areas of the putamen that largely receive input from primary motor cortex.

Though we observed significant encoding of task condition differences in one of our a priori striatal convergence zones, we failed to find clear evidence of a corticostriatal network that represents distinct levels of context and cost during risky spatial decisions. Focusing on the fMRI results, we did have strong support for condition-specific encoding in the left putamen, and marginal evidence for the left OFC as well (Table 5.6, Figures 5.4 and 5.5). Even with reduced signal in OFC regions that, for the sake of uniform data preprocessing across all participants, we opted not to correct for, the left OFC region still showed encoding at uncorrected  $p < 0.05$  for all

pairwise conditions (Figure 5.5b). This particular finding is highly consistent with a large body of research showing that OFC is involved in encoding the subjective value of future rewards on both economic and action decisions (Arana et al., 2003; Gottfried, O'Doherty, & Dolan, 2003; Howard, Gottfried, Tobler, & Kahnt, 2015; Padoa-Schioppa & Assad, 2006; Windmann et al., 2006). However, as we discussed in detail in Chapter 1 (Section 1.4), this specific function of the OFC may work in concert with other prefrontal and parietal regions along with its connectivity to the striatum to contribute to value-based action selection (Domenech & Koechlin, 2015/2; Kahnt, 2017; Ridderinkhof et al., 2004).

Our observation of significant differences in task-related activation magnitude and patterns distributed broadly across cortical and striatal regions is consistent with previous evidence of lateralized motor control and execution processes. We found a significant increase in left motor putamen ROI activation in harm conditions (Table 5.5) along with significant pattern differences between harm and help contexts in the left putamen convergence zone (Table 5.6 and Figure 5.5a, top center). This finding is not surprising given that all participants used their right hands in the task and motor execution is largely driven by contralateral brain regions (Kim et al., 1993). However, the left putamen has been implicated in more sophisticated motor planning processes where unique levels of a task condition require different execution of planned actions (Kurniawan et al., 2010; Monchi, Petrides, Petre, Worsley, & Dagher, 2001; Monchi, Petrides, Strafella, Worsley, & Doyon, 2006). Additionally, we saw a significant context x cost interaction that drove activation magnitude differences in right precentral gyrus (Table 5.5), ipsilateral to the hand used in the task. Some research provides evidence that right precentral gyrus, i.e., right primary motor cortex, contributes to motor processes by halting ongoing actions and terminating

movements at a goal location (Mutha, Haaland, & Sainburg, 2012, 2013). Our current results also support previous findings that the motor planning and execution processes are not completely lateralized to the contralateral hemisphere and appear to be distributed across, at least, the left putamen and right precentral gyrus ROIs in this study. Given the null findings the PPC--an area largely implicated in spatial cognition (Burgess, 2008; Colby & Goldberg, 1999), we cannot say whether or not context or cost influenced spatial processes involved in our task. Together, these findings suggest that changes in task context that elicited significant activation differences in left putamen and right precentral gyrus may impact risky spatial decision-making by controlling the execution of planned actions to a targeted stimulus location.

In general, this study suffers from some limitations that we would like to address with future work that refines the processing and analyses of fMRI data. Most notably, this study is underpowered ( $N = 20$ ) for both the fMRI and behavioral measures we sought to evaluate. In the Drone Strike behavioral experiment (Chapter 3), we found a significant interaction between context and cost with an  $N = 44$ . But with fewer than half the participants in the present study, we failed to replicate that particular finding. A post hoc power analysis of the Danger Zone experiment (Chapter 2) showed that a minimum of 26 participants would be necessary to detect the significant interactions and main effects we saw in that study. Though the context manipulation used here is obviously qualitatively different than manipulating target stimulus variance, increasing our sample size to a minimum of 26 may result in more robust findings in the behavioral and fMRI versions of the task. This may also be due, in part, to having to complete the task in the scanner in a constrained, supine position along with differences in

hardware responsiveness (e.g., cursor lag in optical mouse) and viewing stimuli through a mirror that could affect performance compared to a typical testing room environment.

Regarding fMRI analyses, our interpretation of condition-specific differences based on the RDMs is primarily qualitative. Though the H values indicate the presence of significant pairwise condition distances in each RDM, this omnibus measure does not indicate which subset of condition comparisons show the greatest differences. As such, it is unclear which condition levels are differentially represented in each ROI. Additional analyses on the distance measures will be able to confirm representational differences to a finer degree, and we can extend our inferences further to comparisons of the RDMs themselves (Kriegeskorte et al., 2008; Nili et al., 2014) to identify networks of regions that are encoding task conditions in similar ways. Another reason why we may have failed to observe significant encoding differences, particularly in the cortex, is that the cortical ROIs spanned large swaths of cortex in DLPFC and PPC. In both the DLPFC and PPC, functional activity has been associated with myriad cognitive processes that may contribute to noise in our distance estimates. Follow-up work on this project can address limitations in our fMRI analyses in a number of ways, including: 1) a parcellation of the cortical ROIs into smaller regions defined *a priori* by structural or functional connectivity, 2) by using a data-driven approach like independent components analysis (Calhoun, Liu, & Adali, 2009) to identify networks of spatially distributed brain regions that share task-related time courses of activity, or 3) by performing a whole brain searchlight RSA (Kriegeskorte et al., 2006; Nili et al., 2014) that parses the entire brain with an ROI of a predetermined size to locate regions that show significant pattern distances as well as similar RDMs. By implementing any, or all, of these approaches can provide additional evidence for a set of brain regions that are representing

distinct levels of a task--in our case, a decision-making task with contextual framing of risk--in the same way. Combining that task-based information with known corticostriatal connectivity would clearly elucidate an integrative brain network that uses subjective value to drive action selection.

## 5.5 Conclusion

Our initial analyses of the MRI version of Drone Strike provide evidence that a putative action-value region of the striatum, the left putamen, reliably distinguishes between levels of context and cost during risky spatial decisions. Taken together with our identification of this region as convergence zone of corticostriatal connectivity, these findings suggest that the left putamen may serve as a hub that integrates contextual information with costs to represent the subjective value of spatial targets to impact action selection behavior. Importantly, this work highlights a locus of structural and functional connectivity wherein explicit contextual information that shapes subjective value signals can penetrate implicit sensorimotor integration processes involved in value-based decision-making in humans.

# **Chapter 6**

## **Conclusions and future directions**

With this dissertation, I set out to address three specific aims geared toward gaining insight to the neural mechanisms of human decision-making under risk. First, we developed a novel behavioral task that demonstrated that the interplay between sensory uncertainty and costs drives loss avoidant behavior, particularly when sensory information about the target of an action becomes less reliable. Next, we adapted that task by superimposing the narrative of a wartime scenario, allowing us to observe a subtle but significant effect of contextual framing on risky decision-making. Namely, the kind of loss that someone believes they will incur on a risky decision that has a harmful side effect leads to an increased avoidance and more cautious action execution than when the decision outcomes are subjectively less harmful. Together, our behavioral studies show that people will behavior in a manner that foregoes the maximization of expected gain in order to avoid a potential loss. To begin to gain an understanding the neural underpinnings of these ostensibly complex cognitive processes, we identified structural and functional corticostriatal connectivity that we believe can serve as an integrative locus for incorporating sensory estimates, action selection, and subjective value during risky decisions. Leveraging our behavioral task, the final experiment of this dissertation supplies an initial, novel finding that the anterior putamen together with orbitofrontal cortex differentially encodes distinct levels of contextual framing and costs to represent the subjective value of an action decision outcome. In all, the experiments presented in this dissertation incrementally build on one another

to link multiple theories of decision-making with multimodal neuroimaging approaches to elucidate a mechanism for integrating subjective value and action selection under risk.

## 6.1 Contributions of individual studies

### 6.1.1 Extended predictions of the maximum expected gain model

In Chapter 2, I evaluated a previously untested prediction of the maximum expected gain model on selection behavior by developing and implementing a novel risky spatial decision-making task (Danger Zone). The study showed that people attempted to mitigate potential losses by selecting significantly farther away from the penalizing non-target in high variance conditions, when the location of the target mean was more difficult to estimate. Additionally, reaction times (i.e., time to initiate movement) across trials were significantly slower in high variance conditions, suggesting that participants either 1) spent a longer time estimating the location of the target mean or 2) intentionally withheld movement initiation due to decreased confidence in their estimates. Since the results presented in this dissertation, nor previous studies that employed the maximum expected gain model, did not closely examine experimental effects on reaction time, future research can focus on disentangling the computational and motivational processes that underlie reaction time behavior during risky spatial decisions. Regardless, the findings presented in Chapter 2 extend the application of the maximum expected gain model to exploring spatial decision-making behavior under varying degrees of sensory uncertainty, rather than constraining the model's predictions to loss avoidance based on the spatial proximity of the target and the non-target.

### 6.1.2 Elucidated contextual effects of risky spatial decision-making

Chapter 3 presents the results of a novel adaptation of Danger Zone that provide evidence that the contextual framing of a risky spatial decision impacts the extent to which people avoid different kinds of losses. To explore how contextual framing affects selection behavior, the instructions for Drone Strike superimposed two wartime scenarios as separate contexts that framed target selection decisions as different kinds of moral dilemmas. Participants were tasked with either selecting the location for a drone strike on enemies or delivering ammunition to allies whose positions were demarcated by dots, similar to Danger Zone. In no-penalty conditions, the non-target dots represented trees, but represented the nearby locations of allies on drone strike trials and enemies on delivery trials. Though people biased their selections away from the penalizing non-target in both scenarios, this bias was significantly greater on drone strike than delivery trials indicating that the kind of potential loss incurred on a risky decision impacts how much people attempt to avoid that loss. Also, strikingly, the magnitude of the context effects on bias observed in Drone Strike was three times greater than in Danger Zone, which strongly suggests that the contextual framing of losses influences spatial decision-making processes.

Broadly, as discussed in Chapter 2, loss aversion during risky economic decisions in a central principle of Prospect Theory, which attributes choice behavior that minimizes potential loss as a subjective response to the risk of “losses looming larger than gains” (Kahneman & Tversky, 1979). Building on the findings presented in Chapters 2 and 3 opens up an intriguing avenue for developing the maximum expected gain model in concert with specific facets of Prospect Theory to test novel predictions about how different types of contextual factors can amplify loss avoidance during risky decisions.

Critically, by incorporating affectively valenced scenarios into task narratives, the general of spatial decision paradigm used in Drone Strike can be used examine subjective aspects of risky decision-making processes that impact action selection behavior. Now, consider the contrast between Drone Strike (Chapter 3) and Danger Zone (Chapter 2), wherein the primary difference between the tasks was the kind of collateral costs incurred in penalty conditions that participants decided how much to avoid, i.e., ally casualties versus points lost. In either case, the “optimal” solution on any trial type was to select the center of the target dots in order to maximize expected gain by neutralizing as many enemies as possible or scoring as many points as possible. Though posed as moral dilemmas, without the superimposed narrative, Drone Strike can be interpreted as an otherwise non-moral, risky economic decision task, like Danger Zone.

#### 6.1.3 Linked moral choice to risky spatial decision-making

From a moral psychology and philosophy perspective, the process of maximizing expected gain runs ostensibly parallel to a moral reasoning process that individuals may engage in to make action decisions under risk. For instance, dilemmas like the “trolley problem” or “footbridge problem” (Greene et al., 2001) are standard paradigms in moral psychology and experimental philosophy studies that examine moral reasoning about risky decisions. In these cases, the “right” choice in the “trolley problem” could be equivalent to the “optimal” solution yielded by a simple model or equation that maximizes gain, e.g., saving five people by killing one. However, in “trolley problem” cases where the one person who will be killed is a close friend or significant other compared with five strangers, choice behavior is altered particularly for individuals who would willingly sacrifice five strangers to save a loved one. While choosing to save one over five

fail to maximize expected gain in a strict Utilitarian sense, does not necessarily mean that the choice was morally wrong.

In Drone Strike, the moral reasoning used by a very strictly Utilitarian individual might lead them to accept that some loss in the form of instrumental harm to allies must happen if their selection is to maximize net gain, in terms of a larger ratio of enemy to ally casualties. However, a less Utilitarian individual may desire to avoid ally casualties altogether, which comes at the expense of neutralizing as many enemies as possible. So, even though incurring some ally casualties in “optimal” in a purely economic or computational sense, is it necessarily “right” in a moral sense? Conversely, is it then morally wrong to save allies if it means your decision failed to maximize enemy casualties? This highlights an important notion that subjective influences can result in biased behavior during risky decisions that appear to be suboptimal when considered within more strict interpretations of Utilitarian moral reasoning and optimal/statistical decision theory where maximizing expected gain is the “right” or “optimal”. Thus, the impact of subjective perceptions based on the contextual framing of losses should be accounted for when evaluating the outcomes and processes involved in risky decision-making to describe action selection behavior. Also, studying how people make decisions that involve moral reasoning about what someone ought to do when moral considerations (e.g., potential ally casualties on a drone strike) are relevant to a goal-direction action decision (e.g., maximizing enemy casualties on each drone strike in order to win a war) can provide insight to moral intuitions or beliefs about intent (Knobe, 2003b), and right and wrong actions (Sinnott-Armstrong, 2008). More deeply characterizing the similarities and distinctions between moral reasoning and risky

economic decision-making processes that drive action selection can guide the exploration of neural mechanisms that support those processes.

#### 6.1.4 Identification of action-value connectivity in the human brain

By combining resting state functional connectivity analysis and diffusion weighted imaging and fiber tractography, we confirmed and validated the structural and functional connectivity of a network that may integrate information during risky decision-making. More specifically, we demonstrated for the first time *in vivo* in humans, that afferent white matter projections from three disparate regions of cortex: DLPFC, OFC, and PPC, converged within contiguous clusters of voxels within both nuclei of the striatum bilaterally. A large body of histological research in nonhuman primates extending back several decades has helped to thoroughly characterize the topography of the striatum. The evidence for overlapping, convergent projections from multiple regions of the cortex was overwhelmingly clear in nonhuman primates, but it only became possible to map those projects in living human brains at high resolution in the 2000s, with the advent of tractography based on diffusion weighted imaging. The corpus of tracer studies along with dissections of brains from cadavers contributed to the establishment of a “ground truth” or “gold standard” by which the accuracy of diffusion imaging and tractography methods could map the brain. A critical aspect of the study presented in Chapter 4 is that we leveraged the ground truth neuroanatomy to infer the directionality of connectivity, and thus flow of information, of a set of streamlines from the cortex into the striatum. With diffusion imaging and tractography alone, there is no way to know which streamline endpoints correspond to the source or destination of the neural signals that traverse them. Many regions of the brain also exhibit a

high degree of bidirectional connectivity. That said, both retrograde and anterograde tracers can confirm directionality, and have long shown that the striatum, as the primary input to the basal ganglia, only receives projections from the cortex. This together with its centralized location within the brain, makes the striatum an ideal location for an integrative hub of information from disparate regions of cortex that play different roles in complex cognitive processes. In Chapter 4, we focused specifically on providing clear evidence for a three-way convergence of DLPFC, OFC, and PPC projections that had not been observed even in nonhuman primates, despite findings of all pairwise combinations of those regions. Our study confirmed that connectivity and was highly consistent with contemporary human neuroimaging work that localized the striatum within functionally connected prefrontal, orbitofrontal, and parietal regions. In all, the identification of these convergence zones is a strong contribution to research focusing on corticostriatal connectivity as a mechanism of information integration in a wide array of cognitive processes.

Soon after the work in Chapter 4 was published, a large meta-analysis of human functional neuroimaging data had pinpointed the striatum as an action-value region of the brain. In particular, anterior regions of the caudate nucleus and putamen were broadly implicated in tasks that involved the use of value-based feedback on action decisions. For the so-called action-value striatal regions to live up to their namesake, the striatum must, at minimum, integrate information about action selections together with perceptual information about the targets of those actions. This perceptual information can be based purely on estimates of sensory reliability, e.g., locating the spatial position of a target stimulus amidst visual noise, but subjective value signals can also be incorporated into action selection decisions, leading to biases

in behavior--as we showed in Chapters 2 and 3 along with substantial research on sensorimotor integration. Recent research in humans and nonhuman primates make a strong case for the OFC's role in representing the subjective value of multiple choices. Separate lines of research suggest that these value representations underlie action decisions via integrative processes that involve goal and action representations in dorsolateral prefrontal regions. However, the choices and action decisions under study in this research are still based largely on more purely economic choices, like taking a gamble over a lottery, or grape juice over water. Even at the level of the striatum, the focus is largely on feedback signals and learning, but less so on executing an action based on how valuable an individual deems a target to be. Thus, a glaring gap that few research tracks attempt to address is the neural mechanism by which integration of subjective value signals into sensorimotor decision-making processes happens. By developing Danger Zone into Drone Strike and adapting it for fMRI, we were able to explore the functional activity of a network of brain areas associated with the component processes that constitute risky decision-making. Our aim was to determine whether this structurally and functionally connected set of regions including OFC, DLPFC, PPC, and anterior striatum would actually show task-related functional connectivity as well as distinct representations of context and cost on risky spatial decisions. Indeed, this preliminary investigation has yielded promising early findings that indicate subjective value signals based on the contextual framing on costs on a risky decision can penetrate action selection processes via representations of task-related information in the OFC and anterior putamen.

## 6.2 Limitations of the current work

Though these early findings are exciting, there are still limitations to the studies presented in this dissertation that would make the overall work more comprehensive. One concern deals with the issue of power in the behavioral and fMRI studies. Only 20 datasets each were included in the final samples for Danger Zone and Drone Strike fMRI. Post hoc power analyses indicate that a minimum of 26 participants are needed to observe the behavioral effects we found in the 2x2 within-subjects study designs. On one hand, whether or not our studies were underpowered, there is little doubt about the general robustness of the paradigm we developed. That Danger Zone was readily adapted to carry out the Drone Strike task is also an early testament to its flexibility to test a variety of cognitive, moral, and social phenomena related to decision-making under risk or uncertainty. However, the effects of context, in particular, were very subtle and bordered marginal significance in both the behavioral and fMRI versions of Drone Strike. For instance, it was not clear that we would have even observed a context effect in the behavioral version when we scaled up to a 2x2x2 within-subjects design. Even though it paid off, working under an assumption that doubling N, rather than conducting a formal power analysis, was a risk that ought to be considered for planning future studies. Also, the addition of a moral dilemma increased the complexity of the study beyond the mere introduction of new independent variable. As we discuss in this chapter as well as in Chapter 3, decisions during moral dilemmas may rely on processes of rational moral reasoning, moral intuition, and ethical dispositions. All of these factors are difficult to control for--even in nonmoral cases, and require extremely careful consideration during stimulus design, developing task instructions, and interpretation of the

findings. Fortunately, some survey data on participants' decision styles and approaches as well as ethical beliefs and dispositions have been acquired and will be a focal point for future studies.

Another lingering concern about this work as a whole, is our shortcomings in regard to developing a computational model to describe behavior on these tasks. I have certainly come to appreciate the elegance of the maximum expected gain model and its ability to predict sensorimotor behavior in risky contexts simply by accounting for estimates of sensory noise and internal motor variability. We could have used the model as is to predict participant behavior on our novel experimental task or developed it further to look more specifically at contextual framing effects. As it stands, the  $\alpha$  term in the model carries all the weight (no pun intended) in driving bias away from a penalizing spatial location; however, the nature of  $\alpha$  is still very unclear. In particular, virtually none of the studies reviewed for this dissertation and the development of the projects herein have explicitly studied  $\alpha$  and whether it is tracking more than feedback signals. The fact that participants can readily shift their aim in order to avoid penalties on ballistic reaching tasks by simply receiving a cue to penalty conditions is direct evidence that  $\alpha$  is not all about feedback. With future work, I hope to delve more deeply into this curiosity. A bonus of developing a computational model for risky decisions is that parameters like  $\alpha$  can be used in fMRI analyses as parametric regressors that track fluctuations in neural activation or even specific patterns of activity across different brain regions or networks that distinguish between levels of context and cost as in the Drone Strike study. Ideally, this computational model would be a great leap forward in linking brain activity to observable behavior to more fully characterize cognitive processes.

### 6.3 Toward a causal mechanism of risky spatial decision-making

Risky spatial decisions can deviate from the predictions of models based on estimates of objective value and spatial variance. Mechanistically, the maximum expected gain model (Trommershäuser et al., 2003b) determines an optimal selection location by combining the values associated with spatial locations in the target (reward/gain) and non-target (penalty/loss) regions of a visually-presented stimulus. In previous risky spatial decision studies gain and loss were uniform throughout the target and non-target regions, respectively, and the amount of target and non-target overlap was manipulated across trials (Gepshtain et al., 2007; Neyedli & Welsh, 2013, 2014; Trommershäuser et al., 2006, 2003a, 2003b; Wu et al., 2006). In no-penalty conditions, the target center was the optimal selection location. However, under penalty conditions, the maximum expected gain location within the target was shifted away from the penalizing non-target, and thus the target center. In a critical difference between our work and previous studies, we disassociated value from spatial variance in the Danger Zone study (Chapter 2) so that the maximum expected gain location was always the target center. Despite knowing this, individuals still biased their selections in penalty conditions (see Section 2.3 and Figure 2.3) when we should not have observed significant selection bias in any condition. Also, since high spatial variance alone did not result in significant avoidance of the non-target in no-penalty conditions, the risk of penalty seems to be a necessary and sufficient cause of selection bias. So, when information about objective value and spatial variance conflict, people rely on value, resulting in biased selections that do not strictly maximize expected gain.

If people are not truly maximizing expected gain based on objective value, then how else might they be making selection decisions? (To disambiguate terminology, *reward* corresponds to

a score obtained on a selection on a Danger Zone trial: The maximum expected reward location is the target center across all conditions. *Gain* corresponds to the score obtained for selecting the optimal location predicted by the maximum expected gain model. The maximum expected gain location is the target center in no-penalty conditions, but is shifted away from the non-target in penalty conditions.) Importantly, we found that selection bias was not significantly different from zero in no-penalty conditions indicating that participants were capable of selecting the target center and, therefore demonstrated that they could maximize expected reward, even in penalty conditions. Despite that, participants selected *neither* the maximum expected reward or gain locations in penalty conditions, suggesting that participants were not objectively optimizing selections according to the maximum expected gain model or feedback based on our reward scoring function. Instead, participants made selections that were not completely risk seeking (closer to the target center) or risk averse (closer to the maximum expected gain location) in penalty conditions, as evidenced by selection bias measures observed approximately halfway between the target center and the maximum expected gain location. For one, this observation is consistent with the notion of satisficing, wherein selection behavior is constrained in order to perform “well enough”, but not necessarily optimally, to meet task goals (Jarvstad et al., 2014; Todd & Gigerenzer, 2000). Our findings in both the Danger Zone and Drone Strike (Chapters 3 and 5) studies suggest that participants misrepresented the objective value of  $\alpha$  (see *Equation 2.1*) by evaluating and incorporating feedback in a way that drove selection behavior that satisfied with respect to reward rather than optimized gain. In other words, people assigned *subjective value* to locations during risky spatial decisions to obtain greater, but not maximum, reward while mitigating potential loss on selection outcomes. It follows that how individuals

subjectively evaluate the reward and penalty associated with of a risky spatial decision outcome impacts how the decision is made.

To confirm whether subjective value impacted selection behavior based on idiosyncratic interpretations of reward and penalty, we manipulated the contextual framing of a risky spatial decision in the Drone Strike study. Experimental philosophy research has shown that moral dilemmas, like choosing whether to kill versus let die, strongly influence how people evaluate risky decisions, making differences in contextual framing effects a powerful way to probe decision-making mechanisms (Knobe, 2003b; Sinnott-Armstrong, 2008). We intervened on the decision-making process we observed in Danger Zone that resulted in selection bias away from the non-target, by superimposing a wartime scenario on the spatial decision. In particular, in the harm context in penalty conditions, loss corresponded to ally casualties incurred on an attempted drone strike on nearby enemies. On trials in the help context in penalty conditions, ammunition deliveries to allies intercepted by nearby enemies constituted a loss. Importantly, all visuospatial characteristics of the target and non-target stimuli *and* the scoring function remained the same across harm and help contexts while only the instructions to neutralize enemies or delivery ammunition to allies differed between conditions. Therefore, the only difference between contexts is the *kind* of loss that participants believed would be incurred on their selection decisions. In this case, we expected that participants would evaluate ally casualties as a subjectively more aversive type of loss, and that this subjective valuation should be reflected in a greater selection bias under penalty conditions within the harm context. That exact finding provided evidence that contextual framing amplifies loss avoidant selections and contributes to subjective estimates of value during risky spatial decisions. Taken together with the Danger Zone

findings, the ultimate goal of risky spatial decision-making is to create a representation of relative subjective value that corresponds to locations that constitute a spatial stimulus, i.e., a *spatial priority map*. Namely, the representation of subjective value is the *priority* component of the spatial priority map that can be used to shape goal-directed motor plans to a spatial location associated with high subjective value.

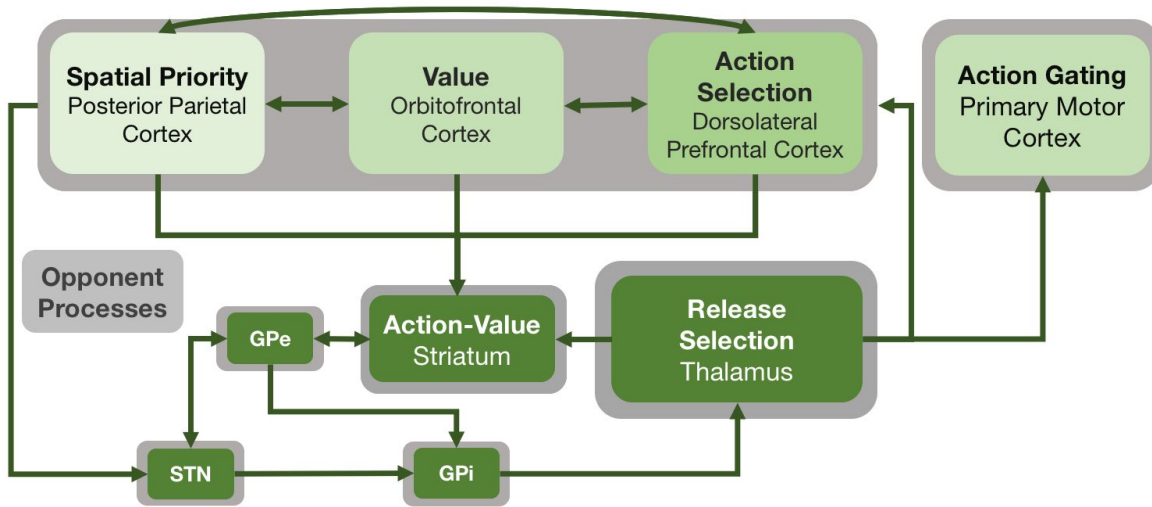


**Figure 6.1** Figure 1.2 revisited. Process model of a neural mechanism for risky spatial decision-making.

In Chapter 1, we introduced a model that illustrates the neural circuitry that may be involved in the psychological component processes that underlie risky spatial decision-making (Figure 1.2 depicted again above). Though we specifically predicted that the striatum would integrate spatial, subjective value, and action selection information from PPC, OFC, and DLPFC, respectively, we did not find evidence for the complete neural mechanism that we hypothesized in the Drone Strike fMRI study (Chapter 5). However, those findings do provide some insight about the effect of context on value representations and the execution of goal-directed movements during risky spatial decisions. For instance, left OFC showed differences in

activation patterns across task conditions (Table 5.6 and Figure 5.5b, bottom left), that is largely consistent with evidence that OFC activity represents the relative subjective value of multiple choices during decision-making (Murray & Rudebeck, 2018; Padoa-Schioppa & Conen, 2017). In terms of motor execution, the left putamen showed significant differences in context encoding in the convergence zone ROI (Table 5.6 and Figure 5.5a, top center) as well as a significant main effect of context in the motor putamen ROI (Table 5.5) and its more established role in motor planning and execution (Alexander & Crutcher, 1990; Schultz & Romo, 1992; Schultz & Romo, 1992). Additionally, we observed a significant interaction between context and cost on activation in the right precentral gyrus ROI (Table 5.5) that is consistent with research showing that right motor cortex is involved in updating actions in progress and stopping movements at targeted locations (Mutha et al., 2012, 2013). To explore the mechanistic relationship between the function of left OFC and putamen, and right precentral gyrus and selection behavior, studies could be conducted with patients with lesions to these areas as they performed the Drone Strike task. In patients with OFC damage, we would expect that patients would demonstrate more variable selection bias in harm and help conditions, indicating noisier representations of value associated with spatial locations (e.g., “credit assignment”) (Murray & Rudebeck, 2018; Walton, Behrens, Noonan, & Rushworth, 2011) or impaired risk (Hsu, Bhatt, Adolphs, Tranel, & Camerer, 2005; O’Neill & Schultz, 2013) or subjective value comparison abilities (Raghuraman & Padoa-Schioppa, 2014; Wallis, 2007). Regarding motor control and execution, individuals with left putamen damage would be expected to show no differences in the execution of movements across context conditions (e.g., similar movement times and velocities in harm and help conditions). Such a finding would be consistent with previous work where switching

between distinct levels of task context required different planned movements (Kurniawan et al., 2010; Monchi et al., 2006). In a hypothetical spatial decision-making study of individuals with damage to right precentral gyrus, we would expect to see increased selection variability that corresponds to an impaired ability to terminate goal-directed movements at a targeted location (Mutha et al., 2013). While these findings point to an explanation of how OFC, putamen, and right primary motor cortex impact value-guided movements during risky spatial decisions, we did not find any evidence of context effects on DLPFC, PPC, or caudate activity that would have allowed us to more fully characterize the neural mechanism of representing a spatial priority map and action selection that our process model predicts.

#### 6.4 Concluding remarks

Reflecting on this dissertation as a whole, I believe there is a solid foundation to pursue the development of behavioral, neuroimaging, and computational modeling approaches to understanding the mechanisms of value-based decision-making. A key question that I have tried to address with this work is how a mechanism of cognitive penetration would function, if it existed, during decision-making. In other words, how does external information that frames the outcome of an implicit process come to influence the implicit process itself prior to feedback? One clue seems to lie in the observation of idiosyncratic behavior when a decision with one objective outcome is framed in a way that leads the choice itself to be perceived in a subjectively different way. This is not dependent at all on feedback, and in fact many kinds of risky decisions studied in the literature only require objective estimates of sensory, or economic information. However, people still generate internal representations of expected feedback on a choice that are

based, in part, on external information. I think my final study in particular provides good evidence of that claim by showing contextual framing impacts avoidant behavior for the kinds of losses that individuals believe are subjectively worse than others. Now, the next big question I think I have to address is whether or not people make biased decisions because subjective perceptions of value, or their subjective perceptions of the decision-making context itself.

# References

*In alphabetical order*

- Alexander, G. E., & Crutcher, M. D. (1990). Preparation for movement: neural representations of intended direction in three motor areas of the monkey. *Journal of Neurophysiology*, 64(1), 133–150. Retrieved from <https://www.ncbi.nlm.nih.gov/pubmed/2388061>
- Alexander, G. E., DeLong, M. R., & Strick, P. L. (1986). Parallel organization of functionally segregated circuits linking basal ganglia and cortex. *Annual Review of Neuroscience*, 9, 357–381. <https://doi.org/10.1146/annurev.ne.09.030186.002041>
- Anderson, R. C., & Pichert, J. W. (1978). Recall of previously unrecallable information following a shift in perspective. *Journal of Verbal Learning and Verbal Behavior*, 17(1), 1–12. [https://doi.org/10.1016/S0022-5371\(78\)90485-1](https://doi.org/10.1016/S0022-5371(78)90485-1)
- Arana, F. S., Parkinson, J. A., Hinton, E., Holland, A. J., Owen, A. M., & Roberts, A. C. (2003). Dissociable contributions of the human amygdala and orbitofrontal cortex to incentive motivation and goal selection. *The Journal of Neuroscience: The Official Journal of the Society for Neuroscience*, 23(29), 9632–9638. Retrieved from <https://www.ncbi.nlm.nih.gov/pubmed/14573543>
- Averbeck, B. B., Lehman, J., Jacobson, M., & Haber, S. N. (2014). Estimates of projection overlap and zones of convergence within frontal-striatal circuits. *The Journal of Neuroscience: The Official Journal of the Society for Neuroscience*, 34(29), 9497–9505. <https://doi.org/10.1523/JNEUROSCI.5806-12.2014>
- Badre, D., & Frank, M. J. (2012). Mechanisms of Hierarchical Reinforcement Learning in

Cortico–Striatal Circuits 2: Evidence from fMRI. *Cerebral Cortex*, 22(3), 527–536.

<https://doi.org/10.1093/cercor/bhr117>

Balleine, B. W., & O’Doherty, J. P. (2010). Human and rodent homologies in action control: corticostriatal determinants of goal-directed and habitual action.

*Neuropsychopharmacology: Official Publication of the American College of*

*Neuropsychopharmacology*, 35(1), 48–69. <https://doi.org/10.1038/npp.2009.131>

Barbas, H. (2000). Connections underlying the synthesis of cognition, memory, and emotion in primate prefrontal cortices. *Brain Research Bulletin*, 52(5), 319–330. Retrieved from <https://www.ncbi.nlm.nih.gov/pubmed/10922509>

Bastian, A., Riehle, A., Erlhagen, W., & Schöner, G. (1998). Prior information preshapes the population representation of movement direction in motor cortex. *Neuroreport*, 9(2), 315–319. Retrieved from <https://www.ncbi.nlm.nih.gov/pubmed/9507975>

Battaglia, P. W., & Schrater, P. R. (2007). Humans trade off viewing time and movement duration to improve visuomotor accuracy in a fast reaching task. *The Journal of Neuroscience: The Official Journal of the Society for Neuroscience*, 27(26), 6984–6994. <https://doi.org/10.1523/JNEUROSCI.1309-07.2007>

Beck, J. M., Ma, W. J., Pitkow, X., Latham, P. E., & Pouget, A. (2012). Not noisy, just wrong: the role of suboptimal inference in behavioral variability. *Neuron*, 74(1), 30–39. <https://doi.org/10.1016/j.neuron.2012.03.016>

Bejjanki, V. R., Knill, D. C., & Aslin, R. N. (2016). Learning and inference using complex generative models in a spatial localization task. *Journal of Vision*, 16(5), 9. <https://doi.org/10.1167/16.5.9>

- Berger, J. O. (1985). *Statistical Decision Theory and Bayesian Analysis*. (S. Fienberg, J. Gani, K. Krickeberg, J. Berger, & B. Singer, Eds.). New York: Springer-Verlag New York, Inc.
- Berniker, M., & Kording, K. (2011). Bayesian approaches to sensory integration for motor control. *Wiley Interdisciplinary Reviews. Cognitive Science*, 2(4), 419–428.  
<https://doi.org/10.1002/wcs.125>
- Beukema, P., Diedrichsen, J., & Verstynen, T. (2018). *Binding during sequence learning does not alter cortical representations of individual actions*. *bioRxiv*.  
<https://doi.org/10.1101/255794>
- Bond, K. M., & Taylor, J. A. (2015). Flexible explicit but rigid implicit learning in a visuomotor adaptation task. *Journal of Neurophysiology*, 113(10), 3836–3849.  
<https://doi.org/10.1152/jn.00009.2015>
- Brainard, D. H. (1997). The Psychophysics Toolbox. *Spatial Vision*, 10(4), 433–436. Retrieved from <https://www.ncbi.nlm.nih.gov/pubmed/9176952>
- Buneo, C. A., & Andersen, R. A. (2006). The posterior parietal cortex: sensorimotor interface for the planning and online control of visually guided movements. *Neuropsychologia*, 44(13), 2594–2606. <https://doi.org/10.1016/j.neuropsychologia.2005.10.011>
- Burgess, N. (2008). Spatial cognition and the brain. *Annals of the New York Academy of Sciences*, 1124, 77–97. <https://doi.org/10.1196/annals.1440.002>
- Calhoun, V. D., Liu, J., & Adali, T. (2009). A review of group ICA for fMRI data and ICA for joint inference of imaging, genetic, and ERP data. *NeuroImage*, 45(1 Suppl), S163–S172.  
<https://doi.org/10.1016/j.neuroimage.2008.10.057>
- Catani, M., & de Schotten, M. T. (2012). *Atlas of Human Brain Connections*. OUP Oxford.

Retrieved from <https://market.android.com/details?id=book-nROILZ9HwEgC>

Cavada, C., Company, T., Tejedor, J., Cruz-Rizzolo, R. J., & Reinoso-Suarez, F. (2000). The

Anatomical Connections of the Macaque Monkey Orbitofrontal Cortex. A Review.

*Cerebral Cortex, 10*, 220–242. [https://doi.org/https://doi.org/10.1093/cercor/10.3.220](https://doi.org/10.1093/cercor/10.3.220)

Cavada, C., & Goldman-Rakic, P. S. (1989). Posterior parietal cortex in rhesus monkey: II.

Evidence for segregated corticocortical networks linking sensory and limbic areas with the frontal lobe. *The Journal of Comparative Neurology, 287*(4), 422–445.

<https://doi.org/10.1002/cne.902870403>

Chafee, M. V., & Goldman-Rakic, P. S. (2000). Inactivation of parietal and prefrontal cortex

reveals interdependence of neural activity during memory-guided saccades. *Journal of*

*Neurophysiology, 83*(3), 1550–1566. Retrieved from

<https://www.ncbi.nlm.nih.gov/pubmed/10712479>

Choi, E. Y., Yeo, B. T. T., & Buckner, R. L. (2012). The organization of the human striatum

estimated by intrinsic functional connectivity. *Journal of Neurophysiology, 108*(8),

2242–2263. <https://doi.org/10.1152/jn.00270.2012>

Cisek, P., & Kalaska, J. F. (2005). Neural correlates of reaching decisions in dorsal premotor

cortex: specification of multiple direction choices and final selection of action. *Neuron, 45*(5), 801–814. <https://doi.org/10.1016/j.neuron.2005.01.027>

Cisek, P., & Kalaska, J. F. (2010). Neural mechanisms for interacting with a world full of action

choices. *Annual Review of Neuroscience, 33*, 269–298.

<https://doi.org/10.1146/annurev.neuro.051508.135409>

Clarke, A., & Tyler, L. K. (2014). Object-specific semantic coding in human perirhinal cortex.

- The Journal of Neuroscience: The Official Journal of the Society for Neuroscience*, 34(14), 4766–4775. <https://doi.org/10.1523/JNEUROSCI.2828-13.2014>
- Colby, C. L. (1998). Action-oriented spatial reference frames in cortex. *Neuron*, 20(1), 15–24. [https://doi.org/10.1016/S0896-6273\(00\)80429-8](https://doi.org/10.1016/S0896-6273(00)80429-8)
- Colby, C. L., & Duhamel, J. R. (1996). Spatial representations for action in parietal cortex. *Brain Research. Cognitive Brain Research*, 5(1-2), 105–115. [https://doi.org/10.1016/S0926-6410\(96\)00046-8](https://doi.org/10.1016/S0926-6410(96)00046-8)
- Colby, C. L., & Goldberg, M. E. (1999). Space and attention in parietal cortex. *Annual Review of Neuroscience*, 22, 319–349. <https://doi.org/10.1146/annurev.neuro.22.1.319>
- Cosmides, L., & Tooby, J. (1992). Cognitive adaptations for social exchange. In J. H. Barkow, L. Cosmides, & J. Tooby (Eds.), *The Adapted Mind: Evolutionary Psychology and the Generation of Culture* (pp. 163–228). New York: Oxford University Press.
- Crammond, D. J., & Kalaska, J. F. (1994). Modulation of preparatory neuronal activity in dorsal premotor cortex due to stimulus-response compatibility. *Journal of Neurophysiology*, 71(3), 1281–1284. Retrieved from <https://www.ncbi.nlm.nih.gov/pubmed/8201421>
- Curtis, C. E. (2006). Prefrontal and parietal contributions to spatial working memory. *Neuroscience*, 139(1), 173–180. <https://doi.org/10.1016/j.neuroscience.2005.04.070>
- Cushman, F., Knobe, J., & Sinnott-Armstrong, W. (2008). Moral appraisals affect doing/allowing judgments. *Cognition*, 108(1), 281–289. <https://doi.org/10.1016/j.cognition.2008.02.005>
- Dekleva, B. M., Ramkumar, P., Wanda, P. A., Kording, K. P., & Miller, L. E. (2016). Uncertainty leads to persistent effects on reach representations in dorsal premotor cortex.

*eLife*, 5. <https://doi.org/10.7554/eLife.14316>

Diedrichsen, J., Wiestler, T., & Krakauer, J. W. (2013). Two distinct ipsilateral cortical representations for individuated finger movements. *Cerebral Cortex*, 23(6), 1362–1377.

<https://doi.org/10.1093/cercor/bhs120>

Dixon, M. L., & Christoff, K. (2014). The lateral prefrontal cortex and complex value-based learning and decision making. *Neuroscience and Biobehavioral Reviews*, 45, 9–18.

<https://doi.org/10.1016/j.neubiorev.2014.04.011>

Domenech, P., & Koechlin, E. (2015/2). Executive control and decision-making in the prefrontal cortex. *Current Opinion in Behavioral Sciences*, 1, 101–106.

<https://doi.org/10.1016/j.cobeha.2014.10.007>

Doya, K. (2008). Modulators of decision making. *Nature Neuroscience*, 11(4), 410–416.

<https://doi.org/10.1038/nn2077>

Faisal, A. A., Selen, L. P. J., & Wolpert, D. M. (2008). Noise in the nervous system. *Nature Reviews Neuroscience*, 9(4), 292–303. <https://doi.org/10.1038/nrn2258>

Feltz, A. (2007). The Knobe Effect: A Brief Overview. *The Journal of Mind and Behavior*, 28(3/4), 265–277. Retrieved from <http://www.jstor.org/stable/43854197>

Fernandes, H. L., Stevenson, I. H., Vilares, I., & Kording, K. P. (2014). The generalization of prior uncertainty during reaching. *The Journal of Neuroscience: The Official Journal of the Society for Neuroscience*, 34(34), 11470–11484.

<https://doi.org/10.1523/JNEUROSCI.3882-13.2014>

Fernandez-Miranda, J. C., Pathak, S., Engh, J., Jarbo, K., Verstynen, T., Yeh, F.-C., ...

Friedlander, R. (2012). High-definition fiber tractography of the human brain:

- neuroanatomical validation and neurosurgical applications. *Neurosurgery*, 71(2), 430–453.  
<https://doi.org/10.1227/NEU.0b013e3182592faa>
- Fitts, P. M. (1954). The information capacity of the human motor system in controlling the amplitude of movement. *Journal of Experimental Psychology*, 47(6), 381–391. Retrieved from <https://www.ncbi.nlm.nih.gov/pubmed/13174710>
- Franklin, D. W., & Wolpert, D. M. (2011). Computational mechanisms of sensorimotor control. *Neuron*, 72(3), 425–442. <https://doi.org/10.1016/j.neuron.2011.10.006>
- Funahashi, S., Bruce, C. J., & Goldman-Rakic, P. S. (1989). Mnemonic coding of visual space in the monkey's dorsolateral prefrontal cortex. *Journal of Neurophysiology*, 61(2), 331–349. Retrieved from <https://www.ncbi.nlm.nih.gov/pubmed/2918358>
- Gepshtain, S., Seydell, A., & Trommershäuser, J. (2007). Optimality of human movement under natural variations of visual-motor uncertainty. *Journal of Vision*, 7(5), 13.1–18.  
<https://doi.org/10.1167/7.5.13>
- Goodale, M. A., & Milner, A. D. (1992). Separate visual pathways for perception and action. *Trends in Neurosciences*, 15(1), 20–25. [https://doi.org/10.1016/0166-2236\(92\)90344-8](https://doi.org/10.1016/0166-2236(92)90344-8)
- Gottfried, J. A., O'Doherty, J., & Dolan, R. J. (2003). Encoding predictive reward value in human amygdala and orbitofrontal cortex. *Science*, 301(5636), 1104–1107.  
<https://doi.org/10.1126/science.1087919>
- Gottlieb, J. (2002). Parietal mechanisms of target representation. *Current Opinion in Neurobiology*, 12(2), 134–140. Retrieved from <https://www.ncbi.nlm.nih.gov/pubmed/12015228>
- Gottlieb, J. (2007). From thought to action: the parietal cortex as a bridge between perception,

- action, and cognition. *Neuron*, 53(1), 9–16. <https://doi.org/10.1016/j.neuron.2006.12.009>
- Gottlieb, J., Hayhoe, M., Hikosaka, O., & Rangel, A. (2014). Attention, reward, and information seeking. *The Journal of Neuroscience: The Official Journal of the Society for Neuroscience*, 34(46), 15497–15504. <https://doi.org/10.1523/JNEUROSCI.3270-14.2014>
- Grau-Moya, J., Ortega, P. A., & Braun, D. A. (2012). Risk-sensitivity in Bayesian sensorimotor integration. *PLoS Computational Biology*, 8(9), e1002698.  
<https://doi.org/10.1371/journal.pcbi.1002698>
- Grau-Moya, J., Ortega, P. A., & Braun, D. A. (2016). Decision-Making under Ambiguity Is Modulated by Visual Framing, but Not by Motor vs. Non-Motor Context. Experiments and an Information-Theoretic Ambiguity Model. *PloS One*, 11(4), e0153179.  
<https://doi.org/10.1371/journal.pone.0153179>
- Graybiel, A. M. (2008). Habits, rituals, and the evaluative brain. *Annual Review of Neuroscience*, 31, 359–387. <https://doi.org/10.1146/annurev.neuro.29.051605.112851>
- Greene, J. D., Sommerville, R. B., Nystrom, L. E., Darley, J. M., & Cohen, J. D. (2001). An fMRI investigation of emotional engagement in moral judgment. *Science*, 293(5537), 2105–2108. <https://doi.org/10.1126/science.1062872>
- Griggs, R. A., & Cox, J. R. (1982). The elusive thematic-materials effect in Wason's selection task. *British Journal of Psychology*, 73(3), 407–420.  
<https://doi.org/10.1111/j.2044-8295.1982.tb01823.x>
- Grubbs, F. E. (1969). Procedures for Detecting Outlying Observations in Samples. *Technometrics: A Journal of Statistics for the Physical, Chemical, and Engineering Sciences*, 11(1), 1–21. <https://doi.org/10.1080/00401706.1969.10490657>

Haber, S. N. (2003). The primate basal ganglia: parallel and integrative networks. *Journal of Chemical Neuroanatomy*, 26(4), 317–330. Retrieved from  
<http://www.ncbi.nlm.nih.gov/pubmed/14729134>

Haber, S. N. (2016). Corticostriatal circuitry. *Dialogues in Clinical Neuroscience*, 18(1), 7–21.  
Retrieved from <https://www.ncbi.nlm.nih.gov/pubmed/27069376>

Haber, S. N., & Calzavara, R. (2009). The cortico-basal ganglia integrative network: the role of the thalamus. *Brain Research Bulletin*, 78(2-3), 69–74.  
<https://doi.org/10.1016/j.brainresbull.2008.09.013>

Haber, S. N., & Knutson, B. (2010). The reward circuit: linking primate anatomy and human imaging. *Neuropsychopharmacology: Official Publication of the American College of Neuropsychopharmacology*, 35(1), 4–26. <https://doi.org/10.1038/npp.2009.129>

Harris, C. M., & Wolpert, D. M. (1998). Signal-dependent noise determines motor planning. *Nature*, 394(6695), 780–784. <https://doi.org/10.1038/29528>

Hershey, J. C., & Paul J. H. Schoemaker. (1980). Risk Taking and Problem Context in the Domain of Losses: An Expected Utility Analysis. *The Journal of Risk and Insurance*, 47(1), 111–132. <https://doi.org/10.2307/252685>

Hikosaka, O., Sakamoto, M., & Usui, S. (1989). Functional properties of monkey caudate neurons. III. Activities related to expectation of target and reward. *Journal of Neurophysiology*, 61(4), 814–832. Retrieved from  
<https://www.ncbi.nlm.nih.gov/pubmed/2723722>

Hoshi, E. (2006). Functional specialization within the dorsolateral prefrontal cortex: a review of anatomical and physiological studies of non-human primates. *Neuroscience Research*,

54(2), 73–84. <https://doi.org/10.1016/j.neures.2005.10.013>

Hoshi, E. (2013). Cortico-basal ganglia networks subserving goal-directed behavior mediated by conditional visuo-goal association. *Frontiers in Neural Circuits*, 7, 158.  
<https://doi.org/10.3389/fncir.2013.00158>

Hoshi, E., Shima, K., & Tanji, J. (1998). Task-dependent selectivity of movement-related neuronal activity in the primate prefrontal cortex. *Journal of Neurophysiology*, 80(6), 3392–3397. Retrieved from <https://www.ncbi.nlm.nih.gov/pubmed/9862940>

Hoshi, E., & Tanji, J. (2006). Differential involvement of neurons in the dorsal and ventral premotor cortex during processing of visual signals for action planning. *Journal of Neurophysiology*, 95(6), 3596–3616. <https://doi.org/10.1152/jn.01126.2005>

Houk, J. C., & Adams, J. L. (1995). 13 A Model of How the Basal Ganglia Generate and Use Neural Signals That. *Models of Information Processing in the Basal Ganglia*, 249.

Retrieved from

[https://books.google.com/books?hl=en&lr=&id=q6RThpQR\\_aIC&oi=fnd&pg=PA249&dq=houk+adams+barto&ots=zQ-y0bIi7h&sig=ZY2OgOoj8tCyYBLWTpm0IUau0v4](https://books.google.com/books?hl=en&lr=&id=q6RThpQR_aIC&oi=fnd&pg=PA249&dq=houk+adams+barto&ots=zQ-y0bIi7h&sig=ZY2OgOoj8tCyYBLWTpm0IUau0v4)

Howard, J. D., Gottfried, J. A., Tobler, P. N., & Kahnt, T. (2015). Identity-specific coding of future rewards in the human orbitofrontal cortex. *Proceedings of the National Academy of Sciences of the United States of America*, 112(16), 5195–5200.  
<https://doi.org/10.1073/pnas.1503550112>

Hsu, M., Bhatt, M., Adolphs, R., Tranel, D., & Camerer, C. F. (2005). Neural systems responding to degrees of uncertainty in human decision-making. *Science*, 310(5754), 1680–1683. <https://doi.org/10.1126/science.1115327>

- Hudson, T. E., Wolfe, U., & Maloney, L. T. (2012). Speeded reaching movements around invisible obstacles. *PLoS Computational Biology*, 8(9), e1002676.  
<https://doi.org/10.1371/journal.pcbi.1002676>
- Jarbo, K., Flemming, R., & Verstynen, T. D. (2017). Sensory uncertainty impacts avoidance during spatial decisions. *Experimental Brain Research. Experimentelle Hirnforschung. Experimentation Cerebrale*, 1–9. <https://doi.org/10.1007/s00221-017-5145-7>
- Jarbo, K., & Verstynen, T. D. (2015). Converging structural and functional connectivity of orbitofrontal, dorsolateral prefrontal, and posterior parietal cortex in the human striatum. *The Journal of Neuroscience: The Official Journal of the Society for Neuroscience*, 35(9), 3865–3878. <https://doi.org/10.1523/JNEUROSCI.2636-14.2015>
- Jarvstad, A., Hahn, U., Rushton, S. K., & Warren, P. A. (2013). Perceptuo-motor, cognitive, and description-based decision-making seem equally good. *Proceedings of the National Academy of Sciences of the United States of America*, 110(40), 16271–16276.  
<https://doi.org/10.1073/pnas.1300239110>
- Jarvstad, A., Hahn, U., Warren, P. A., & Rushton, S. K. (2014). Are perceptuo-motor decisions really more optimal than cognitive decisions? *Cognition*, 130(3), 397–416.  
<https://doi.org/10.1016/j.cognition.2013.09.009>
- Juni, M. Z., Gureckis, T. M., & Maloney, L. T. (2016). Information sampling behavior with explicit sampling costs. *Decisions*, 3(3), 147–168. <https://doi.org/10.1037/dec0000045>
- Kagan, S. (1988). Causation and Responsibility. *American Philosophical Quarterly*, 25(4), 293–302. Retrieved from <http://www.jstor.org/stable/20014252>
- Kahane, G., Everett, J. A. C., Earp, B. D., Caviola, L., Faber, N. S., Crockett, M. J., &

- Savulescu, J. (2017). Beyond Sacrificial Harm: A Two-Dimensional Model of Utilitarian Psychology. *Psychological Review*. <https://doi.org/10.1037/rev0000093>
- Kahneman, D., & Tversky, A. (1979). Prospect Theory: An Analysis of Decision under Risk. *Econometrica: Journal of the Econometric Society*, 47(2), 263–291.  
<https://doi.org/10.2307/1914185>
- Kahneman, D., & Tversky, A. (1984). Choices, values, and frames. *The American Psychologist*, 39(4), 341–350. <https://doi.org/10.1037/0003-066X.39.4.341>
- Kahnt, T. (2017). A decade of decoding reward-related fMRI signals and where we go from here. *NeuroImage*. <https://doi.org/10.1016/j.neuroimage.2017.03.067>
- Kakei, S., Hoffman, D. S., & Strick, P. L. (2001). Direction of action is represented in the ventral premotor cortex. *Nature Neuroscience*, 4(10), 1020–1025. <https://doi.org/10.1038/nn726>
- Kemp, J. M., & Powell, T. P. (1970). The cortico-striate projection in the monkey. *Brain: A Journal of Neurology*, 93(3), 525–546. Retrieved from  
<https://www.ncbi.nlm.nih.gov/pubmed/4990231>
- Kermadi, I., & Joseph, J. P. (1995). Activity in the caudate nucleus of monkey during spatial sequencing. *Journal of Neurophysiology*, 74(3), 911–933. Retrieved from  
<https://www.ncbi.nlm.nih.gov/pubmed/7500161>
- Kim, S. G., Ashe, J., Hendrich, K., Ellermann, J. M., Merkle, H., Uğurbil, K., & Georgopoulos, A. P. (1993). Functional magnetic resonance imaging of motor cortex: hemispheric asymmetry and handedness. *Science*, 261(5121), 615–617. Retrieved from  
<https://www.ncbi.nlm.nih.gov/pubmed/8342027>
- Kleiner, M., Brainard, D., Pelli, D., Ingling, A., Murray, R., Broussard, C., & Others. (2007).

- What's new in Psychtoolbox-3. *Perception*, 36(14), 1. Retrieved from  
[http://www.kyb.mpg.de/publications/attachments/ECVP2007-Kleiner-slides\\_5490\[0\].pdf](http://www.kyb.mpg.de/publications/attachments/ECVP2007-Kleiner-slides_5490[0].pdf)
- Knill, D. C., & Pouget, A. (2004). The Bayesian brain: the role of uncertainty in neural coding and computation. *Trends in Neurosciences*, 27(12), 712–719.  
<https://doi.org/10.1016/j.tins.2004.10.007>
- Knobe, J. (2003a). Intentional Action and Side Effects in Ordinary Language. *Analysis*, 63(3), 190–194.
- Knobe, J. (2003b). Intentional action in folk psychology: An experimental investigation. *Philosophical Psychology*, 16(2), 309–324. <https://doi.org/10.1080/09515080307771>
- Kording, K. P., & Wolpert, D. M. (2004). Bayesian integration in sensorimotor learning. *Nature*, 427(6971), 244–247. <https://doi.org/10.1038/nature02169>
- Kording, K. P., & Wolpert, D. M. (2006). Bayesian decision theory in sensorimotor control. *Trends in Cognitive Sciences*, 10(7), 319–326. <https://doi.org/10.1016/j.tics.2006.05.003>
- Kriegeskorte, N., Goebel, R., & Bandettini, P. (2006). Information-based functional brain mapping. *Proceedings of the National Academy of Sciences of the United States of America*, 103(10), 3863–3868. <https://doi.org/10.1073/pnas.0600244103>
- Kriegeskorte, N., Mur, M., & Bandettini, P. (2008). Representational similarity analysis - connecting the branches of systems neuroscience. *Frontiers in Systems Neuroscience*, 2, 4.  
<https://doi.org/10.3389/neuro.06.004.2008>
- Kringelbach, M. L., & Rolls, E. T. (2004). The functional neuroanatomy of the human orbitofrontal cortex: evidence from neuroimaging and neuropsychology. *Progress in Neurobiology*, 72(5), 341–372. <https://doi.org/10.1016/j.pneurobio.2004.03.006>

Kubota, K., & Funahashi, S. (1982). Direction-specific activities of dorsolateral prefrontal and motor cortex pyramidal tract neurons during visual tracking. *Journal of Neurophysiology*, 47(3), 362–376. Retrieved from <https://www.ncbi.nlm.nih.gov/pubmed/7069449>

Kurniawan, I. T., Seymour, B., Talmi, D., Yoshida, W., Chater, N., & Dolan, R. J. (2010).

Choosing to make an effort: the role of striatum in signaling physical effort of a chosen action. *Journal of Neurophysiology*, 104(1), 313–321.

<https://doi.org/10.1152/jn.00027.2010>

Kwon, O.-S., & Knill, D. C. (2013). The brain uses adaptive internal models of scene statistics for sensorimotor estimation and planning. *Proceedings of the National Academy of Sciences of the United States of America*, 110(11), E1064–E1073.

<https://doi.org/10.1073/pnas.1214869110>

Lau, B., & Glimcher, P. W. (2007). Action and outcome encoding in the primate caudate nucleus. *The Journal of Neuroscience: The Official Journal of the Society for Neuroscience*, 27(52), 14502–14514. <https://doi.org/10.1523/JNEUROSCI.3060-07.2007>

Lee, D., Seo, H., & Jung, M. W. (2012). Neural basis of reinforcement learning and decision making. *Annual Review of Neuroscience*, 35, 287–308.

<https://doi.org/10.1146/annurev-neuro-062111-150512>

Lu, M. T., Preston, J. B., & Strick, P. L. (1994). Interconnections between the prefrontal cortex and the premotor areas in the frontal lobe. *The Journal of Comparative Neurology*, 341(3), 375–392. <https://doi.org/10.1002/cne.903410308>

Maloney, L. T., & Zhang, H. (2010). Decision-theoretic models of visual perception and action. *Vision Research*, 50(23), 2362–2374. <https://doi.org/10.1016/j.visres.2010.09.031>

- Martino, J., De Witt Hamer, P. C., Berger, M. S., Lawton, M. T., Arnold, C. M., de Lucas, E. M., & Duffau, H. (2013). Analysis of the subcomponents and cortical terminations of the perisylvian superior longitudinal fasciculus: a fiber dissection and DTI tractography study. *Brain Structure & Function*, 218(1), 105–121. <https://doi.org/10.1007/s00429-012-0386-5>
- McDougle, S. D., Bond, K. M., & Taylor, J. A. (2015). Explicit and Implicit Processes Constitute the Fast and Slow Processes of Sensorimotor Learning. *The Journal of Neuroscience: The Official Journal of the Society for Neuroscience*, 35(26), 9568–9579. <https://doi.org/10.1523/JNEUROSCI.5061-14.2015>
- McGinty, V. B., Rangel, A., & Newsome, W. T. (2016). Orbitofrontal Cortex Value Signals Depend on Fixation Location during Free Viewing. *Neuron*, 90(6), 1299–1311. <https://doi.org/10.1016/j.neuron.2016.04.045>
- Meyer, D. E., Abrams, R. A., Kornblum, S., Wright, C. E., & Smith, J. E. (1988). Optimality in human motor performance: ideal control of rapid aimed movements. *Psychological Review*, 95(3), 340–370. Retrieved from <https://www.ncbi.nlm.nih.gov/pubmed/3406245>
- Miller, E. K., & Cohen, J. D. (2001). An integrative theory of prefrontal cortex function. *Annual Review of Neuroscience*, 24, 167–202. <https://doi.org/10.1146/annurev.neuro.24.1.167>
- Mill, J. S. (1863). *Utilitarianism*. Parker, Son and Bourn. Retrieved from <https://market.android.com/details?id=book-HCY2AQAAAMAJ>
- Mishkin, M., Ungerleider, L. G., & Macko, K. A. (1983). Object vision and spatial vision: two cortical pathways. *Trends in Neuroscience*, 6, 414–417. Retrieved from [http://ling.umd.edu/~ellenlau/courses/nacs642/Mishkin\\_1983.pdf](http://ling.umd.edu/~ellenlau/courses/nacs642/Mishkin_1983.pdf)
- Monchi, O., Petrides, M., Petre, V., Worsley, K., & Dagher, A. (2001). Wisconsin Card Sorting

- revisited: distinct neural circuits participating in different stages of the task identified by event-related functional magnetic resonance imaging. *The Journal of Neuroscience: The Official Journal of the Society for Neuroscience*, 21(19), 7733–7741. Retrieved from <https://www.ncbi.nlm.nih.gov/pubmed/11567063>
- Monchi, O., Petrides, M., Strafella, A. P., Worsley, K. J., & Doyon, J. (2006). Functional role of the basal ganglia in the planning and execution of actions. *Annals of Neurology*, 59(2), 257–264. <https://doi.org/10.1002/ana.20742>
- Moore, G. E. (1903). *Principia Ethica*. Dover Publications. Retrieved from <https://philpapers.org/rec/mooke>
- Murray, E. A., & Rudebeck, P. H. (2018). Specializations for reward-guided decision-making in the primate ventral prefrontal cortex. *Nature Reviews. Neuroscience*, 19(7), 404–417. <https://doi.org/10.1038/s41583-018-0013-4>
- Mutha, P. K., Haaland, K. Y., & Sainburg, R. L. (2012). The effects of brain lateralization on motor control and adaptation. *Journal of Motor Behavior*, 44(6), 455–469. <https://doi.org/10.1080/00222895.2012.747482>
- Mutha, P. K., Haaland, K. Y., & Sainburg, R. L. (2013). Rethinking motor lateralization: specialized but complementary mechanisms for motor control of each arm. *PLoS One*, 8(3), e58582. <https://doi.org/10.1371/journal.pone.0058582>
- Nagengast, A. J., Braun, D. A., & Wolpert, D. M. (2010). Risk-sensitive optimal feedback control accounts for sensorimotor behavior under uncertainty. *PLoS Computational Biology*, 6(7), e1000857. <https://doi.org/10.1371/journal.pcbi.1000857>
- Nakamura, K. (2018). Harming is more intentional than helping because it is more probable: the

- underlying influence of probability on the Knobe effect. *Journal of Cognitive Psychology*, 30(2), 129–137. <https://doi.org/10.1080/20445911.2017.1415345>
- Neyedli, H. F., & Welsh, T. N. (2013). Optimal weighting of costs and probabilities in a risky motor decision-making task requires experience. *Journal of Experimental Psychology. Human Perception and Performance*, 39(3), 638–645. <https://doi.org/10.1037/a0030518>
- Neyedli, H. F., & Welsh, T. N. (2014). People are better at maximizing expected gain in a manual aiming task with rapidly changing probabilities than with rapidly changing payoffs. *Journal of Neurophysiology*, 111(5), 1016–1026. <https://doi.org/10.1152/jn.00163.2013>
- Neyedli, H. F., & Welsh, T. N. (2015). The preference of probability over negative values in action selection. *Quarterly Journal of Experimental Psychology*, 68(2), 261–283. <https://doi.org/10.1080/17470218.2014.942674>
- Nili, H., Wingfield, C., Walther, A., Su, L., Marslen-Wilson, W., & Kriegeskorte, N. (2014). A toolbox for representational similarity analysis. *PLoS Computational Biology*, 10(4), e1003553. <https://doi.org/10.1371/journal.pcbi.1003553>
- Noonan, M. P., Kolling, N., Walton, M. E., & Rushworth, M. F. S. (2012). Re-evaluating the role of the orbitofrontal cortex in reward and reinforcement. *The European Journal of Neuroscience*, 35(7), 997–1010. <https://doi.org/10.1111/j.1460-9568.2012.08023.x>
- O'Brien, M. K., & Ahmed, A. A. (2016). Rationality in Human Movement. *Exercise and Sport Sciences Reviews*, 44(1), 20–28. <https://doi.org/10.1249/JES.0000000000000066>
- O'Neill, M., & Schultz, W. (2013). Risk Prediction Error Coding in Orbitofrontal Neurons. *The Journal of Neuroscience: The Official Journal of the Society for Neuroscience*, 33(40), 15810–15814. <https://doi.org/10.1523/JNEUROSCI.4236-12.2013>

- Orbán, G., & Wolpert, D. M. (2011). Representations of uncertainty in sensorimotor control. *Current Opinion in Neurobiology*, 21(4), 629–635.  
<https://doi.org/10.1016/j.conb.2011.05.026>
- Osborne, L. C., Lisberger, S. G., & Bialek, W. (2005). A sensory source for motor variation. *Nature*, 437(7057), 412–416. <https://doi.org/10.1038/nature03961>
- Padoa-Schioppa, C., & Assad, J. A. (2006). Neurons in the orbitofrontal cortex encode economic value. *Nature*, 441(7090), 223–226. <https://doi.org/10.1038/nature04676>
- Padoa-Schioppa, C., & Conen, K. E. (2017). Orbitofrontal Cortex: A Neural Circuit for Economic Decisions. *Neuron*, 96(4), 736–754. <https://doi.org/10.1016/j.neuron.2017.09.031>
- Parent, A., & Hazrati, L. N. (1995). Functional anatomy of the basal ganglia. I. The cortico-basal ganglia-thalamo-cortical loop. *Brain Research. Brain Research Reviews*, 20(1), 91–127.
- Retrieved from <https://www.ncbi.nlm.nih.gov/pubmed/7711769>
- Pauli, W. M., O'Reilly, R. C., Yarkoni, T., & Wager, T. D. (2016). Regional specialization within the human striatum for diverse psychological functions. *Proceedings of the National Academy of Sciences of the United States of America*, 113(7), 1907–1912.  
<https://doi.org/10.1073/pnas.1507610113>
- Pichert, J. W., & Anderson, R. C. (1977). Taking different perspectives on a story. *Journal of Educational Psychology*, 69(4), 309. <https://doi.org/10.1037/0022-0663.69.4.309>
- Ptak, R. (2012). The frontoparietal attention network of the human brain: action, saliency, and a priority map of the environment. *The Neuroscientist: A Review Journal Bringing Neurobiology, Neurology and Psychiatry*, 18(5), 502–515.  
<https://doi.org/10.1177/1073858411409051>

Quintana, J., Yajeya, J., & Fuster, J. M. (1988). Prefrontal representation of stimulus attributes during delay tasks. I. Unit activity in cross-temporal integration of sensory and

sensory-motor information. *Brain Research*, 474(2), 211–221. Retrieved from

<https://www.ncbi.nlm.nih.gov/pubmed/3208130>

Raghuraman, A. P., & Padoa-Schioppa, C. (2014). Integration of multiple determinants in the neuronal computation of economic values. *The Journal of Neuroscience: The Official Journal of the Society for Neuroscience*, 34(35), 11583–11603.

<https://doi.org/10.1523/JNEUROSCI.1235-14.2014>

Rainer, G., Asaad, W. F., & Miller, E. K. (1998). Selective representation of relevant information by neurons in the primate prefrontal cortex. *Nature*, 393(6685), 577–579.

<https://doi.org/10.1038/31235>

Retailleau, A., Etienne, S., Guthrie, M., & Boraud, T. (2012). Where is my reward and how do I get it? Interaction between the hippocampus and the basal ganglia during spatial learning.

*Journal of Physiology, Paris*, 106(3-4), 72–80.

<https://doi.org/10.1016/j.jphysparis.2011.10.002>

Ridderinkhof, K. R., van den Wildenberg, W. P. M., Segalowitz, S. J., & Carter, C. S. (2004).

Neurocognitive mechanisms of cognitive control: The role of prefrontal cortex in action selection, response inhibition, performance monitoring, and reward-based learning. *Brain and Cognition*, 56(2), 129–140. <https://doi.org/10.1016/j.bandc.2004.09.016>

Rizzolatti, G., Gentilucci, M., Fogassi, L., Luppino, G., Matelli, M., & Ponzoni-Maggi, S.

(1987). Neurons related to goal-directed motor acts in inferior area 6 of the macaque monkey. *Experimental Brain Research. Experimentelle Hirnforschung. Experimentation*

- Cerebrale*, 67(1), 220–224. Retrieved from <https://www.ncbi.nlm.nih.gov/pubmed/3622679>
- Romo, R., Hernández, A., & Zainos, A. (2004). Neuronal correlates of a perceptual decision in ventral premotor cortex. *Neuron*, 41(1), 165–173.  
[https://doi.org/10.1016/S0896-6273\(03\)00817-1](https://doi.org/10.1016/S0896-6273(03)00817-1)
- Rudebeck, P. H., & Murray, E. A. (2011). Balkanizing the primate orbitofrontal cortex: distinct subregions for comparing and contrasting values. *Annals of the New York Academy of Sciences*, 1239, 1–13. <https://doi.org/10.1111/j.1749-6632.2011.06267.x>
- Schmahmann, J., & Pandya, D. (2006). *Fiber Pathways of the Brain*. Oxford University Press, Inc.
- Schultz, W. (2016). Reward functions of the basal ganglia. *Journal of Neural Transmission*, 123(7), 679–693. <https://doi.org/10.1007/s00702-016-1510-0>
- Schultz, W., & Romo, R. (1992). Role of primate basal ganglia and frontal cortex in the internal generation of movements. *Experimental Brain Research. Experimentelle Hirnforschung. Experimentation Cerebrale*, 91(3), 363–384. <https://doi.org/10.1007/BF00227834>
- Schultz, W., & Romo, R. (1992). Role of primate basal ganglia and frontal cortex in the internal generation of movements. I. Preparatory activity in the anterior striatum. *Experimental Brain Research. Experimentelle Hirnforschung. Experimentation Cerebrale*, 91(3), 363–384. Retrieved from <https://www.ncbi.nlm.nih.gov/pubmed/1483512>
- Schultz, W., Tremblay, L., & Hollerman, J. R. (2000). Reward processing in primate orbitofrontal cortex and basal ganglia. *Cerebral Cortex*, 10(3), 272–284. Retrieved from <https://www.ncbi.nlm.nih.gov/pubmed/10731222>
- Selemon, L. D., & Goldman-Rakic, P. S. (1985). Longitudinal topography and interdigitation of

- corticostriatal projections in the rhesus monkey. *The Journal of Neuroscience: The Official Journal of the Society for Neuroscience*, 5(3), 776–794. Retrieved from <http://www.ncbi.nlm.nih.gov/pubmed/2983048>
- Selemon, L. D., & Goldman-Rakic, P. S. (1988). Common cortical and subcortical targets of the dorsolateral prefrontal and posterior parietal cortices in the rhesus monkey: evidence for a distributed neural network subserving spatially guided behavior. *The Journal of Neuroscience: The Official Journal of the Society for Neuroscience*, 8(11), 4049–4068. Retrieved from <https://www.ncbi.nlm.nih.gov/pubmed/2846794>
- Sinnott-Armstrong, W. (2008). Framing Moral Intuitions. In W. Sinnott-Armstrong (Ed.), *Moral Psychology: The Cognitive Science of Morality: Intuition and Diversity* (Vol. 2, pp. 47–76). MIT Press.
- Sinnott-Armstrong, W., Mallon, R., McCOY, T., & Hull, J. G. (2008). Intention, Temporal Order, and Moral Judgments. *Mind & Language*, 23(1), 90–106.  
<https://doi.org/10.1111/j.1468-0017.2007.00330.x>
- Strait, C. E., Sleezer, B. J., Blanchard, T. C., Azab, H., Castagno, M. D., & Hayden, B. Y. (2016). Neuronal selectivity for spatial positions of offers and choices in five reward regions. *Journal of Neurophysiology*, 115(3), 1098–1111.  
<https://doi.org/10.1152/jn.00325.2015>
- Sutton, R. S., & Barto, A. G. (1998). *Reinforcement Learning: An Introduction*. Cambridge, MA: MIT Press.
- Tassinari, H., Hudson, T. E., & Landy, M. S. (2006). Combining priors and noisy visual cues in a rapid pointing task. *The Journal of Neuroscience: The Official Journal of the Society for*

- Neuroscience*, 26(40), 10154–10163. <https://doi.org/10.1523/JNEUROSCI.2779-06.2006>
- Taylor, J. A., & Ivry, R. B. (2011). Flexible cognitive strategies during motor learning. *PLoS Computational Biology*, 7(3), e1001096. <https://doi.org/10.1371/journal.pcbi.1001096>
- Taylor, J. A., & Ivry, R. B. (2012). The role of strategies in motor learning. *Annals of the New York Academy of Sciences*, 1251, 1–12. <https://doi.org/10.1111/j.1749-6632.2011.06430.x>
- Taylor, J. A., Krakauer, J. W., & Ivry, R. B. (2014). Explicit and implicit contributions to learning in a sensorimotor adaptation task. *The Journal of Neuroscience: The Official Journal of the Society for Neuroscience*, 34(8), 3023–3032.  
<https://doi.org/10.1523/JNEUROSCI.3619-13.2014>
- Thomson, J. J. (1986). *Rights, Restitution, and Risk: Essays in Moral Theory*. Harvard University Press. Retrieved from <https://market.android.com/details?id=book-sLh4oBgJEtEC>
- Todd, P. M., & Gigerenzer, G. (2000). Précis of Simple heuristics that make us smart. *The Behavioral and Brain Sciences*, 23(5), 727–741; discussion 742–780. Retrieved from <https://www.ncbi.nlm.nih.gov/pubmed/11301545>
- Todorov, E. (2004). Optimality principles in sensorimotor control. *Nature Neuroscience*, 7(9), 907–915. <https://doi.org/10.1038/nn1309>
- Todorov, E., & Jordan, M. I. (2002). Optimal feedback control as a theory of motor coordination. *Nature Neuroscience*, 5(11), 1226–1235. <https://doi.org/10.1038/nn963>
- Trommershäuser, J., Gepshtein, S., Maloney, L. T., Landy, M. S., & Banks, M. S. (2005). Optimal compensation for changes in task-relevant movement variability. *The Journal of Neuroscience: The Official Journal of the Society for Neuroscience*, 25(31), 7169–7178.  
<https://doi.org/10.1523/JNEUROSCI.1906-05.2005>

Trommershäuser, J., Landy, M. S., & Maloney, L. T. (2006). Humans rapidly estimate expected gain in movement planning. *Psychological Science*, 17(11), 981–988.

<https://doi.org/10.1111/j.1467-9280.2006.01816.x>

Trommershäuser, J., Maloney, L. T., & Landy, M. S. (2003a). Statistical decision theory and the selection of rapid, goal-directed movements. *Journal of the Optical Society of America. A, Optics, Image Science, and Vision*, 20(7), 1419–1433. Retrieved from

<https://www.ncbi.nlm.nih.gov/pubmed/12868646>

Trommershäuser, J., Maloney, L. T., & Landy, M. S. (2003b). Statistical decision theory and trade-offs in the control of motor response. *Spatial Vision*, 16(3-4), 255–275.

<https://doi.org/10.1163/156856803322467527>

Trommershäuser, J., Maloney, L. T., & Landy, M. S. (2008). Decision making, movement planning and statistical decision theory. *Trends in Cognitive Sciences*, 12(8), 291–297.

<https://doi.org/10.1016/j.tics.2008.04.010>

Tversky, A., & Fox, C. R. (1995). Weighing risk and uncertainty. *Psychological Review*, 102(2), 269. <https://doi.org/10.1037/0033-295X.102.2.269>

Tversky, A., & Kahneman, D. (1981). The Framing of Decisions and the Psychology of Choice. *Science*, 211(4881), 453–458.

Tversky, A., & Kahneman, D. (1992). Advances in prospect theory: Cumulative representation of uncertainty. *Journal of Risk and Uncertainty*, 5(4), 297–323.

<https://doi.org/10.1007/BF00122574>

Verstynen, T., & Sabes, P. N. (2011). How each movement changes the next: an experimental and theoretical study of fast adaptive priors in reaching. *The Journal of Neuroscience: The*

*Official Journal of the Society for Neuroscience*, 31(27), 10050–10059.

<https://doi.org/10.1523/JNEUROSCI.6525-10.2011>

Wakana, S., Jiang, H., Nagae-Poetscher, L. M., van Zijl, P. C. M., & Mori, S. (2004). Fiber Tract-based Atlas of Human White Matter Anatomy. *Radiology*, 230(1), 77–87.

<https://doi.org/10.1148/radiol.2301021640>

Wallis, J. D. (2007). Orbitofrontal cortex and its contribution to decision-making. *Annual Review of Neuroscience*, 30, 31–56. <https://doi.org/10.1146/annurev.neuro.30.051606.094334>

Walther, A., Nili, H., Ejaz, N., Alink, A., Kriegeskorte, N., & Diedrichsen, J. (2016). Reliability of dissimilarity measures for multi-voxel pattern analysis. *NeuroImage*, 137, 188–200.

<https://doi.org/10.1016/j.neuroimage.2015.12.012>

Walton, M. E., Behrens, T. E. J., Noonan, M. P., & Rushworth, M. F. S. (2011). Giving credit where credit is due: orbitofrontal cortex and valuation in an uncertain world. *Annals of the New York Academy of Sciences*, 1239, 14–24.

<https://doi.org/10.1111/j.1749-6632.2011.06257.x>

Wang, X. T. (1996). Framing Effects: Dynamics and Task Domains. *Organizational Behavior and Human Decision Processes*, 68(2), 145–157. Retrieved from <https://www.ncbi.nlm.nih.gov/pubmed/8954876>

Wason, P. C. (1968). Reasoning about a rule. *The Quarterly Journal of Experimental Psychology*, 20(3), 273–281. <https://doi.org/10.1080/14640746808400161>

Wason, P. C., & Shapiro, D. (1971). Natural and contrived experience in a reasoning problem. *The Quarterly Journal of Experimental Psychology*, 23(1), 63–71.

<https://doi.org/10.1080/00335557143000068>

- Wei, K., & Kording, K. (2010). Uncertainty of feedback and state estimation determines the speed of motor adaptation. *Frontiers in Computational Neuroscience*, 4, 11.  
<https://doi.org/10.3389/fncom.2010.00011>
- Weiskopf, N., Hutton, C., Josephs, O., & Deichmann, R. (2006). Optimal EPI parameters for reduction of susceptibility-induced BOLD sensitivity losses: a whole-brain analysis at 3 T and 1.5 T. *NeuroImage*, 33(2), 493–504. <https://doi.org/10.1016/j.neuroimage.2006.07.029>
- Windmann, S., Kirsch, P., Mier, D., Stark, R., Walter, B., Güntürkün, O., & Vaitl, D. (2006). On framing effects in decision making: linking lateral versus medial orbitofrontal cortex activation to choice outcome processing. *Journal of Cognitive Neuroscience*, 18(7), 1198–1211. <https://doi.org/10.1162/jocn.2006.18.7.1198>
- Wise, S. P., Boussaoud, D., Johnson, P. B., & Caminiti, R. (1997). PREMOTOR AND PARIETAL CORTEX: Corticocortical Connectivity and Combinatorial Computations. *Annual Review of Neuroscience*, 20(1), 25–42.  
<https://doi.org/10.1146/annurev.neuro.20.1.25>
- Wise, S. P., di Pellegrino, G., & Boussaoud, D. (1996). The premotor cortex and nonstandard sensorimotor mapping. *Canadian Journal of Physiology and Pharmacology*, 74(4), 469–482. Retrieved from <https://www.ncbi.nlm.nih.gov/pubmed/8828893>
- Wolpert, D. M. (2007). Probabilistic models in human sensorimotor control. *Human Movement Science*, 26(4), 511–524. <https://doi.org/10.1016/j.humov.2007.05.005>
- Wu, S.-W., Delgado, M. R., & Maloney, L. T. (2009). Economic decision-making compared with an equivalent motor task. *Proceedings of the National Academy of Sciences*, 106(15), 6088–6093.

- Wu, S.-W., Trommershäuser, J., Maloney, L. T., & Landy, M. S. (2006). Limits to human movement planning in tasks with asymmetric gain landscapes. *Journal of Vision*, 6(1), 53–63. <https://doi.org/10.1167/6.1.5>
- Yamagata, T., Nakayama, Y., Tanji, J., & Hoshi, E. (2009). Processing of visual signals for direct specification of motor targets and for conceptual representation of action targets in the dorsal and ventral premotor cortex. *Journal of Neurophysiology*, 102(6), 3280–3294. <https://doi.org/10.1152/jn.00452.2009>
- Yamagata, T., Nakayama, Y., Tanji, J., & Hoshi, E. (2012). Distinct information representation and processing for goal-directed behavior in the dorsolateral and ventrolateral prefrontal cortex and the dorsal premotor cortex. *The Journal of Neuroscience: The Official Journal of the Society for Neuroscience*, 32(37), 12934–12949. <https://doi.org/10.1523/JNEUROSCI.2398-12.2012>
- Yang, Y., Vosgerau, J., & Loewenstein, G. (2013). Framing Influences Willingness to Pay but Not Willingness to Accept. *JMR, Journal of Marketing Research*, 50(6), 725–738. <https://doi.org/10.1509/jmr.12.0430>
- Yeterian, E. H., Pandya, D. N., Tomaiuolo, F., & Petrides, M. (2012). The cortical connectivity of the prefrontal cortex in the monkey brain. *Cortex; a Journal Devoted to the Study of the Nervous System and Behavior*, 48(1), 58–81. <https://doi.org/10.1016/j.cortex.2011.03.004>
- Zhang, H., Daw, N. D., & Maloney, L. T. (2013). Testing whether humans have an accurate model of their own motor uncertainty in a speeded reaching task. *PLoS Computational Biology*, 9(5), e1003080. <https://doi.org/10.1371/journal.pcbi.1003080>
- Zhang, H., Daw, N. D., & Maloney, L. T. (2015). Human representation of visuo-motor

uncertainty as mixtures of orthogonal basis distributions. *Nature Neuroscience*, 18(8), 1152–1158. <https://doi.org/10.1038/nn.4055>